Production of π^0 mesons in ν_μ CC interactions in the tracker part of the near detector of the T2K experiment

Doctoral thesis by:
Marcela Batkiewicz

Advisor:
prof. Agnieszka Zalewska
Auxiliary advisor:
dr Tomasz Wąchała

H. Niewodniczański Institute of Nuclear Physics
Polish Academy of Sciences

Department of Neutrino and Dark Matter Studies

Cracow, Poland
April 2016

Produkcja mezonów π^0 w oddziaływaniach ν_μ CC w poddetektorze śladowym bliskiego detektora eksperymentu T2K

Praca doktorska

Autor:
Marcela Batkiewicz

Promotor:
prof. dr hab. Agnieszka Zalewska
Promotor pomocniczy:
dr Tomasz Wąchała

Instytut Fizyki Jądrowej im. Henryka Niewodniczańskiego
Polskiej Akademii Nauk

Zakład Neutrin i Ciemnej Materii

Kraków
Kwiecień 2016

Abstract

The analysis presented in this thesis concerns the inclusive ν_μ charged current interactions with at least one neutral pion leaving the target nucleus, $(\nu_\mu CC\pi^0)_{incl.}$. The total flux-averaged cross-section on the plastic scintillator target (CH) was measured using the tracker and calorimeter of the ND280 off-axis near detector of the T2K experiment. The cross-section determined based on 0.549×10^{21} POT (Protons On Target) real data sample

$$\langle\sigma\rangle^{data} = (1.239 \pm 0.034(stat)^{+0.235}_{-0.217}(syst)) \times 10^{-39}\text{cm}^2/\text{ nucleon}$$

agrees within the errors with the value predicted by the NEUT generator

$$\langle\sigma\rangle^{MC} = (1.0522 \pm 0.0028(stat)) \times 10^{-39}\text{cm}^2/\text{ nucleon}$$

based on 12.21×10^{21} POT MC sample.

Streszczenie

Analiza przedstawiona w tej pracy doktorskiej dotyczy oddziaływań neutrin mionowych przez wymianę prądów naładowanych z co najmniej jednym pionem neutralnym w stanie końcowym, $(\nu_\mu CC\pi^0)_{incl.}$. Całkowity, uśredniony po strumieniu przekrój czynny został zmierzony przy użyciu poddetektora śladowego i kalorymetru pozaosiowego, bliskiego detektora ND280 eksperymentu T2K. Przekrój czynny wyznaczony na podstawie próbki danych zawierającej 0.549×10^{21} POT (protonów na tarczę)

$$\langle\sigma\rangle^{data} = (1.239 \pm 0.034(stat)^{+0.235}_{-0.217}(syst)) \times 10^{-39}\text{cm}^2/\text{ nucleon}$$

zgadza się w granicach błędu z wartością przewidywaną w generatorze NEUT

$$\langle\sigma\rangle^{MC} = (1.0522 \pm 0.0028(stat)) \times 10^{-39}\text{cm}^2/\text{ nucleon}$$

dla próbki MC zawierającej 12.21×10^{21} POT.

Contents

Introduction

Neutrinos are very mysterious particles. After photons, they are the second most abundant particles in the Universe. Despite the fact that there are so many neutrinos, they are almost imperceptible. The average interaction length of a neutrino from a neutron decay is of the order of a galaxy size and for a 1 GeV neutrino it is a million of Earth's diameter. The concept of neutrino oscillations is well established and considered by many theorists as the first phenomenon from beyond the Standard Model. CP violation in the lepton sector, studied via neutrino oscillations, could provide an explanation for the observed matter dominance in the Universe. There are also interesting non-oscillation experiments searching for neutrinoless double beta decay, which would give evidence that neutrinos are the only elementary fermions identical with their own antiparticles. Such fermions are called Majorana particles.

Neutrino studies constitute an important and dynamic field of physics and astrophysics, which has already been awarded two Nobel Prizes in this century and the 2016 Breakthrough Prize in Fundamental Physics. However, it must be noted that further measurements are not possible without a good knowledge of neutrino interaction cross-sections, whose uncertainties are one of the most significant contributions to systematic errors. The goal of the analysis presented in this thesis is to improve our knowledge about the reaction denoted as $(\nu_\mu CC\pi^0)_{incl.}$.

The $(\nu_\mu CC\pi^0)_{incl.}$ reaction is defined as resulting from the muon neutrino interaction with a nucleon of the target nucleus, mediated by the charge current and characterized by a negative muon, at least one neutral pion and any other particles in the reaction's final state (Fig. 1). The use of the definition of the reaction based on particles leaving the nucleus, i.e. in the final state, makes the results more model-independent and easier to interpret for theorists.

The presented analysis includes the measurement of the total flux-averaged $(\nu_\mu CC\pi^0)_{incl.}$ cross-section in the near ND280 detector of the T2K experiment. Cross-section measurements for multi-pion (or more general multi-meson) neutrino interactions are almost non-existent in the literature [1, 2]. This analysis is the first inclusive measurement for this reaction. Two different production mechanisms contribute to the $(\nu_\mu CC\pi^0)_{incl.}$ reaction: single pion resonance production and Deep Inelastic Scattering (DIS). Secondary interactions inside the target nucleus, the Final State Interactions (FSI), additionally modify the

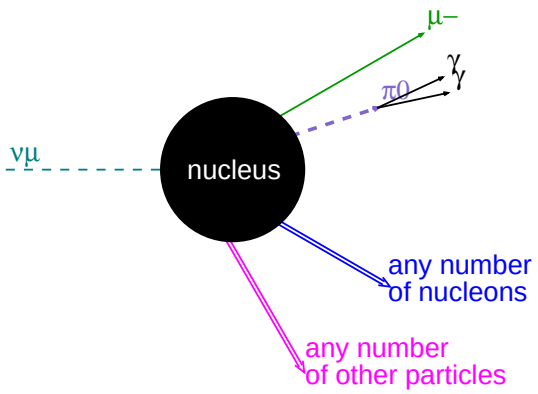

Figure 1: $(\nu_\mu CC\pi^0)_{incl.}$ reaction definition.

multiplicity, types and momenta of produced particles. Thus, this analysis will help to tune better those aspects of the Monte Carlo (MC) generators that describe neutrino interactions.

This thesis is composed of six chapters. The first chapter serves as an introduction to the neutrino-nucleus interaction model involving the nuclear model, neutrino primary interactions and secondary interactions in the target nucleus. The second chapter succinctly describes the T2K experiment. The software and data samples used in this analysis are introduced in Chapter 3. The next three chapters contain the $(\nu_\mu CC\pi^0)_{incl.}$ analysis results. Chapter 4 describes the selection criteria of the signal events in the tracker part of the ND280 detector. The total flux-averaged cross-section calculation is presented in Chapter 5. Chapter 6 delineates the systematic errors related to the neutrino flux, MC interaction model and detector response. The paper concludes with a short summary of the $(\nu_\mu CC\pi^0)_{incl.}$ analysis results and the outlook on further analysis.

Chapter 1

Neutrino physics

1.1 Neutrinos in the Standard Model

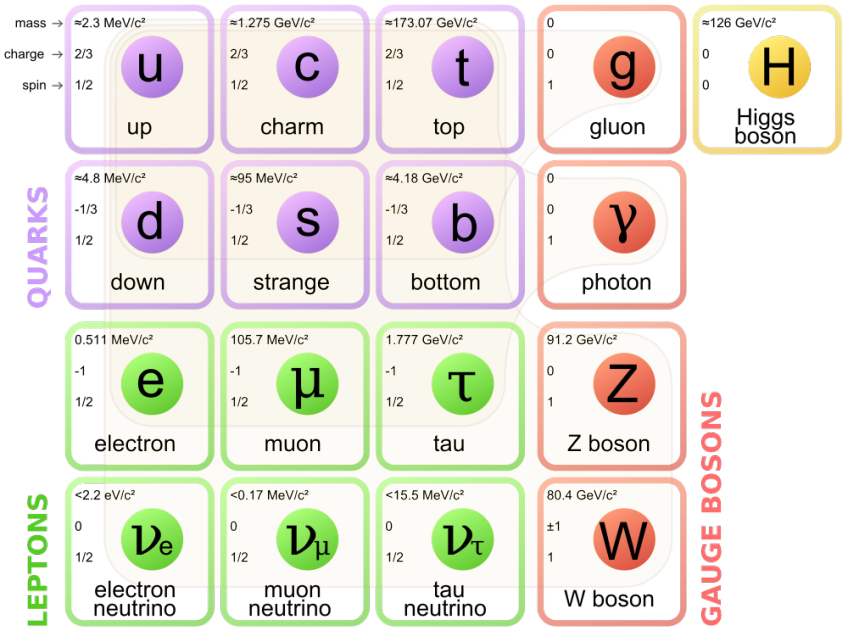

Figure 1.1: Elementary particles of matter and gauge bosons [3].

For more than 40 years the Standard Model (SM) has been the best model describing the structure of matter, and allowing to predict many phenomena in particle physics. The Standard Model predictions agree with almost all observations. SM assumes that matter consists of elementary particles with spin 1/2 (called fermions) and the interactions between them are mediated by

the particles with integer spins (called bosons) (Fig. 1.1).

There are four fundamental interactions:

- gravitational – negligible in particle physics,
- electromagnetic – mediated by photons (γ),
- strong – mediated by eight gluons, e.g. responsible for confining quarks into hadrons, such as protons and neutrons,
- weak – mediated by massive bosons $W^{\pm}$ of mass about 80 GeV and Z^0 of mass about 91 GeV; it is a short range and a relatively weak interaction.

Fermions are divided into two groups: quarks, which undergo all interactions, strong, weak and electromagnetic, and leptons, which do not participate in strong interactions. There are six types of quarks belonging to three generations, which are also called families. In each generation there is a pair of quarks, one with electric charge $+\frac{2}{3}e$ and one with $-\frac{1}{3}e$. Protons and neutrons which are composed of three light quarks (up and down quarks) make up ordinary nuclear matter. Leptons also belong to three generations. In each family there is one charged lepton (with charge $-1e$) and one neutral lepton (neutrino) corresponding to the charged lepton. The lightest charged lepton is an electron (e) and it is accompanied by electron neutrino (ν_e). Heavier and unstable charged leptons are muon (μ) and taon (τ) and the corresponding neutral leptons are muon neutrino (ν_μ) and taon neutrino (ν_τ), respectively. Additionally, each elementary particle has its antiparticle with the same mass but opposite charge, and other quantum numbers according to the CPT theorem.

Neutrinos, as neutral leptons, are affected only by the weak force, therefore they penetrate matter unimpeded and are difficult to detect. Since the first detected neutrino interaction in 1956 [4], our knowledge about these mysterious particles has been gradually growing, but there are still some open questions to be answered.

1.2 Neutrino oscillations

Neutrino oscillations is a quantum-mechanical phenomenon in which neutrinos change their flavour from one to another while propagating in space. This

results from the fact that the neutrino flavour eigenstates $(\nu_e, \nu_\mu, \nu_\tau)$ are linear combinations of mass eigenstates (ν_1, ν_2, ν_3) and their masses (m_1, m_2, m_3) are different from each other. This means that at least two of the neutrino mass values are non-zero.

The relation between flavour and mass eigenstates is given by the Pontecorvo-Maki-Nakagawa-Sakata (PMNS) unitary mixing matrix U:

$$\begin{pmatrix} \nu_e \\ \nu_\mu \\ \nu_\tau \end{pmatrix} = U \begin{pmatrix} \nu_1 \\ \nu_2 \\ \nu_3 \end{pmatrix} \tag{1.1}$$

The U matrix can be parametrized by three real numbers called mixing angles $(\theta_{12}, \theta_{13}, \theta_{23})$ and one[1] imaginary phase (δ_{CP}) responsible for CP asymmetry in the lepton sector:

$$U = \underbrace{\begin{pmatrix} 1 & 0 & 0 \\ 0 & c_{23} & s_{23} \\ 0 & -s_{23} & c_{23} \end{pmatrix}}_{\text{atmosferic neutrino oscillation}} \begin{pmatrix} c_{13} & 0 & s_{13}e^{-i\delta} \\ 0 & 1 & 0 \\ -s_{13}e^{i\delta} & 0 & c_{13} \end{pmatrix} \underbrace{\begin{pmatrix} c_{12} & s_{12} & 0 \\ -s_{12} & c_{12} & 0 \\ 0 & 0 & 1 \end{pmatrix}}_{\text{solar neutrino oscillation}} \tag{1.2}$$

where $c_{ij} = \cos\theta_{ij}, s_{ij} = \sin\theta_{ij}$ and $\delta = \delta_{CP}$.

The last two independent parameters describing the probabilities for neutrino oscillations are the differences in neutrino mass values: $\Delta m^2_{21} = m^2_2 - m^2_1$ and $\Delta m^2_{32} = m^2_3 - m^2_2$.

The current values of the oscillation parameters [2] are as follows:

$$\begin{aligned} \sin^2 2\theta_{12} &= 0.857 \pm 0.024 \\ \sin^2 2\theta_{23} &= > 0.95 \\ \sin^2 2\theta_{13} &= 0.095 \pm 0.010 \\ \Delta m^2_{21} &= (7.50 \pm 0.20) \times 10^{-5}\ eV^2 \\ |\Delta m^2_{32}| &= (2.32^{+0.12}_{-0.08}) \times 10^{-3}\ eV^2 \\ \delta_{CP} &= ? \end{aligned} \tag{1.3}$$

The questions in neutrino oscillations still waiting for the answer are:

- the value of δ_{CP},

[1] There is one imaginary CP phase if neutrinos are Dirac particles and additional two if they are Majorana particles. Oscillations are not sensitive to the Majorana phases.

- the sign of Δm^2_{32}, which defines the neutrino mass hierarchy: $m_1 < m_2 < m_3$ for Normal Hierarchy (NH) or $m_3 < m_1 < m_2$ for Inverted Hierarchy (IH),

- the octant of the θ_{23} angle ($\theta_{23} \leq 45°$ or $\theta_{23} \geq 45°$).

The large difference between Δm^2_{21} and Δm^2_{32} makes it possible to use the two-flavour approximation for the so called atmospheric and solar neutrino oscillations, i.e. to take only part of matrix U into account and use the simplified oscillation formula:

$$P(\nu_\alpha \to \nu_\beta) \approx \sin^2 2\theta \sin^2 \left(1.267 \frac{\Delta m^2 L}{E} \frac{GeV}{eV^2 km}\right), \tag{1.4}$$

where

- $P(\nu_\alpha \to \nu_\beta)$ – probability that the neutrino produced with flavour α will be observed as the neutrino of a different flavour β,

- θ – mixing angle (θ_{23} for atmospheric and θ_{12} for solar neutrino oscillation),

- Δm^2 – mass square difference in eV^2 (m^2_{23} for atmospheric and m^2_{12} for solar neutrino oscillation),

- L – distance travelled by the neutrino in km,

- E – energy of the neutrino in GeV.

Neutrino oscillation studies entered an era of precision measurements, which requires a very good knowledge of neutrino interactions and neutrino fluxes. This is why oscillation studies with atmospheric (solar) measurements have been almost entirely replaced with studies of the artificially produced accelerator (reactor) neutrinos.

The analysis presented in this thesis is based on the accelerator neutrino beam produced in the J-PARC (Japan Proton Accelerator Research Complex) in Japan.

1.3 Neutrino interactions

Knowledge of neutrino cross-sections is crucial for precise measurements in oscillation experiments, as it is one of the main sources of systematic errors. Figure 1.2 depicts the compilation of neutrino and antineutrino cross-section measurements. For intermediate energies (0.1-20 GeV) multiple processes play an important role and the available measurements are not sufficient. This issue is even more complex, because the nucleons undergoing neutrino interactions are usually parts of nucleus, which means that they are not at rest, but have a non-zero momentum which must be taken into account. A neutrino primary interaction can happen on an entire nucleus, on a single nucleon bound in a nuclear potential, or on a parton. This requires a good nuclear model, which describes the behaviour of a single nucleon in a nucleus and quantum chromodynamics to describe the nucleon structure. Subsequently, the products of the neutrino primary interactions on a nucleon or parton are propagated through nuclear medium, where they can interact with other nucleons before leaving the target nucleus. These are the so called Final State Interactions (FSI). All that causes modifications in neutrino interaction cross-sections and changes in the types, multiplicity and momenta of the observed particles. In the following subsections the neutrino interactions will be described in more detail. Antineutrinos undergo analogical processes.

1.3.1 Nuclear models

Nucleons inside nuclei are not free particles. They are bound in the nuclear potential and can interact with each other. More or less sophisticated models of this phenomenon are implemented in neutrino event generators.

The simplest one, the Fermi Gas (FG) model [5] illustrated in Fig. 1.3, assumes that the nucleons are in an average nuclear potential and are independent of each other, except for the Pauli exclusion principle[2]. The nuclear potential is assumed to be a rectangular well, deeper for neutrons than for protons, which is due to the protons' electromagnetic repulsion. The protons and neutrons in such a well occupy discrete energy levels up to the Fermi energy, which actually can happen only in the temperature of absolute zero.

[2]The Pauli exclusion principle states that in a nucleus two identical fermions cannot occupy the same quantum state simultaneously.

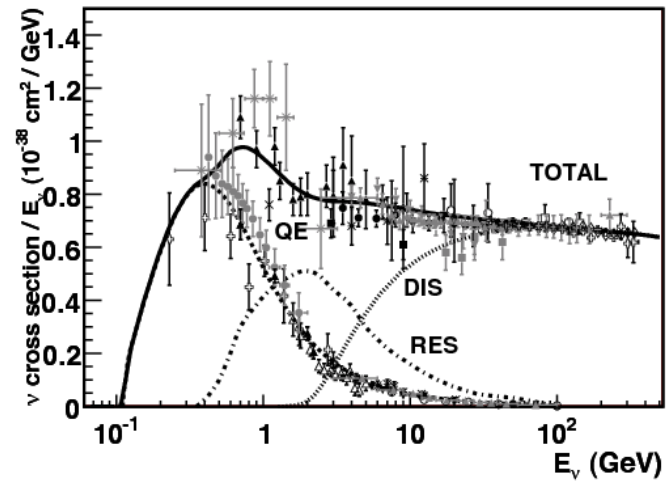

(a)

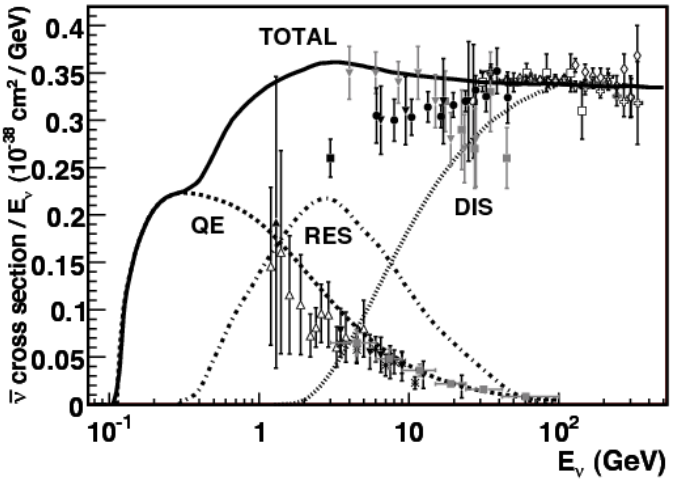

(b)

Figure 1.2: Total (solid line) neutrino (a) and antineutrino (b) Charged Current (CC) cross-section per nucleon divided by (anti)neutrino energy as a function of this energy [1]. Contributions from CC Quasi-Elastic (CCQE – dashed), Resonance production (RES – dot-dash) and Deep Inelastic Scattering (DIS – dotted) are also shown. Description of these processes is in further part of this section.

The most natural extension of this model is the Relativistic Fermi Gas (RFG) model that uses relativistic formulas in kinematic equations.

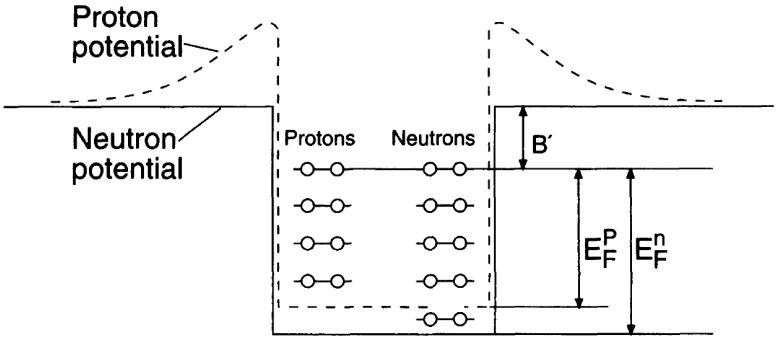

Figure 1.3: Nuclear potential for protons and neutrons in the Fermi Gas Model [5]. The neutron potential results from the strong interaction between the neutron and the nucleus. The proton potential is a combination of the attractive strong potential and repulsive electromagnetic potential of the nucleus. E_F^p is the protons' Fermi energy; E_F^n is the neutrons' Fermi energy; B' is their binding energy, i.e. it is the energy needed to separate the nucleon from the nucleus.

The most popular among nuclear models is the Spectral Function (SF) model [6, 7]. The SF model determines momentum probability density taking into account the nuclear shell structure model and incorporating short-range correlations between nucleons based on an advanced many-body approach. The probability distribution of the nucleon momentum for both models is shown in Figure 1.4. The SF model predicts the occurrence of nucleons with momenta much higher than the Fermi momentum. An additional consequence is the existence of interactions with two knocked-out nucleons for a neutrino interaction with one nucleon from a strongly correlated pair. The nucleons in such pairs have high relative momenta, which allow also the spectator nucleon to leave the nucleus. Spectral functions for particular nuclei are obtained from electron scattering measurements.

Both the RFG and SF introduced nuclear models indicate that nucleons, as parts of the nucleus, are not at rest, but have non-zero momenta, and this fact has a significant influence on the neutrino interaction cross-sections and momenta of the produced particles.

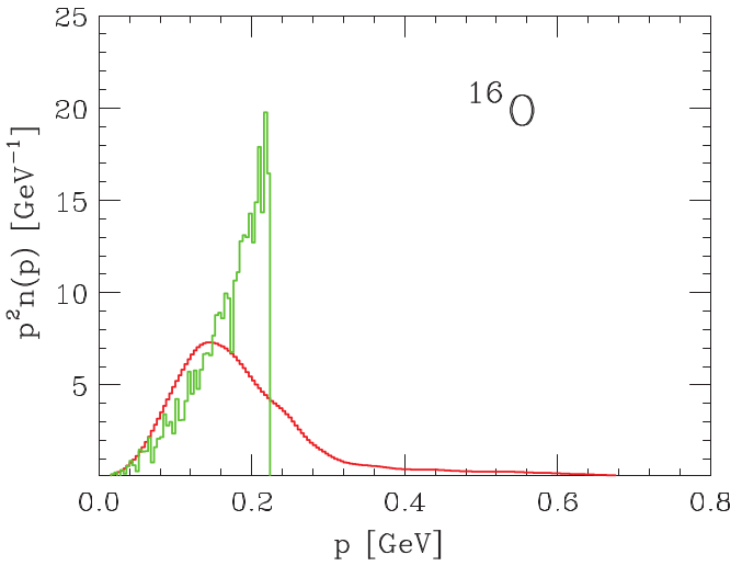

Figure 1.4: Probability distribution of nucleon momentum in oxygen calculated from the Spectral Function model (red) and from the Relativistic Fermi Gas model (green) [7].

1.3.2 Neutrino primary interactions

There are several types of neutrino interactions depending on the products of the interaction and the way they are produced. The neutrino interactions can be divided with respect to the exchanged boson. A neutrino exchanging the Z^0 boson undergoes the so called Neutral Current (NC) interaction and remains in the final state. The $W^{\pm}$ boson is exchanged in the so called Charged Current (CC) neutrino interaction. In such an interaction the neutrino changes into a charged lepton from the same family as the neutrino. The NC and CC interactions are further divided in the following way [1,8]:

- In the Neutral Current Elastic (NCE) and Charged Current Quasi-Elastic (CCQE) interactions the neutrino scatters on an entire nucleon, which is usually knocked out of the target nucleus:

$$\begin{aligned} \nu + N &\rightarrow \nu + N \qquad (NCE) \\ \nu_l + n &\rightarrow l^- + p \qquad (CCQE), \end{aligned} \tag{1.5}$$

  where N denotes a proton or neutron. The CCQE reaction is particularly important in the neutrino oscillation analyses, because within this reaction one can reconstruct the neutrino type and energy E_ν (Eq. 2.1). For muon neutrinos, CCQE dominates for E_ν below 1 GeV. According to

the Llewellyn-Smith formalism [9], the cross-section depends on the vector and axial form factors. The vector form factor is obtained from the electron scattering measurements. The axial form factor F_A is assumed to have a dipole form:

$$F_A(Q^2) = \frac{g_A}{\left(1 + Q^2/M_A^2\right)^2}, \tag{1.6}$$

where Q^2 is a square of the four-momentum transfer, g_A is an empirical parameter measured in beta decay and M_A is the only unknown parameter called the axial mass. In NCE interactions [1, 10] additional coupling factors and the contribution from strange quarks must be taken into account.

- In the NC and CC Resonance production (RES) the neutrino excites the nucleon to a baryonic resonance, usually Δ (1232). The resonance decays back to a nucleon, which is most often accompanied by a single pion:

$$\begin{aligned}
\nu + p &\rightarrow \nu + p + \pi^0 \\
\nu + p &\rightarrow \nu + n + \pi^+ \\
\nu + n &\rightarrow \nu + n + \pi^0 \\
\nu + n &\rightarrow \nu + p + \pi^- \\
\nu_l + p &\rightarrow l^- + p + \pi^+ \\
\nu_l + n &\rightarrow l^- + p + \pi^0 \\
\nu_l + n &\rightarrow l^- + n + \pi^+
\end{aligned} \tag{1.7}$$

  Higher resonances can also be produced and decay into a single pion, multiple pions, kaon, eta meson or photon. The most common description of a single pion production through baryon resonances is the Rein-Sehgal model [11]. In this model 18 resonances with masses below 2 GeV are considered together with the possible interferences between them and a simple non-resonant background of isospin 1/2.

- The Deep Inelastic Scattering (DIS) is possible at higher energies for which the neutrino can resolve the internal structure of a nucleon and interact with individual partons. The struck nucleon is broken up. Its fragments hadronise and form a jet of hadrons, which are in a great part

pions:

$$\begin{aligned} \nu + A &\rightarrow \nu + X \\ \nu_l + A &\rightarrow l^- + X, \end{aligned} \tag{1.8}$$

where A denotes the target nucleus and X denotes hadronic jet. Therefore, DIS interactions are characterized by higher energies and usually higher multiplicities of the produced particles. DIS dominates for neutrino energies above 10 GeV and then grows linearly with the neutrino energy.

- In Coherent pion production (COH) the neutrino scatters on the entire nucleus, producing a single pion:

$$\begin{aligned} \nu + A &\rightarrow \nu + A + \pi^0 \\ \nu_l + A &\rightarrow l^- + A + \pi^+. \end{aligned} \tag{1.9}$$

  In the COH interactions the nucleus remains in the ground state and the pion is produced at a small angle with respect to the incident neutrino direction. The NC COH reaction can be especially dangerous in the oscillation analyses, because π^0 can mimic an electron from electron neutrino interaction.

- In the multinucleon interactions the neutrino interacts with more than one nucleon, which are usually ejected out of the target nucleus. These interactions increase the total neutrino cross-section and can be responsible for the excess of the real data events identified as CCQE in the MiniBooNE experiment, because nucleons are usually below a reconstruction threshold [12–15]. This type of interactions is dominated by Meson Exchange Current (MEC) mechanism, in which a neutrino interacts with two nucleons simultaneously and a virtual meson is exchanged between the nucleons.

1.3.3 FSI interactions

The products of the neutrino primary interaction can reinteract inside the target nucleus. These are the so called Final State Interactions (FSI). At low neutrino energies, for π mesons, which are the most frequently produced particles in the primary interactions, the most common FSI are: the elastic

scattering ($\pi + N \rightarrow \pi + N$), pion absorption ($\pi + N \rightarrow N'$) and charge exchange reactions ($\pi^+ + n \leftrightarrow \pi^0 + p$, $\pi^- + p \leftrightarrow \pi^0 + n$). Consequently, the multiplicity, types and energies of particles produced directly in the neutrino primary interaction can significantly differ from those leaving the nucleus.

Examples of the primary ν_μ interactions, classified as belonging to the $(\nu_\mu CC\pi^0)_{incl.}$ reaction, studied in this thesis, are given in Figure 1.5. For the $\nu_\mu CC\mu^-\pi^0 p$ reaction in Fig. 1.5(a) the neutrino exchanges the W^+ boson with a neutron and changes into a negative muon. The neutron turns into Δ^+ resonance, which decays into a proton and a π^0. A neutral pion, accompanied or not by other particles, can also be produced directly in the non-resonant or DIS interactions, which are illustrated in Fig. 1.5(b) and 1.5(c), respectively.

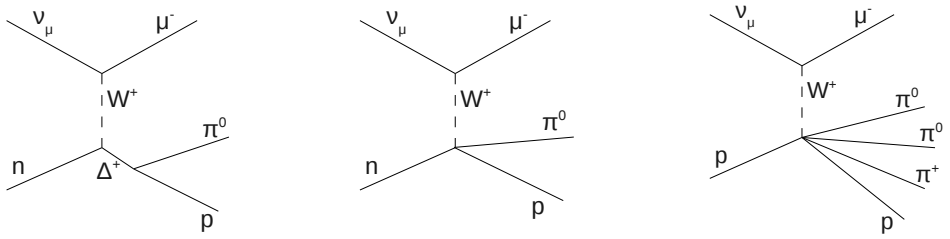

(a) (b) (c)

Figure 1.5: Examples of the $(\nu_\mu CC\pi^0)_{incl.}$ reaction on a single nucleon. The plot (a) depicts resonance $\nu_\mu CC\mu^-\pi^0 p$ reaction, plot (b) – non resonance $\nu_\mu CC\mu^-\pi^0 p$ reaction, and plot (c) – DIS $\nu_\mu CC\mu^- 2\pi^0\pi^+ p$ reaction.

The impact of FSI on the $(\nu_\mu CC\pi^0)_{incl.}$ interaction is illustrated in Figure 1.6. Figures 1.6(a) and 1.6(b) depict two reactions with the same set of particles after FSI $(\mu^-, \pi^0, p, 2n)$, but corresponding to different types of the neutrino primary interactions. In the first case π^0 is produced in the primary $\nu_\mu CC\mu^-\pi^0 p$ reaction. In the second one, the primary interaction is $\nu_\mu CC\mu^-\pi^+ n$, but π^+ undergoes charge exchange and π^0 leaves the nucleus. Two other plots, 1.6(c) and 1.6(d), show the situation where in the neutrino primary reaction a neutral pion is produced, but π^0 does not leave the nucleus because of charge exchange. Such reactions are classified as a signal for the definition based on the neutrino primary interaction products, but they will fall into a background category if the reaction definitions are based on particles leaving the target nucleus.

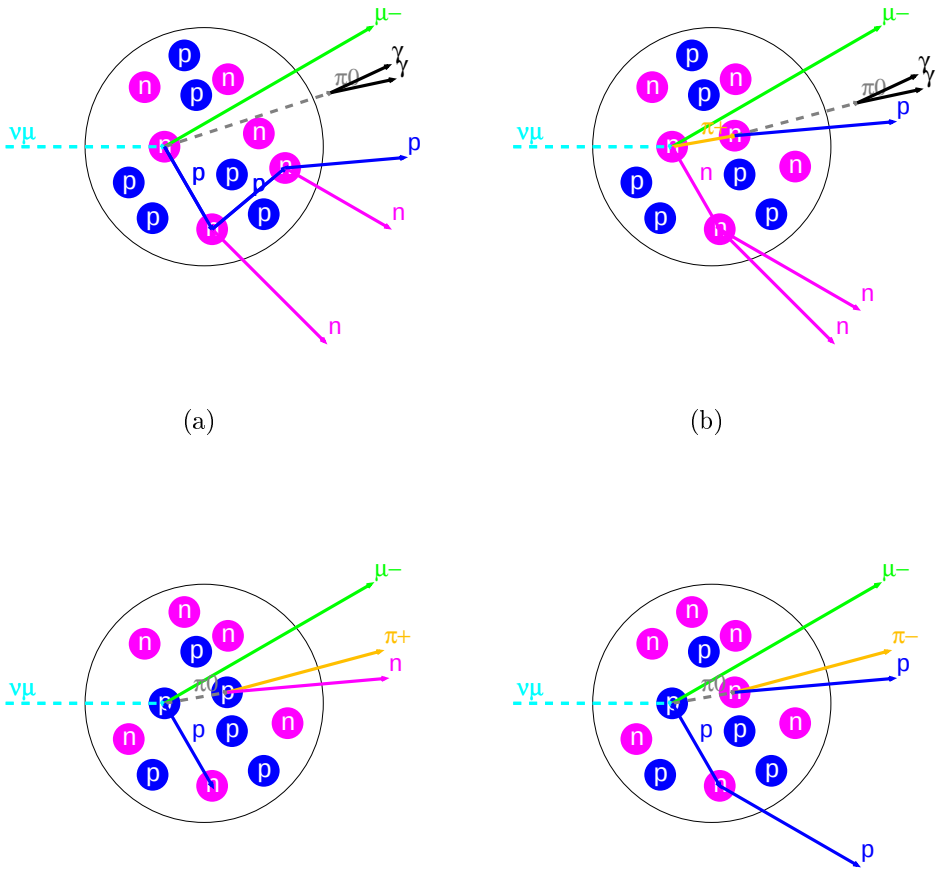

Figure 1.6: Illustration of the impact of FSI on the $(\nu_\mu CC\pi^0)_{incl.}$ reaction. The plot (a) shows primary $\nu_\mu CC\mu^-\pi^0 p$ reaction classified as the $(\nu_\mu CC\pi^0)_{incl.}$ reaction, the plot (b) – primary $\nu_\mu CC\mu^-\pi^+ n$ reaction classified as the $(\nu_\mu CC\pi^0)_{incl.}$ reaction, the plots (c) and (d) – primary $\nu_\mu CC\mu^-\pi^0 p$ reaction classified as the background: $\nu_\mu CC1\pi^+$ and $\nu_\mu CC1\pi^-$ respectively.

1.3.4 Reaction definitions

Because of FSI, the definition of the reaction types requires further specification. We can consider either products of the neutrino primary interaction or particles after FSI. In this thesis, if not stated otherwise, all reaction definitions are based on particles leaving the nucleus, because they can be observed in the detector. All the considered reaction types are listed in Table 1.1. It was also decided that the type and number of nucleons would not be considered, so in the reaction definitions the term *nucleons* means $0, 1, 2$ or more nucleons. It should be noted that the signal reaction $(\nu_\mu CC\pi^0)_{incl.}$ consists of two sub-reactions, $\nu_\mu CC1\pi^0$ and $\nu_\mu CC\pi^0 + X$, defined in the Table.

The analysis presented in this thesis is the first measurement of the $(\nu_\mu CC\pi^0)_{incl.}$ interaction cross-section and with higher data statistics it should help to test physics models of Resonance production (RES), DIS and FSI.

Abbreviation	Definition	Annotations
	Signal reactions	
$CC1\pi^0$	$\nu_\mu + nucleon \rightarrow \mu^- + nucleons + \pi^0$	
$CC\pi^0 + others$	$\nu_\mu + nucleon \rightarrow \mu^- + nucleons + \pi^0 + others$	the *others* can include π^0
	Background reactions	
$CCsec\pi^0$ (secondary π^0)	$\nu_\mu + nucleon \rightarrow \mu^- + nucleons + others$	none of the *others* is π^0, but produce π^0
$CCQE$	$\nu_\mu + nucleon \rightarrow \mu^- + nucleons$	
$CC + others$	$\nu_\mu + nucleon \rightarrow \mu^- + nucleons + others$	the *others* do not include π^0
$NC1\pi^0$	$\nu_\mu + nucleon \rightarrow \nu_\mu + nucleons + \pi^0$	
$NC\pi^0 + others$	$\nu_\mu + nucleon \rightarrow \nu_\mu + nucleons + \pi^0 + others$	the *others* can include π^0
$NCsec\pi^0$ (secondary π^0)	$\nu_\mu + nucleon \rightarrow \nu_\mu + nucleons + others$	none of the *others* is π^0 , but produce π^0
NCE	$\nu_\mu + nucleon \rightarrow \nu_\mu + nucleons$	
$NC + others$	$\nu_\mu + nucleon \rightarrow \nu_\mu + nucleons + others$	the *others* do not include π^0
not ν_μ	interactions of $\overline{\nu}_\mu$, ν_e and $\overline{\nu}_e$	

Table 1.1: Reaction definitions based on particles leaving the nucleus. The abbreviations listed in the first column are used in the plot legends and tables discussed later in this thesis. Secondary neutral pions, labelled as $sec\pi^0$, are π^0's produced through secondary interactions or decays outside the target nucleus. To make plots more clear, all NC reactions are put together and labelled NC in part of the plots.

Chapter 2

T2K experiment

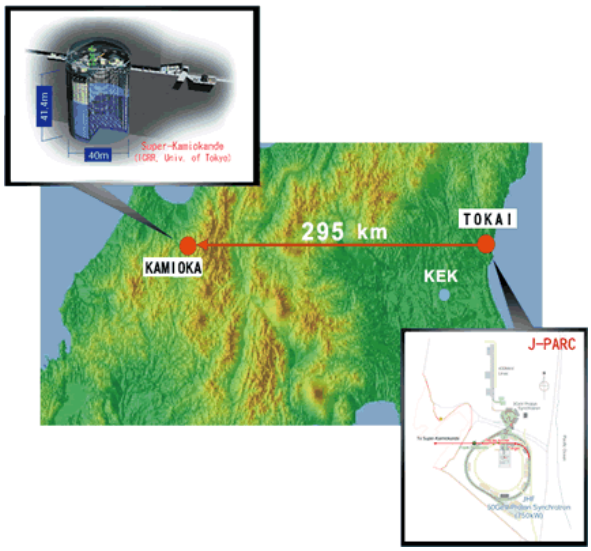

Figure 2.1: Overview of the T2K experiment.

The T2K (Tokai to Kamioka) experiment [16, 17] (Fig. 2.1) is a long baseline neutrino oscillation experiment, performed in Japan by an international collaboration of approximately 500 people from 59 institutions in 11 countries. The muon neutrino and the muon antineutrino beams are produced in the Japan Proton Accelerator Research Complex (J-PARC) in Tokai village on the Japanese east coast. After travelling 280 m, yet before the oscillations occur, the beam goes through the complex of two detectors [18, 19], INGRID (Interactive Neutrino GRID) and ND280 (Near Detector at 280 m) [20]. After passing another 295 km to the west the neutrino beam crosses the far detector, Super-Kamiokande (SK) [21], in Kamioka. The INGRID near detector is

placed on the beam axis, while the ND280 near detector and the SK detector are located 2.5° away from the neutrino beam axis. The scientific goals of this experiment are: the measurement of the disappearance of (anti)muon neutrinos, appearance of electron (anti)neutrinos in the muon (anti)neutrino beam, neutrino-nucleus cross-section measurements, search for sterile neutrinos and, in the longer term, investigation of the CP violation in the neutrino sector.

The neutrino beam production, the near detectors and the far detector are shortly described below.

2.1 Neutrino beam

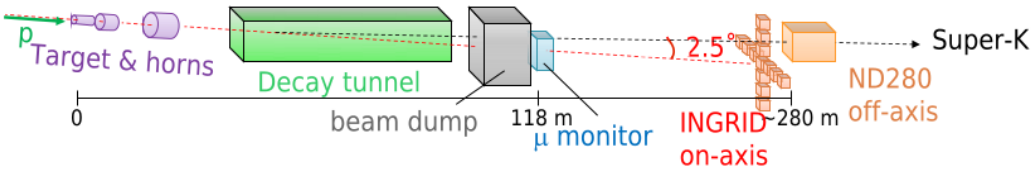

Figure 2.2: Overview of the T2K neutrino beamline and near detectors [22].

The T2K neutrino beam is produced at J-PARC in Tokai village on the east coast of Japan. The scheme of the T2K neutrino beamline is presented in Figure 2.2. First, the protons are propelled to 30 GeV by the system of accelerators. Every 2.5 to 3.5 seconds, depending on the run period, the protons are extracted as a spill and hit a graphite target. The spill width is 5.5 μs and it contains 8 bunches (6 by June 2010), each 58 ns wide. The particles produced in the collisions with the target are mainly pions ($\sim 90\%$) and kaons ($\sim 10\%$). In order to produce the ν_μ beam, three magnetic horns focus positive particles and direct them to a decay tunnel, where positively charged mesons decay mainly into positively charged muons and muon neutrinos. It is also possible to reverse the current in the horns to focus negative particles and get the muon antineutrino beam. The remaining particles, except for neutrinos, are stopped by the beam dump and in the surrounding ground. The unimpeded beam of neutrinos travels farther through the set of near detectors (INGRID and ND280) and then the far detector Super-Kamiokande.

An important feature of the T2K experiment is the use of an off-axis beam. Such a beam has a narrower energy spectrum and the peak energy tuned

to maximise the ν_μ disappearance and ν_e appearance probabilities at the far detector (Fig. 2.3(a)). The off-axis configuration also helps to reduce the high energy background and decrease the ν_e contribution. The energy spectra of different types of neutrinos at the ND280 detector are shown in Figure 2.3(b).

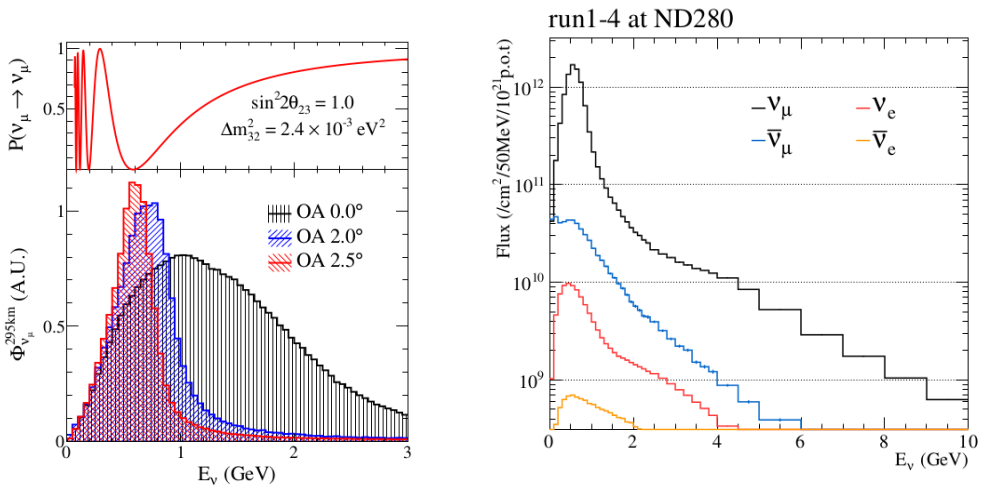

(a) (b)

Figure 2.3: (a) T2K neutrino beam energy spectrum at different angles and muon neutrino survival probability [23] and (b) the predicted neutrino flux at the ND280 detector for ν_μ signal and ν_e, $\overline{\nu}_\mu$ and $\overline{\nu}_e$ backgrounds [24].

2.2 Near detectors

The set of two near detectors is located 280 m away from the graphite target. The INGRID detector is centered on the neutrino beam axis. The ND280 detector is positioned 2.5° off the beam axis on its way to the far detector. Figure 2.4 presents a relative location of the two near detectors in the detector shaft.

2.2.1 On-axis near detector INGRID

The INGRID detector is located at the centre of the neutrino beam. INGRID consists of 16 identical modules composed of iron and plastic scintillator layers. The configuration of the modules is shown in Figure 2.5: 7+7 modules form a "cross" and two extra modules are placed outside the cross. The neutrino beam

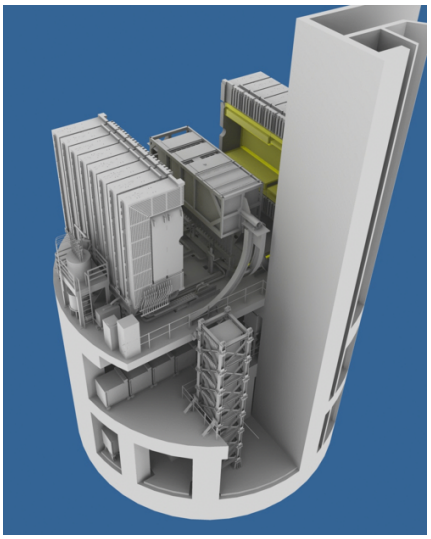

Figure 2.4: Overview of the T2K near detector complex.

axis goes through the centre of the cross. An additional module, consisting of scintillator layers only, is placed at the beam centre, between the vertical and horizontal modules.

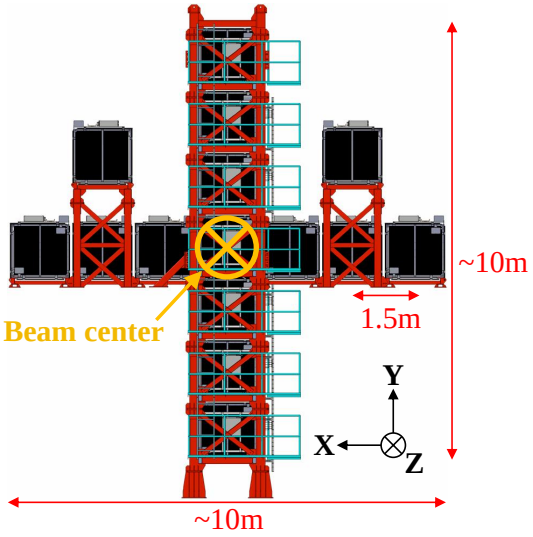

Figure 2.5: INGRID detector scheme.

The energy spectrum of the off-axis beam changes depending on the off-axis angle. Therefore, the main goal of the INGRID detector is the day-to-day monitoring of beam position, direction and intensity. INGRID also measures the neutrino cross-sections on iron and carbon at the energies higher than the

off-axis beam energy, taking an advantage of a higher intensity of the on-axis neutrino beam.

2.2.2 Off-axis near detector ND280

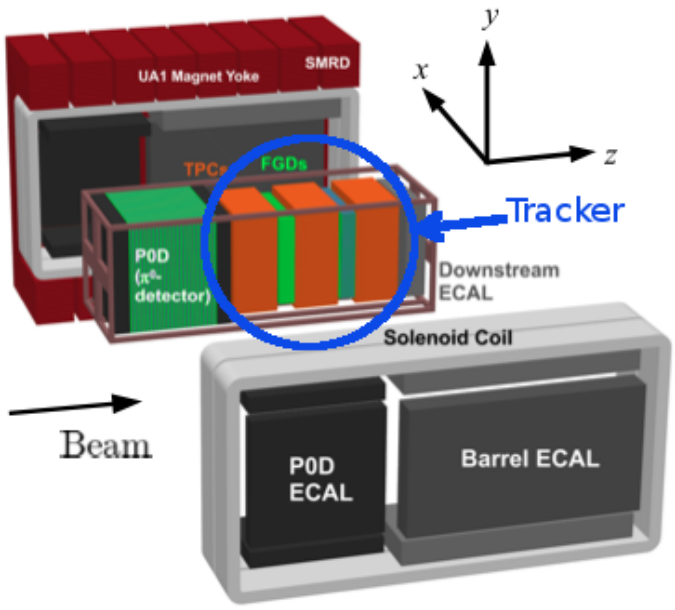

Figure 2.6: ND280 detector scheme.

The ND280 detector, positioned 2.5° away from the beam axis, is a magnetised detector consisting of a number of specialised subdetectors, configured as it is shown in Fig. 2.6. The Pi-Zero Detector (P0D) and the tracker form the so called basket, i.e. the inner part of the ND280 detector. P0D [25] consists of a plastic scitillator, lead and water layers and is optimised for the reconstruction of neutral pions from the NC interactions. The tracker consists of three Time Projection Chambers (TPCs) [26] and two Fine Grained Detectors (FGDs) [27] in between them. FGD1, placed more upstream the neutrino beam, is entirely built of plastic scintillator. In FGD2 the scintillator layers are sandwiched with water layers. FGDs serve as a target for neutrino interactions and allow the reconstruction of the neutrino vertex position and short range particles leaving it. TPCs are filled with a mixture of gases, whose main component is argon (95%), and precisely reconstruct the charges, mo-

menta and directions of charged particles. The tracker is optimised towards the selection of the CC neutrino interactions. The basket part is surrounded by a set of three Electromagnetic Calorimeters (ECals) [28]. The calorimeter around P0D is called P0DECal or PECal and, together with the calorimeter around the tracker (TECal), it composes the Barrel Electromagnetic Calorimeter (BrECal). The Downstream Electromagnetic Calorimeter (DsECal) is perpendicular to the neutrino beam and adheres to the most downstream TPC (TPC3). All calorimeters consist of plastic scintillator layers sandwiched with lead. PECal has 4.5 radiation lenghts, TECal – 10.5 and DsECal – 11. TECal and DsECal are essential in the reconstruction of neutral pion decay products leaving the tracker region. BrECal is surrounded by a magnet generating a homogeneous magnetic field of 0.2 T. The magnet is instrumented with scintillators to measure muon tracks at large angles – Side Muon Range Detector (SMRD) [29]. The coordinate system used in the ND280 geometry is dextrorotary with the Z axis parallel to the neutrino beam direction and the Y axis pointing upwards. This system is used in each plot containing spatial coordinates or angles.

ND280 is designed to measure the neutrino cross-sections on different nuclear targets, as well as to determine the off-axis neutrino flux and flavour composition at the 2.5° angle. These measurements significantly reduce systematic errors in the oscillation analysis. Because of the ND280 constraints, the effect of the total systematic error on the predicted event rate in the far detector decreases from 23.5% to 7.7% for ν_μ CC events and from 26.8% to 6.8% for ν_e CC events [30]. Figure 2.7 depicts the total systematic error envelopes for the energy distributions of these events.

The analysis described in this thesis focuses on the events corresponding to the $(\nu_\mu CC\pi^0)_{incl.}$ reaction with the neutrino interaction vertex in the FGD1 Fiducial Volume (FV), defined later in Table 4.2 and shown in Fig. 4.3, with the produced particles traversing the tracker section of the ND280 near detector and the surrounding calorimeters. An example of the $\nu_\mu CC\mu^-\pi^0 p$ event in the ND280 tracker is shown in Figure 2.8. The neutrino interacts with a nucleus inside the FGD1 and produces μ^-, p and π^0. The negative muon, which is usually the highest momentum particle, leaves the long track starting at the vertex. As the particle crosses the TPC, it is possible to measure its charge and momentum from the track curvature and to identify it through its energy deposit per unit distance (dE/dx). The neutral pion decays immediately at the

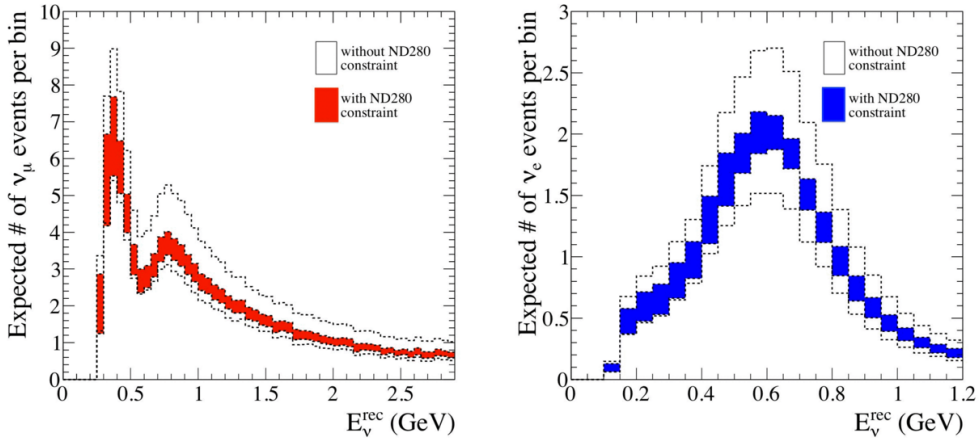

(a) (b)

Figure 2.7: Total systematic error envelopes for the reconstructed energy distributions of ν_μ CC (a) and ν_e CC (b) candidate events in the far detector, with and without the ND280 constraint [30].

vertex into two photons. The photon, converting in one of the FGD detectors or in the TPC outer structure, produces an electron-positron pair, which may be observed in the TPC. If the conversion occurs inside the ECal, it manifests itself there as a shower. In the $(\nu_\mu CC\pi^0)_{incl.}$ reaction μ^- and π^0 can be accompanied by any number of nucleons and other particles (mainly charged pions), but the selection performed in this analysis is not oriented towards them.

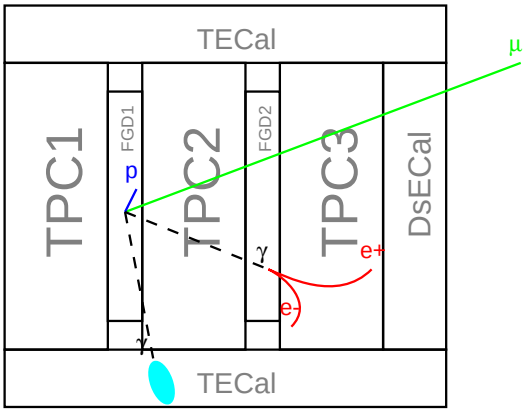

Figure 2.8: Example of the $\nu_\mu CC\mu^-\pi^0 p$ reaction visualised in the ND280 detector.

The analysis relies on the information from the TPC, FGD, TECal and DsECal. Therefore, the reconstruction in these sub-detectors will be described more in detail [31].

1. The role of the TPC detectors is to measure the charge, momentum and energy loss of charged particles. It is the most accurate tracking sub-detector and the track reconstruction starts here. Firstly, the hits overlapping in time and consecutive in space in the same row (for horizontal track with $\theta < 55^0$) or in the same column (for vertical track with $\theta > 55^0$) are combined into nodes. Then, the nodes are joined together into tracks by a pattern recognition algorithm.

2. The FGD detectors serve as a target for neutrino interactions. They are also intended to register products of these interactions near the vertex. If the particle reaches the TPC, the TPC track is matched with FGD hits. The FGD hits without continuation in the TPC are matched together by a different algorithm.

3. One of TECal and DsECal functions is to register particles leaving the tracker region, which in a large part are photons from π^0 decays. The reconstruction in the ECal starts from joining hits into 2D clusters. Then, the 2D clusters are matched into 3D objects. Based on their shape and charge distribution, it is decided if these objects are track-like or shower-like.

4. In the end, the objects reconstructed in each of the sub-detectors are matched together and refitted by the global reconstruction of the ND280 detector.

2.3 Far detector Super-Kamiokande

The Super-Kamiokande (SK) detector [21] is a 50 kton water Cherenkov detector located 1000 m underground in the Mozumi mine (Fig. 2.9). It is instrumented with approximately 13000 photomultipliers to register charged particles from the neutrino and antineutrino interactions with water.

The particle identification is based on the shape of the Cherenkov light rings: sharp for muons and more fuzzy for electrons (Fig. 2.10). The detector

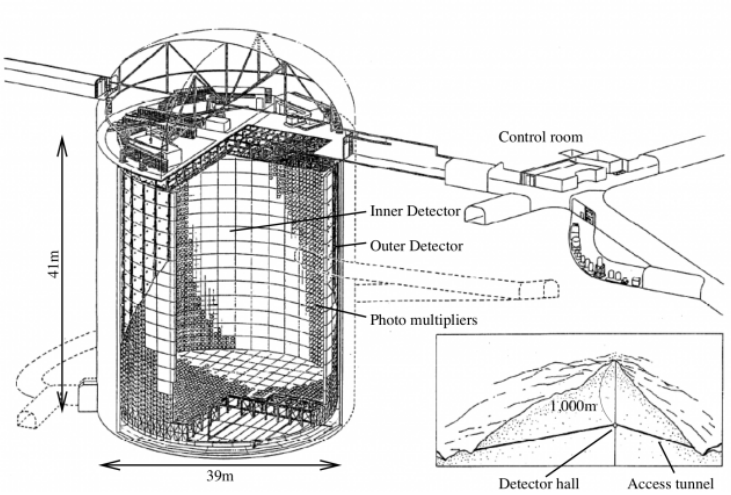

Figure 2.9: Super-Kamiokande detector scheme [32].

has no magnetic field, therefore it cannot distinguish particles from antiparticles. The ring analysis provides the information about the particle directions and energies. T2K studies neutrinos from the beam, for which the direction of the incoming neutrino is known, so the angle between the neutrino and the produced lepton can be easily calculated.

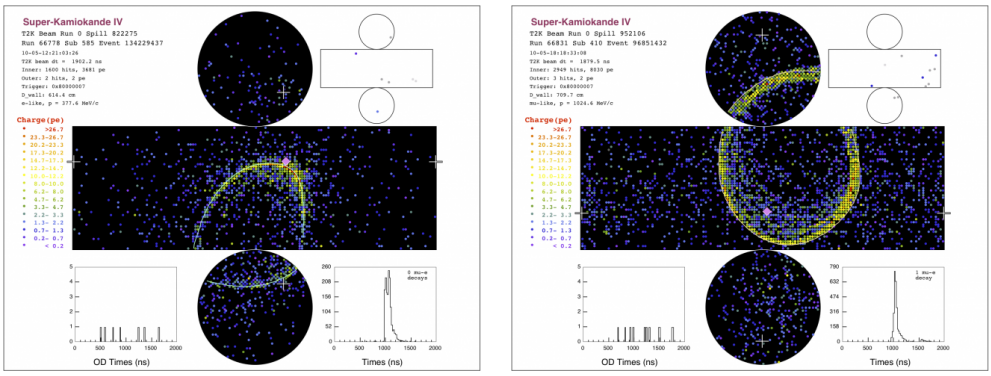

(a) (b)

Figure 2.10: Electron-like (a) and muon-like (b) events in the SK detector [32].

For the CC interactions the neutrino flavour can be reconstructed, and for the CCQE interaction also the neutrino energy E_ν can be determined from the formula:

$$E_\nu = \frac{E_l m_N - m_l^2/2}{m_N - E_l + p_l \cos\theta_l}, \tag{2.1}$$

where

- m_N – nucleon mass (proton and neutron masses are approximately the same),
- m_l – lepton mass,
- E_l – lepton energy,
- p_l – lepton momentum,
- θ_l – angle between the incoming neutrino and the produced lepton.

Information about the types and energy distribution of the neutrinos in the far detector is crucial in the oscillation analyses.

2.4 Main physics results

The T2K experiment is a world leading neutrino experiment, which has already delivered many important physics results. The most prominent of them are:

- First direct observation of the $\nu_\mu \rightarrow \nu_e$ oscillations at the level of 7.3σ. For the sample of 6.57×10^{20} POT the number of the expected ν_e background events in the case of no oscillation was 4.92 ± 0.55, and the measured number of events was 28 [30].
- The world's best measurement of the θ_{23} mixing angle. It was measured based on the difference between a measured muon neutrino spectrum and expectation for no oscillation hypothesis (see Fig. 2.11). The 68% confidence level (C.L.) on $\sin^2\theta_{23}$ is $0.514^{+0.055}_{-0.56}$ for NH and 0.511 ± 0.055 for IH [33]. The comparison of the results from T2K and other experiments is illustrated in Figure 2.12.
- First hint of the non zero δ_{CP} value. As shown in Fig. 2.13, combination of the T2K and reactor experiments measurements indicates the maximal CP violation with $\delta_{CP} = -\pi/2$ [30]. However, more antineutrino beam data are needed to obtain statistically significant result.

Apart from the oscillation analyses, T2K has already provided seven publications concerning cross-section measurements of muon and electron neutrinos

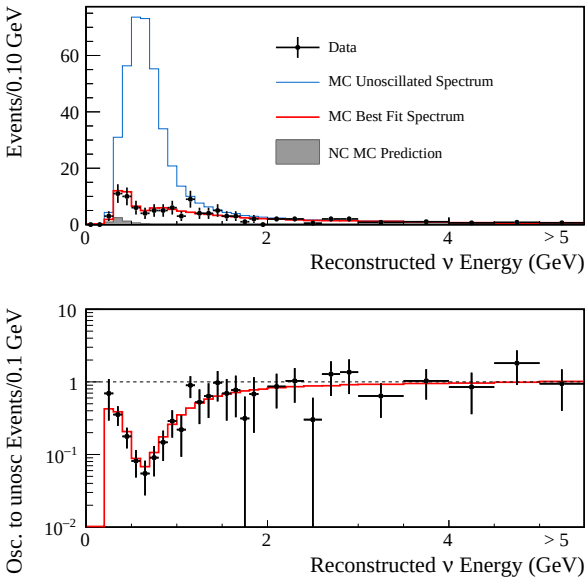

Figure 2.11: Reconstructed muon neutrino energy spectrum in the far detector for data, best-fit prediction and prediction for no oscillation (top) and the ratio to the prediction for no oscillation (bottom) [30].

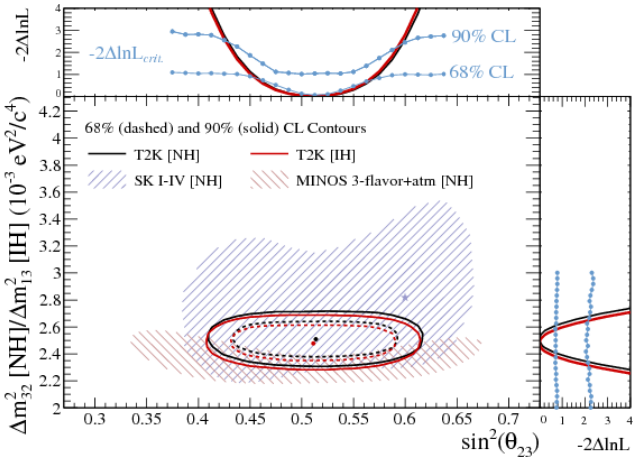

Figure 2.12: T2K 68% and 90% C.L. regions for $\sin^2\theta_{23}$ and Δm^2_{32} (NH) or Δm^2_{13} (IH). The SK and MINOS 90% C.L. regions for NH are shown for comparison [33].

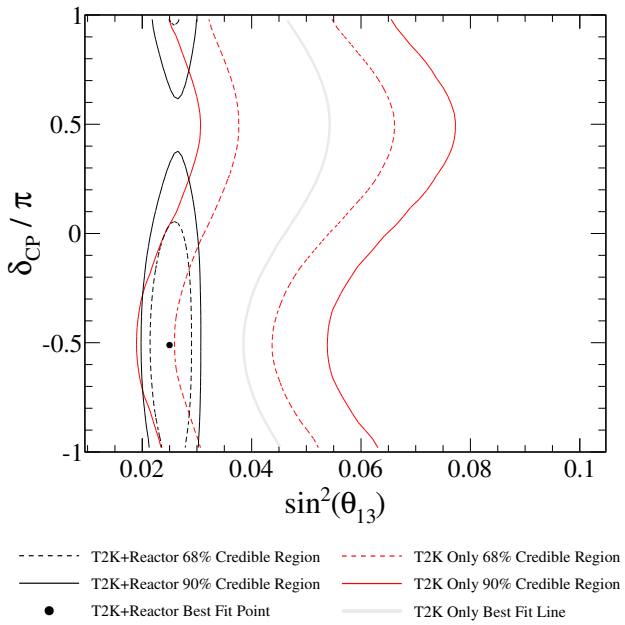

Figure 2.13: Credible regions for $\sin^2\theta_{13}$ and δ_{CP} for the T2K-only and T2K + reactor combined analyses for both hierarchies [30].

on a range of nuclear targets, such as: hydrocarbon, water and iron. A number of further cross-section publications is in preparation. For the analysis presented in this thesis the most important result is the total flux-averaged cross-section of the inclusive $\nu_\mu CC$ interaction [34], which equals

$$\langle\sigma\rangle^{CC} = (6.91 \pm 0.13(stat) \pm 0.84(sys)) \times 10^{-39}\ \text{cm}^2/\text{nucleon} \qquad (2.2)$$

for an average neutrino energy of 0.85 GeV.

Chapter 3

Software tools and data samples

3.1 Software tools

The ND280 software, including the reconstruction and analysis programmes, has been continuously developed in order to improve reconstruction algorithms, physics models, as well as analysis tools. Regularly, after significant changes are made, the entire real data and Monte Carlo (MC) samples are processed with a new software version and the corresponding new production identified by the subsequent numbers (e.g. production 1, 2, etc.). If it appears that the new production software has bugs, they are fixed immediately and the data is re-processed once more with the new re-spin of the latest software. This corresponds to the new re-spin of the production identified by the subsequent letters (e.g. production 6A, 6B, etc.)

The real data and Monte Carlo samples used in the analysis presented in this thesis correspond to production 6B and have been processed by the version v11r31 of the ND280 software[1]. The following software tools have been used in this analysis:

- v1r9p3 version of *nd280AnalysisTools* package[2] – a set of routines which serve to read the real data and MC input files dedicated to physics analyses.

[1] `http://www.hep.lancs.ac.uk/nd280Doc/devel/invariant/nd280Doc/workbook/Workbook.html` – T2K Intranet.

[2] `http://www.hep.lancs.ac.uk/nd280Doc/stable/invariant/nd280AnalysisTools/` – T2K Intranet.

- v0r31 version of *highland* tools[3] – a set of packages for HIGH-Level Analysis in the ND280 detector (highland). The core of the package contains basic tools and classes which facilitate the process of building event selections and data analysis. *highland* also includes several sub-packages for the official ND280 physics analyses, such as: $\nu_\mu CC$ analysis, $\nu_e CC$ analysis, etc.

- v0r27 version of *highland/numuCCAnalysis* package[4] – one of *highland* sub-packages for the $\nu_\mu CC$ analysis. It contains a set of cuts for selecting events corresponding to the inclusive $\nu_\mu CC$ reaction with the vertex in FGD1 FV. The package also allows the relevant detector systematics to be estimated.

- v2015r1p1 version of *T2KReWeight* package[5] – a unified interface for external reweighting libraries from different generators, such us GENIE or NEUT.

The first stage of the MC data production is a simulation of neutrino interactions with a target material using neutrino generators. Then, the passage of produced particles through the detector matter is simulated by a commonly used program Geant4 [35, 36]. The detector electronics response and further reconstruction is handled by proper packages of the ND280 software. The neutrino generators used in T2K are:

- The NEUT generator [37, 38] was developed to study atmospheric neutrinos and nucleon decay in the Kamiokande experiment. Then, it has been used in the Super-Kamiokande [21] and K2K [39] experiments. It has been further developed over the past years and now it is the official neutrino generator of the T2K experiment.

  The NEUT generator simulates neutrino interactions with a nucleon and nucleus in a wide range of neutrino energies from several tens of MeV to hundreds of TeV on various target materials, such as hydrogen, oxygen, carbon, argon and iron. Nucleons in a target nucleus are described using

[3] `http://www.hep.lancs.ac.uk/nd280Doc/devel/invariant/highLevelAnalysis/` – T2K Intranet.

[4] `http://www.hep.lancs.ac.uk/nd280Doc/devel/invariant/numuCCAnalysis/numuCCAnalysis.html` – T2K Intranet.

[5] `http://www.t2k.org/asg/oagroup/tool/t2kreweight` – T2K Intranet.

the RFG model by Smith and Moniz [40]. Neutrino primary interactions cross-sections are calculated using Llewellyn-Smith model [9] for CCQE interactions, Rein Sehgal model [11] for single pion production, coherent pion production mechanism by Rein-Sehgal described in [41–43], and for DIS the nucleon structure functions are taken from the parton distribution function GRV98 [44] with Bodek-Yang corrections [45]. FSI are simulated using the intranuclear cascade model. Possible meson interactions [46–52] are: elastic scattering, charge exchange, absorption and production of an additional pion. Nucleons [53, 54] can undergo elastic scattering or Δ production, which results in pion production. First, each hadron is moved by a unit length starting from the generation point. Then, based on interactions probabilities, it is determined if any of the above processes happened. If no such process takes place, the particle is moved again. This procedure is repeated until an interaction occurs or the hadron leaves the target nucleus.

- GENIE [55,56] (Generates Events for Neutrino Interaction Experiments) is designed as a universal neutrino generator developed by an international collaboration of neutrino interaction experts and is used by many experiments. In T2K it is used as a complementary neutrino generator. Its results have been compared with the NEUT predictions.

  The GENIE neutrino interaction physics model covers the neutrino energy range from several MeV to several hundreds of GeV. It is able to simulate interactions of any neutrino flavour and any type of target nucleus. The nuclear model used by GENIE is the Bodek and Ritchie RFG model with short range nucleon-nucleon correlations included [57]. The GENIE generator incorporates a large variety of possible neutrino-nucleus processes, which can happen on the entire target nucleus, individual nucleons and quarks contained in the nucleons, as well as atomic electrons. These processes are: the CCQE interactions modelled using the Llewellyn-Smith formalism [9], NCE described by Ahrens et al. in [58], baryon resonance production by the Rein-Sehgal model with the Feynmann-Kislinger-Ravndal model of baryon resonances [11, 59], coherent pion production by the Rein-Sehgal model [41, 43], non-resonance inelastic scattering by the Bodek-Yang model [60, 61], quasi-elastic charm production [62,63], DIS charm production [64–67], inclusive inverse muon

decay [68] and neutrino electron elastic scattering [69]. Similarly as it is done in the NEUT generator, the FSI interactions are simulated using the intranuclear cascade model described in [70].

- NuWro [71, 72] (Wrocław Neutrino Event Generator) is an event generator which has been developed by the Wrocław Neutrino Group [73]. It is used in T2K to test new theoretical models before they are implemented in the NEUT generator.

  NuWro can be applied to the simulation of neutrino interactions for neutrino energies from 100 MeV up to TeV. There are multiple nuclear models which can be used during the simulations: global or local FG model, hole spectral function [74–76], effective momentum and density depended potential [77]. For the CCQE and NCE interactions it is possible to choose from among various parametrisations of nuclear form factors. NuWro contains also two MEC [78] implementations: the effective transverse enhancement momentum [79] and microscopic model descibed in [80]. Apart from these interactions, NuWro takes into account resonance pion production for Δ (1232) [81–84], coherent pion production based on the Rein-Sehgal [41] and Berger-Sehgal [85] models, and DIS using the Bodek-Yang corrections [86] and PYTHIA 6 hadronization routines [87]. The FSI interactions are modelled using the intranuclear cascade model [46, 88, 89], whose more detailed description can be found in [90].

3.2 Real data sample

The T2K data taking period started in January 2010 and is divided into six runs. The analysis presented in this thesis uses the data runs 2-4 collected from November 2010 to May 2013, which correspond to the neutrino beam mode and are listed in Table 3.1. Run 1 is not used in this analysis because of the lack of BrECal in the near detector. Since run 5 predominantly the antineutrino beam mode data have been collected; small data sets for the neutrino beam mode were taken mainly for the calibration purposes.

Parameters of the neutrino beam have been changing during the data taking period. Run 2 has the beam type called "beam b", while the beam type in runs 3c and 4 is so called "beam c". "Beam c" has a shorter time between spills

(2.56 s) and a higher average proton beam power ($\sim$ 178 kW) than "beam b" (3.2 s, $\sim$ 120 kW). Horn current in runs 2, 3c and 4 had the nominal value of 250 kA. Due to technical issues, the horn current was decreased to about 205 kA in run 3b (short data taking run with "beam b" type). This run was not used in this analysis, because of a lack of MC files with a proper beam simulation.

The data sample used in this analysis is equivalent to 0.549×10^{21} POT (Protons On Target) and contains events which passed the 'good spill' data quality cut. The spill is a good quality spill when the spill flag (provided by the beam group) is 'good' and all ND280 sub-detectors and magnet data quality flags (provided by the ND280 data quality group) are 'good' [91]. In addition, this analysis does not include a small amount of data files (about 0.6% of the full statistics) that posed computing problems.

Run number	Running period	POT $\times 10^{21}$
Run 2	November 2010 - March 2011	0.0784
Run 3c	April - June 2012	0.1348
Run 4	October 2012 - May 2013	0.3387
Total	November 2010 - May 2013	0.552

Table 3.1: T2K data running periods. POT values are taken from Table 21 in [24]. The running periods are described in Section III of [23].

3.3 Monte Carlo data sets

The MC data sets corresponding to the real data sample used in the $(\nu_\mu CC\pi^0)_{incl.}$ analysis are summarised in Table 3.2.

Neutrino interactions can happen in different parts of the ND280 detector and outside this detector. In this analysis two types of Monte Carlo files are used: the so called "magnet" files with events simulated inside the entire ND280 detector volume (i.e. including the magnet) and "sand muon" files, which contain neutrino interactions simulated in the near detector hall as well as in sand surrounding this hall. The products of the "sand" interactions are mainly muons which enter ND280. Both samples were generated using version 5.3.2 of the neutrino event generator NEUT and contain all types of neutrino interactions possible at the T2K neutrino beam energies.

The number of POTs for the "magnet" MC sample is over 20 times larger than the number of POTs for the real data sample, which allows us to decrease statistical fluctuations in the simulated sample. The "sand muon" MC was generated only for run 3, as the differences between the runs for this sample are expected to be negligible. The "sand muon" sample is scaled to the "magnet" MC POT, then both MC samples are added together to obtain a minimum bias sample that is further compared with the real data.

Run number	magnet POT $\times 10^{21}$	sand muons POT $\times 10^{21}$
Run2	2.13	–
Run3	3.08	1.19
Run4	7.00	–
Total	12.21	1.19

Table 3.2: Number of POTs for MC data sets used in the analysis.

Similarly to the ND280 software, the neutrino flux model has been continuously improved. In order to use the latest neutrino flux without repeating the MC generation and reconstruction procedure, the studied neutrino interactions are reweighted on an event-by-event basis. The weights from the following reweighting files were used in the presented analysis:

- *tuned13av1.1/runX/nd5_tuned13av1.1_13anom_runX_fine.root*[6],

where X in *runX* corresponds to the run number: 2, 3c or 4.

[6] `www.t2k.org/beam/NuFlux/FluxRelease/13arelease/13aFlux_updated` – T2K Intranet.

Chapter 4

Selection criteria

The selection of $(\nu_\mu CC\pi^0)_{incl.}$ events is performed in four steps.

First, within the pre-selection, spill quality cuts are applied only to the real data and the spill is divided into bunches. This is the only part where the conditions for real data and for MC data sets differ from each other. The next steps are identical for both samples.

Then, the negative muon-like track starting in the FGD1 FV is chosen by applying the official $\nu_\mu CC$ cuts.

After that, the photons from π^0 decay are selected. The selection criteria depend on the type of the object produced by the photons: electromagnetic cascade, e^+e^- pair or single $e^\pm$ track. Possible π^0 decay products topologies are listed in Table 4.1

In the end, the observed reaction is considered as the $(\nu_\mu CC\pi^0)_{incl.}$ reaction, if a muon track and at least two π^0 decay products (showers and/or $e^\pm$ tracks) are found.

4.1 Pre-selection

The following pre-selection conditions have to be satisfied before the actual selection starts:

- Spill quality cut applied only to the real data – the spill flag (provided by the beam group) is 'good' and all ND280 subdetectors and magnet data quality flags (provided by the ND280 data quality group) are 'good' [91].

- Bunching – the spill is divided into 8 bunches (Sec. 2.1) according to

π^0 decay products combinations	first photon from π^0 decay	second photon from π^0 decay
no π^0	none	none
1 shower	ECal shower	none
1 $e^{\pm}$ in TPC	e^+ or e^- track	none
2 showers	ECal shower	ECal shower
2 $e^{\pm}$ in TPC	e^+ or e^- track	e^+ or e^- track
2 $e^{\pm}$ in TPC	e^+e^- pair	none
1 shower and 1 $e^{\pm}$	ECal shower	e^+ or e^- track
more than 2 π^0 decay products	ECal shower	e^+e^- pair
more than 2 π^0 decay products	e^+e^- pair	e^+ or e^- track
more than 2 π^0 decay products	e^+e^- pair	e^+e^- pair

Table 4.1: Definition of π^0 decay products topologies used in the analysis. The abbreviations listed in the first column are further used in the plot legends and table descriptions. In short, category "more than 2 π^0 decay products" is also denoted as "$\geq 3\pi^0$ dec. prod.".

the beam structure. All the objects reconstructed within a bunch time window are treated as belonging to one event. Bunching is handled by the *highland* framework.

4.2 Particle identification in the TPC and ECal

Particle identification is crucial for both the muon and π^0 selection, thus it will be introduced prior to the description of the selection criteria.

The selection of charged particles is based mainly on the particle identification it the TPC. Further information, especially important for neutral particles, is provided by the calorimeter.

4.2.1 Particle identification in the TPC

In the TPC a measured energy deposit per unit distance (dE/dx) is compared with a theoretical prediction using the following variable [92, 93]:

$$Pull_\alpha = \frac{dE/dx_{meas} - dE/dx_\alpha}{\sigma_\alpha}, \tag{4.1}$$

where

- $\alpha = e, \mu, \pi^{\pm}, K^{\pm}, p$ corresponds to five different particle hypotheses,
- dE/dx_{meas} is a measured dE/dx,
- dE/dx_{α} is a theoretical prediction of dE/dx for the particle hypothesis α assuming the reconstructed momentum of corresponding track,
- σ_{α} is a standard deviation of the dE/dx_{α} distribution.

Figure 4.1 shows that this is an efficient method of particle identification, except for the momenta regions where the expected dE/dx values for different particles are similar.

Using the Pull variable one can construct the likelihoods for each particle [94]:

$$L_{\alpha} = \frac{\prod_{i=TPC1}^{TPC3} \exp(Pull_{i,\alpha}^2/2)}{\sum_{\alpha=\mu,e,p,\pi} \prod_{i=TPC1}^{TPC3} \exp(Pull_{i,\alpha}^2/2)}, \tag{4.2}$$

with $L_{\mu} + L_e + L_p + L_{\pi} = 1$.

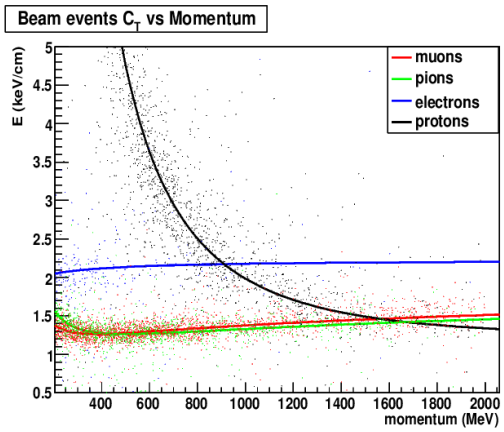

Figure 4.1: Energy loss in gas for different particles as a function of the particle momentum measured in the TPC of the ND280 detector [92].

4.2.2 Particle identification in the ECal

Particle identification in the ECal relies on a MIP EM (Minimum Ionising Particle Electro-Magnetic shower) discriminator [93,95,96], which aims at distinguishing the showering particles, such as electrons and photons, from the non-showering particles, such as muons. The MIP EM discriminator is calculated using low level variables based on the deposited charge distribution

and the shape of the reconstructed object. Figure 4.2 depicts the MIP EM distribution for the pure sample of through-going muons and the pure sample of electrons producted in γ conversion in DsECal. ECal information can be also used to differentiate between muons and charged pions, which are indistinguishable through their dE/dx values in the TPC detectors because of similar masses.

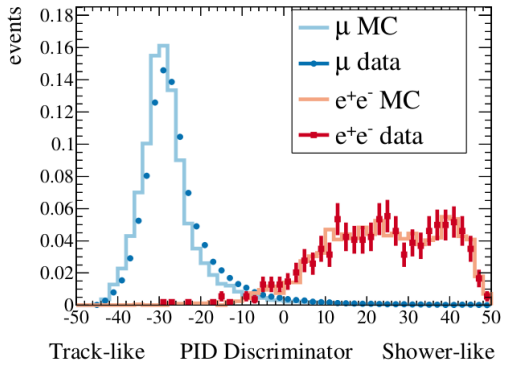

Figure 4.2: Distribution of the MIP EM discriminator for electrons and muons in the DsECal [95].

4.3 $\nu_\mu CC$ inclusive selection

The $(\nu_\mu CC\pi^0)_{incl.}$ analysis starts with the selection of negative muon produced in the inclusive $\nu_\mu CC$ sample with vertex inside the FGD1 Fiducial Volume (FV). Figure 4.3 and Table 4.2 contain the definition of the FGD1 FV. Neutrino interactions with the vertex outside the FGD1 Fiducial Volume are denoted as "out of FGD1 FV" background, regardless of the reaction type and neutrino flavour. This part of the selection is identical for all π^0 decay product topologies.

The official $\nu_\mu CC$ cuts [34,94,97] in the *highland/numuCCAnalysis* package are as follows:

1. Observation of at least one track in the TPC – this is required because currently only TPC provides reliable momentum measurement and particle identification,

2. Selection of the Highest Momentum Negative track (HMN track) starting in the FGD1 FV with more than 18 nodes in the TPC segment closest

	FGD1 Volume		FGD2 Volume	
	min	max	min	max
X	-932.17	932.17	-932.17	932.17
Y	-877.17	987.17	-877.17	987.17
Z	115.95	446.955	1473.95	1807.05

	FGD1 Fiducial Volume FV	
	min	max
X	-874.51	874.51
Y	-819.51	929.51
Z	136.875	446.955

	FGD1 Extended Volume		FGD2 Extended Volume	
	min	max	min	max
X	-1000.0	1000.0	-1000.0	1000.0
Y	-1150.0	1150.0	-1150.0	1150.0
Z	100.0	620.0	1400.0	2000.0

Table 4.2: Definition of the FGD volume, FGD1 Fiducial Volume (FV) and FGD extended volume consisting of the FGD volume and TPC outer envelope. Schematic view is shown in Figure 4.3.

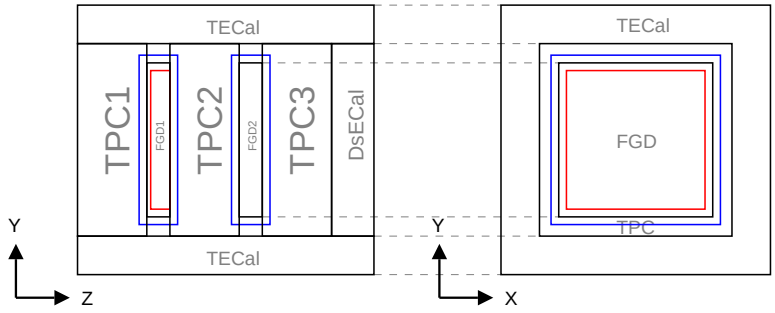

Figure 4.3: Schematic view of the ND280 tracker and surrounding calorimeter in the ZY plane on the left and XY plane on the right. A red box shows the position of the FGD1 Fiducial Volume (FGD1 FV). Blue boxes show the position of the FGD extended volume. FGD volumes, FGD1 FV and FGD extended volume are defined in Table 4.2. Black boxes in the right plot denote external dimensions of the detectors: FGD (the smallest one), TPC (the medium one), TECal (the biggest one).

to the track start position; the track has to be long enough to get correct momentum, charge and *Pull* values,

3. TPC veto – rejection of events with a broken muon track starting upstream to the FGD1,

4. External FGD1 veto – rejection of events with a broken muon track starting in the FGD1, but outside its FV,

5. Muon-like HMN track cut, i.e. $L_\mu > 0.05$ and, for tracks with momenta smaller than 500 MeV, $(L_\mu + L_\pi)/(L_\mu + L_\pi + L_e) > 0.8$.

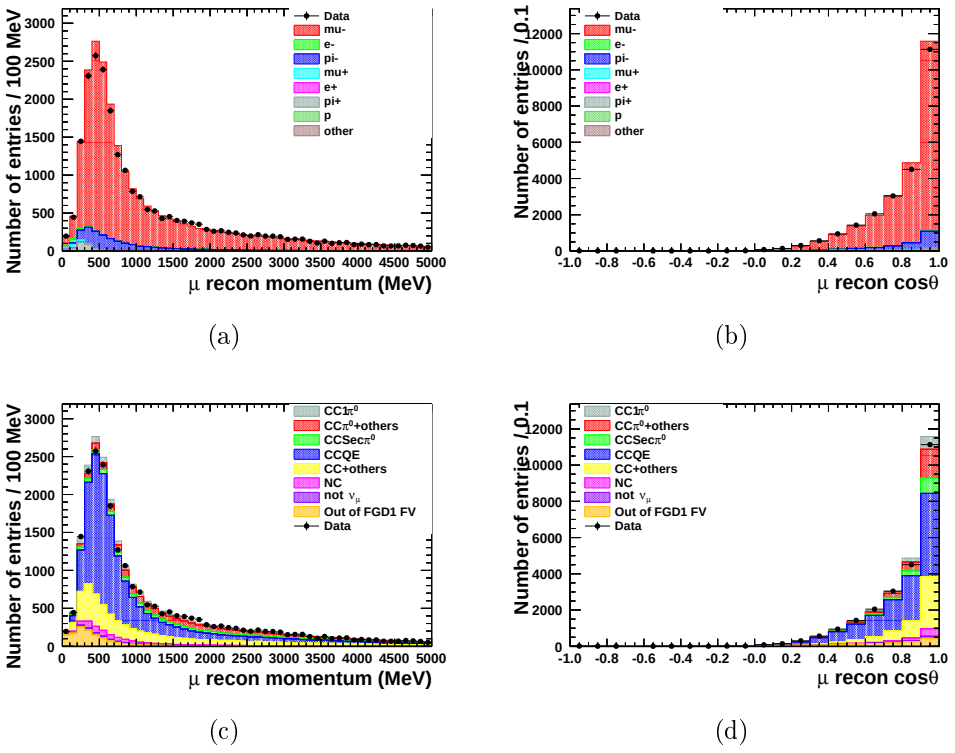

(a) (b)

(c) (d)

Figure 4.4: Characteristics of the selected muon candidates after the $\nu_\mu CC$ cuts. The MC distributions are scaled to real data POT given in Table 3.1. The left column plots show the reconstructed momentum and the right column ones – the reconstructed $\cos\theta$. In the upper row one can find the distributions with Monte Carlo split according to the true particle type of the selected muon candidate. The bottom row contains the plots with Monte Carlo split according to the neutrino reaction type (see Table 1.1).

The reconstructed momentum and $\cos\theta$ distributions of the muon candidate after the $\nu_\mu CC$ cuts are shown in Figure 4.4. Angle θ is an angle between

the track direction and the Z axis. 90% of the selected tracks are true muons, the subsequent biggest contributions come from negative (7.2%) and positive (1.3%) pions. The momentum distribution is equivalent to the top left plot in Figure 6 in [94], which presents the muon candidate momentum after (inclusive) $\nu_\mu CC$ selection, but divided into different categories.

Real data sample			
	Number of events		
all selected events	24242		
MC sample scaled to real data POT			
	Number of events	purity	efficiency
all selected events	24847		
$\nu_\mu CC$ events	22350	90%	53%
$\nu_\mu CC1\pi^0$ events	1243	5%	52%
$\nu_\mu CC\pi^0 + others$ events	2564	10%	68%
Total $(\nu_\mu CC\pi^0)_{incl.}$ events	3807	15%	62%

Table 4.3: Number of events, purity and efficiency after the $\nu_\mu CC$ cuts. $\nu_\mu CC1\pi^0$ and $\nu_\mu CC\pi^0 + others$ add up to $(\nu_\mu CC\pi^0)_{incl.}$.

The results at this level of the selection are listed in Table 4.3. The selected sample contains 90% of $\nu_\mu CC$ events with the vertex in the FGD1 FV. Among them, there are 5% of $\nu_\mu CC1\pi^0$ events and 10% of $\nu_\mu CC\pi^0 + others$ events. After $\nu_\mu CC$ cuts, the efficiencies for selecting the $\nu_\mu CC$ and $(\nu_\mu CC\pi^0)_{incl.}$ reactions equal 53% and 62%, respectively.

4.4 π^0 selection

The second stage of the $(\nu_\mu CC\pi^0)_{incl.}$ selection concerns the selection of π^0 decay products. The π^0 selection criteria have been entirely elaborated by the author of this thesis. A Monte Carlo truth study was conducted and the π^0 selection criteria have been chosen based on the result of this study.

4.4.1 π^0 Monte Carlo truth studies

This section describes the characteristics of true π^0 mesons from the $(\nu_\mu CC\pi^0)_{incl.}$ reaction. Those mesons have been selected using the MC truth information,

i.e. the properties of events and particles simulated by the MC generator, independently of the simulation of particle interactions with the detector material and the reconstruction software.

Figure 4.5 shows the true multiplicity of π^0's, their momentum and $\cos\theta$ distributions for signal reactions, before the selection cuts. About 80% of the signal events contain only one π^0, in 15% of events there are two π^0's and in 5% more than two π^0's appear. The momentum distribution seems to include two components: a narrow peak below 200 MeV and a broader part with a maximum near 350 MeV and higher-energy tail[1].

The π^0 meson itself is invisible in the detector, because its mean life time is $\tau = 8 \cdot 10^{-17}$ s ($c\tau = 25.1$ nm). In 98.8% of cases it decays into two photons and in 1.2% – into $e^+e^-\gamma$. Other decay modes constitute about 0.004%, so they can be neglected. Since the neutral pion decays immediately and predominantly into two photons, the selection strategy depends on the photon energies and location of the point of the photon conversion or the Compton scattering. In the case of the conversion, in a nuclear field the photon disappears and an electron-positron pair is produced. In the Compton scattering, the photon hits an electron bound in an atom and transfers part of its energy to the electron, which recoils. For a better understanding, in the following the number and characteristics of the photons and electrons involved in the Compton scattering will be studied.

The MC sample includes the information about the particles produced by the photon, but not about the type of interaction it underwent. Therefore, an approximate method, based on the distance between the photon stopping point and the electron starting point, is used to distinguish the Compton scattering from the photon conversion. For the conversion, in the case of the primary e^+e^- pairs in electromagnetic cascades, this distance should be equal to zero (Fig. 4.6(a)). However, it is possible that the first particles in the cascade are not saved by the algorithm simulating the passage of the particles through the detector (Fig. 4.6(b)). This can happen for short particle trajectories in inactive material, for which the reconstruction is impossible. The starting point of such $e^\pm$ trajectory is usually downstream to the photon stopping point. The photons undergoing the Compton scattering can travel a longer distance before they stop (Figures 4.6(c) and (d)). The electrons' starting point can be

[1]It was cross-checked that this double structure did not appear in the Monte Carlo sample generated using GENIE, so it is a feature of the NEUT MC.

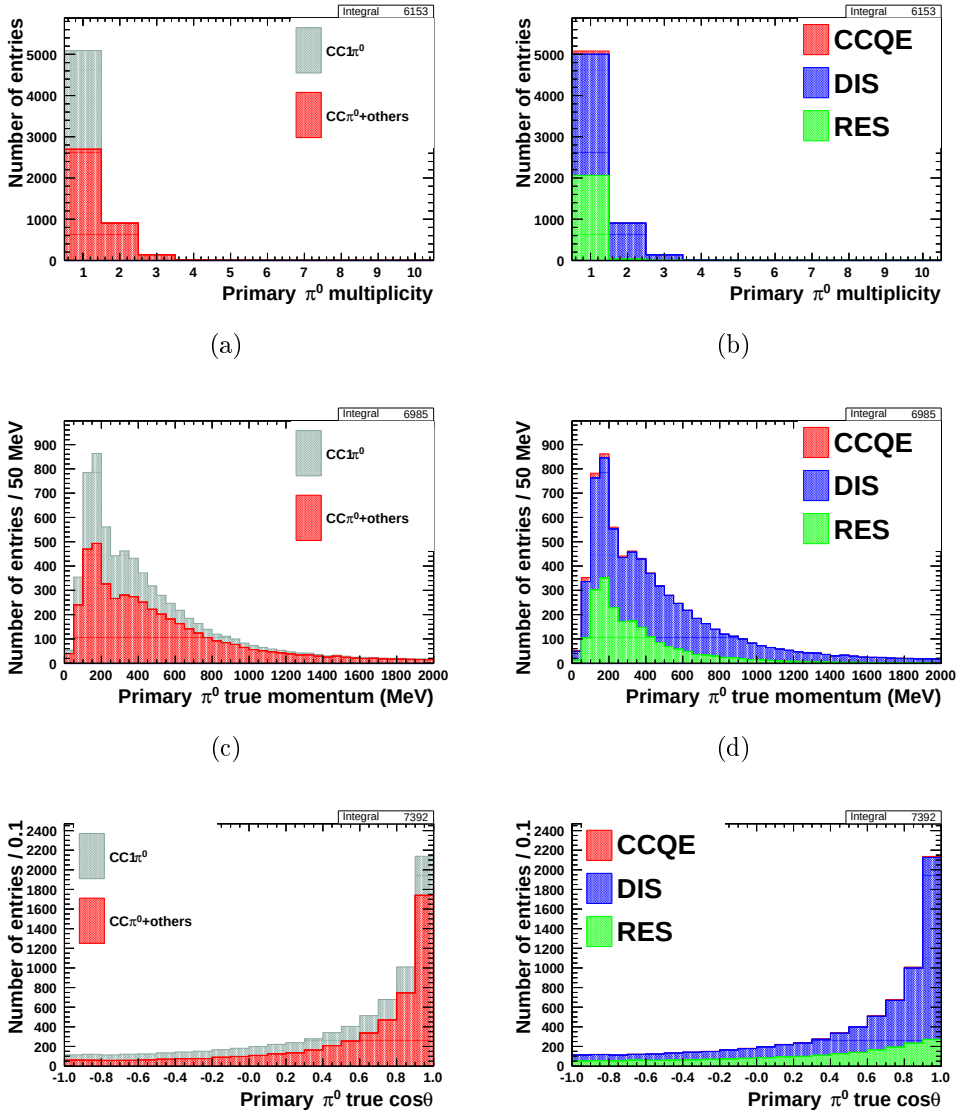

Figure 4.5: Properties of the primary π^0's from the $(\nu_\mu CC\pi^0)_{incl.}$ reaction with the neutrino interaction vertex in FGD1 FV. All distributions are for MC data sets and are scaled to real data POT given in Table 3.1. The upper row plots show the multiplicity of neutral pions, the middle row plots – their true momenta, and the bottom row ones – their true $\cos\theta$ values. In the left column one can find the distributions split according to the neutrino reaction type after FSI (Table 1.1). The right column contains plots with distributions split according to the neutrino reaction type before FSI.

located downstream or upstream to the photon stopping point, depending on the scattering angle α. The direction of the scattered photon is determined as parallel to the vector that starts in the $e^{\pm}$ starting point and goes through the photon stopping point. Therefore, for the cascades the calculated scattering angle is usually close to 180°. Let us assume that the majority of the electrons with the starting point at non-zero distance from the photon stopping point are recoiled in the Compton scattering, but we have to remember that some of them belong to the cascades as discussed above. The other electrons and all positrons are then assumed to be produced in the photon conversion process.

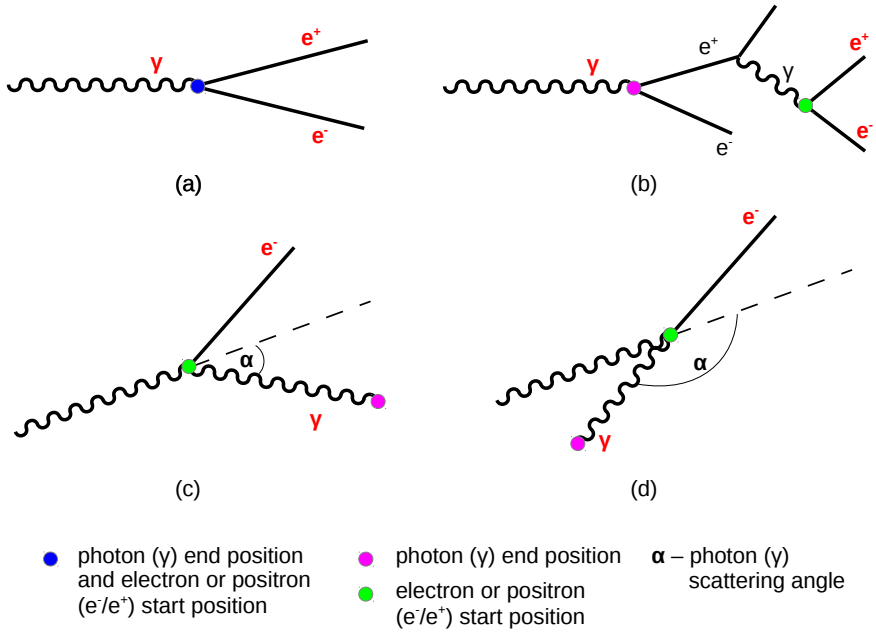

Figure 4.6: Relationship between the photon stopping point and the registered $e^{\pm}$ starting point for different photon interactions. Relevant particle γ and $e^{\pm}$ trajectories are marked with red letters. Plot (a) shows standard photon conversion. Plot (b) depicts the photon conversion in which the first particles in the cascade were not saved by the MC programme. Plots (c) and (d) present the Compton scattering at different angles.

The fraction of the electrons starting at non-zero distance from the photon stopping point is 7%. The fraction for positrons equals 0.8%. Figure 4.7 depicts the distribution of the studied distance for electrons. A peak at around 1300 mm comes from photons scattered in FGD, traversing TPC, and stopping in another dense subdetector: P0D, DsECal or the second FGD. Figure 4.8

shows an analogical distribution for positrons. Such positrons usually start in TECal, downstream to the photon stopping points, which stop mainly in inactive material or TECal (Fig. 4.9). This indicates that these positrons are part of the cascades in the ECal.

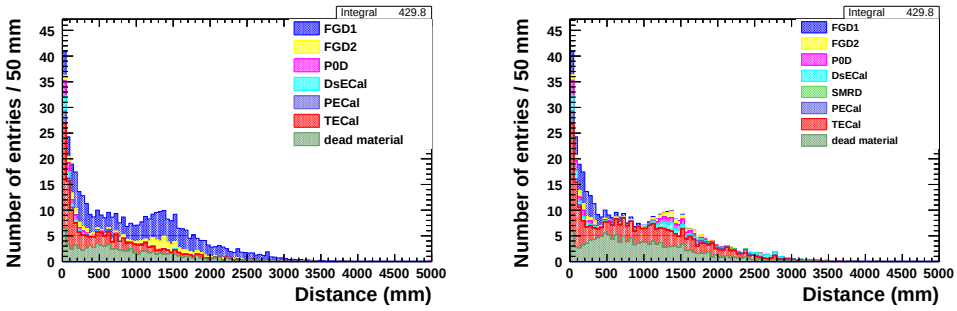

(a) (b)

Figure 4.7: Distance between the photon end position and the electron start position for electrons starting at non-zero distance from the photon end position. The distribution is scaled to real data POT given in Table 3.1. The left distribution is split according to the detector in which the recoiled electron starts. The right one is split according to the detector in which the photon stops.

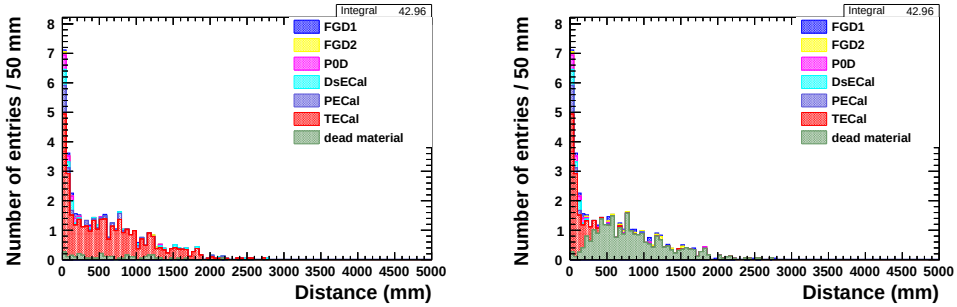

(a) (b)

Figure 4.8: Distance between the photon end position and the positron start position for positrons starting at non-zero distance from photon end position. The distribution is scaled to real data POT given in Table 3.1. The left distribution is split according to the detector in which the positron starts. The right one is split according to the detector in which the photon stops.

Figure 4.10 shows the relationship between the photon scattering angle and the fraction of the photon momentum transferred to the $e^{\pm}$, depending on the process in which the $e^{\pm}$ originates. As it was expected, the electrons from the

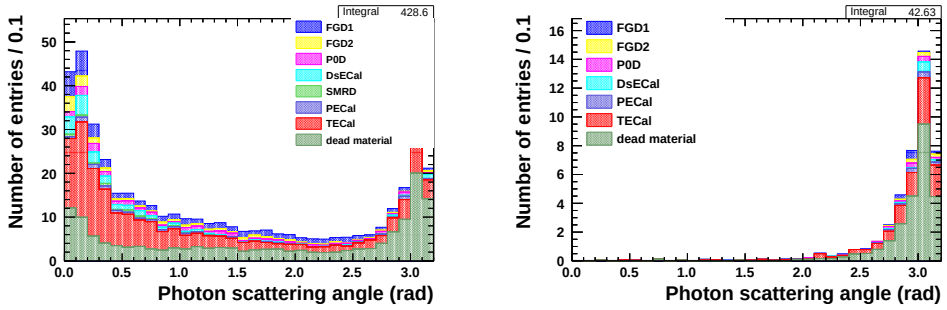

(a) (b)

Figure 4.9: Photon scattering angle (the angle between the original photon direction and the vector joining the $e^{\pm}$ start position and photon stopping point) for the electrons (plot (a)) and positrons (plot (b)) starting at non-zero distance from the photon end position. The distributions are scaled to real data POT given in Table 3.1. The distributions are split according to the detector in which the photon stops.

Compton scattering placed above the magenta line on the plot 4.10(a) inherit the larger part of the photon momentum, the larger photon scattering angle is. The electrons and positrons that are part of the electromagnetic cascade usually share a small part of the photon energy. They start downstream to the photon stopping point, so the scattering angle assigned to them is close to 180°, and therefore they mostly populate the right bottom corner in both plots 4.10. There are more electrons than positrons below the magenta line, which could be assigned to a difference between the interactions with the matter of both types of the particles.

Figure 4.11 shows the distribution of the photon momentum fraction inherited by the $e^{\pm}$. In the conversion, the photon energy is shared by two particles. Thus, the intermediate energy fraction is favoured. The electrons starting at non-zero distance from the photon stopping point tend to capture a very small part or almost whole photons energy. The electrons from the Compton scattering are marked with the magenta line on plot 4.11(b). The peak around zero comes from the electrons being a part of the cascade.

The photon reconstruction procedure is the same for the conversion and Compton scattering processes. An electron recoiled in the Compton scattering is indistinguishable from an electron from $e + e-$ pair, where a positron was not reconstructed.

The criteria of the π^0 decay products' selection depend on the type of reconstructed object associated with the photons or $e^{\pm}$ from their conversion

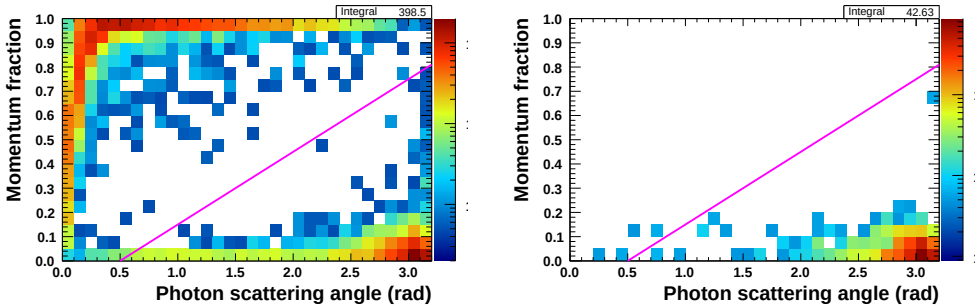

(a) (b)

Figure 4.10: Relationship between the fraction of the photon momentum transferred to the electron (a) or positron (b) and the photon scattering angle for $e^{\pm}$ starting at non-zero distance from the photon stopping point. The distributions are scaled to real data POT given in Table 3.1.

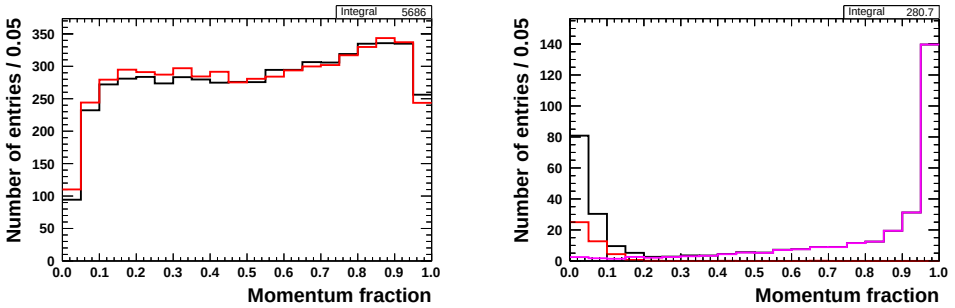

(a) (b)

Figure 4.11: Fraction of the photon momentum transferred to the electron (black) or positron (red) for (a) $e^{\pm}$ starting immediately in the photon stopping point and (b) $e^{\pm}$ starting at non-zero distance. The magenta line on plot (b) shows the distribution for the subsample of the electrons that are above the magenta line on plot 4.10(a). The distributions are scaled to real data POT given in Table 3.1.

or scattering. The types of the considered reconstructed objects are listed in Table 4.4. They are ranked with respect to their quality, i.e. ease of identification. Therefore, if more than one type of the object was reconstructed for a single photon, the object type with a lower number (higher quality) is chosen.

no.	Abbreviation	Reconstructed object associated with the π^0 decay products
0	none	Neither photon nor any of its products give a signal in the detector
1	TPC	Reconstructed track with a part in the TPC
2	isoDsECal	Isolated object in DsECal
3	isoBrECal	Isolated object in BrECal
4	isoFGD1	Isolated object in FGD1
5	isoFGD2	Isolated object in FGD2
6	FGD-ECal -(SMRD)	Reconstructed track with a part in the FGD, TECal and alternatively in SMRD
7	ECal-SMRD	Reconstructed track with at least two segments in TECal, DsECal and/or SMRD
8	other	Reconstructed object in other subdetectors

Table 4.4: Definitions of the types of reconstructed objects associated with the π^0 decay products, i.e. photons or $e^{\pm}$ tracks or pairs from photon conversion or scattering. The abbreviations listed in the second column are further used in the plot legends.

Figure 4.12 presents the momentum distributions of photons from π^0 decays with the information about the reconstructed object. Almost all Higher-Energy photons (HE photons, photons from π^0 decay with higher energy) have momenta above 100 MeV (the majority of photons below 100 MeV are not reconstructed), which can reach even 1 GeV (Fig. 4.12(a)). Nevertheless, 32% of HE photons are not reconstructed in any subdetector. Lower-Energy photons (LE photons, photons from π^0 decay with lower energy) have much lower momenta, usually below 400 MeV (Fig. 4.12(b)), and 50% of them do not produce a signal in the detector. The photons' opening angle is depicted in Fig. 4.13 and has two-component structure, resulting from the π^0 momentum double structure (see Fig. 4.5(c),(d)).

Figure 4.14 shows the reconstructed objects associated with HE and LE photons or $e^{\pm}$ tracks or pairs from photon conversion or other interactions,

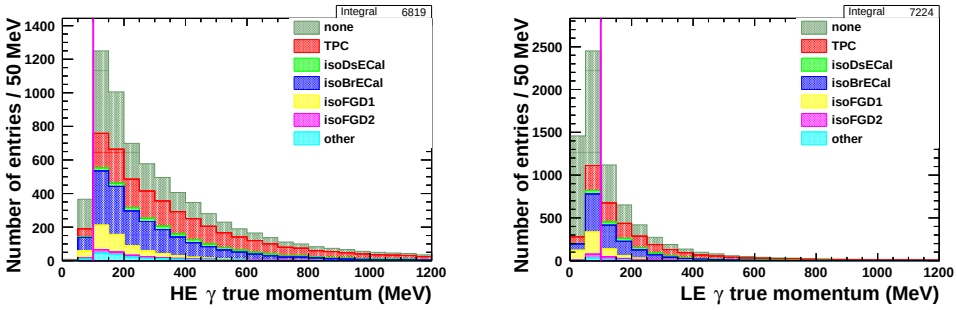

(a) (b)

Figure 4.12: True momenta of photons from the decays of the primary π^0 from the $(\nu_\mu CC\pi^0)_{incl.}$ reaction with the neutrino interaction vertex in FGD1 FV. Distribution (a) corresponds to the higher energy photon, and distribution (b) – to the lower energy photon. They are split according to the type of the reconstructed object associated with the photon, defined in Table 4.4 and scaled to real data POT given in Table 3.1.

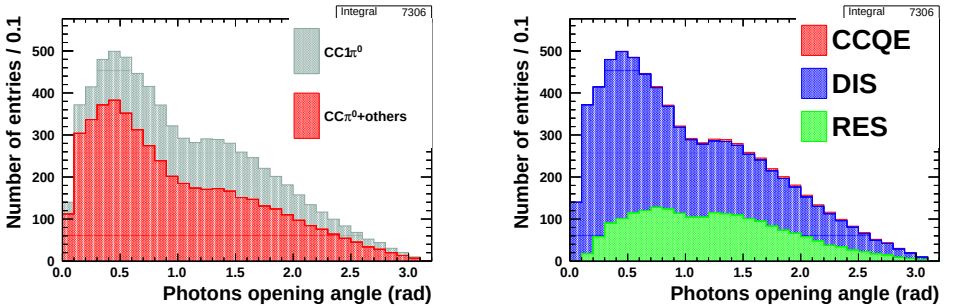

(a) (b)

Figure 4.13: True opening angle of photons from the decay of the primary π^0 from the $(\nu_\mu CC\pi^0)_{incl.}$ reaction with the neutrino interaction vertex in FGD1 FV. The distributions are scaled to real data POT given in Table 3.1. In plot (a) one can find the distributions split according to the neutrino reaction type after FSI (Table 1.1). Plot (b) is split according to the neutrino reaction type before FSI.

dominated by the Compton scattering. For 16% of neutral pions neither of the photons produces a signal in the detector. For 50% of neutral pions one photon is lost, in 34% it is a LE photon and in 16% it is a HE photon. The selection described in this note is focused on the topology with photons reconstructed as isolated objects in the ECal (isoDsECal or isoBrECal) or $e^{\pm}$ tracks or pairs of tracks in the TPC. These topologies are framed with a black line on the plot. For 24% of π^0's both photons, and for 49% one photon is reconstructed as such an object. Only such events are analysed using the selection described in this thesis. By adding the isolated FGD objects to the selection, the fraction of π^0's in which both photons could be reconstructed could increase by about 8%. The $(\nu_\mu CC\pi^0)_{incl.}$ analysis can be extended by such an object in the future, when the quality of particle identification in FGD is improved and better tested. By adding all the other reconstructed objects one can gain another 2% of such events.

Figure 4.15 depicts the dependence between the type of reconstructed object and the subdetector, in which the photon underwent the conversion or the Compton scattering. As expected, most of those processes occur in dense materials. For the π^0 decay products reconstructed in the TPC, they occur mainly in FGDs. Isolated ECal objects, as expected, originate from photons converting or scattered inside the ECal.

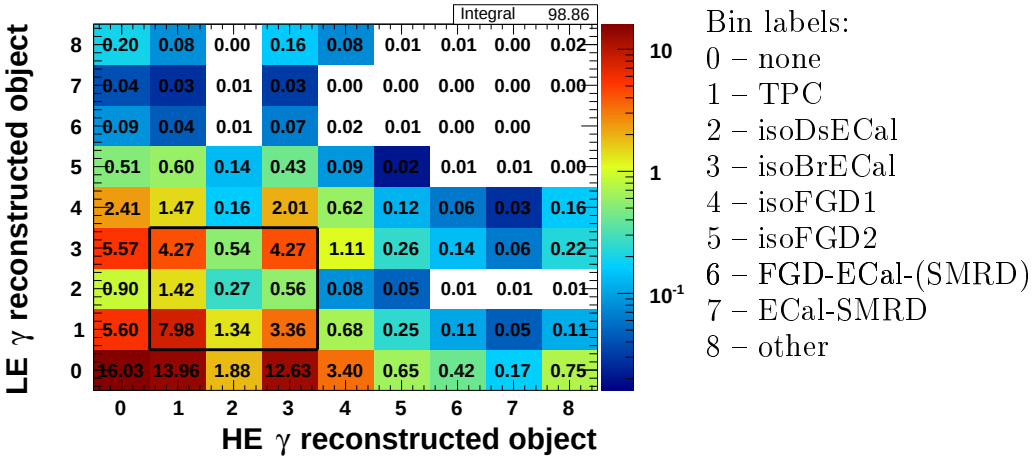

Figure 4.14: Percentage of the types of reconstructed objects associated with the photons from the decay of the primary π^0 from the $(\nu_\mu CC\pi^0)_{incl.}$ reaction with the neutrino interaction vertex in FGD1 FV. Bin numbers corresponding to the types of objects are enumerated in the bin labels list on the right side and described in Table 4.4. The X axis corresponds to the higher energy photon, and the Y axis – to the lower energy photon.

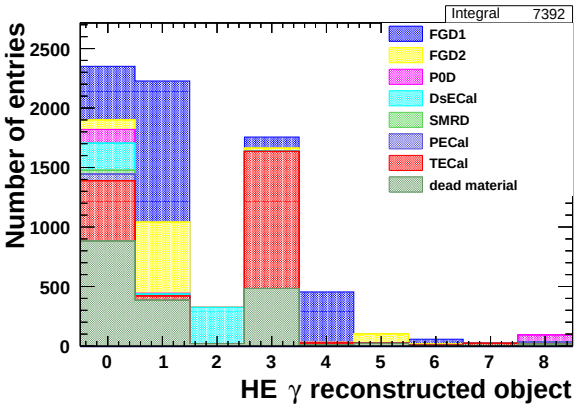

(a)

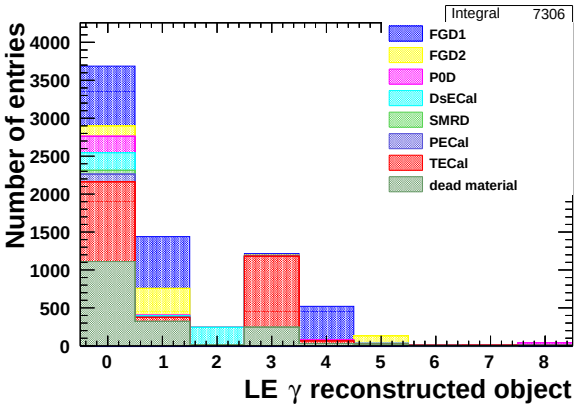

(b)

Bin labels:
0 – none
1 – TPC
2 – isoDsECal
3 – isoBrECal
4 – isoFGD1
5 – isoFGD2
6 – FGD-ECal-(SMRD)
7 – ECal-SMRD
8 – other

Figure 4.15: Type of reconstructed objects associated with the photons from the decay of the primary π^0 from the $(\nu_\mu CC\pi^0)_{incl.}$ reaction with the neutrino interaction vertex in FGD1 FV. Bin numbers corresponding to the types of objects are enumerated in the list on the right side and described in Table 4.4. The distributions are split according to the subdetector in which the photon conversion or the Compton scattering occurred and scaled to real data POT given in Table 3.1. Plot (a) corresponds to the higher energy photon, and plot (b) – to the lower energy photon.

4.4.2 π^0 decay product selection using post-reconstruction variables

In an ideal situation the signature of the photon from a π^0 decay would be a shower in the calorimeter or an electron-positron pair in the TPC. However, as it was shown in the previous section, some of the photons do not produce any signal in the detector because of their low energies, and some of the electrons and positrons from e^+e^- pairs are not visible in the TPC. Therefore, in this analysis only one component of the e^+e^- pair is required to confirm the photon conversion in the FGD extended volume (composed of the FGD volume and TPC outer envelope, defined in Table 4.2 and depicted in Fig. 4.3). In addition to the muon candidate, at least two reconstructed π^0 decay products are requested, and their possible combinations are listed in Table 4.1. The photons might originate from different π^0's as the products of π^0 decays are not paired.

Further in this section the selection procedure of the electron and positron candidates in the TPC and photon candidates in the ECal will be described. The cuts are applied in a loop on all tracks with the segment in the TPC, except the muon candidate, and on all isolated ECal objects in the events which passed $\nu_\mu CC$ selection cuts.

Each plot in the following subsections is made after applying $\nu_\mu CC$ selection cuts. Additional cuts are described in the figure captions. Efficiencies and purities are calculated for the selected tracks, not for the whole events. In other words, the efficiency is calculated with respect to the number of all $e^\pm$'s tracks with the segment in the TPC (except the muon candidate) or the number of isolated objects from primary π^0 decays, registered in the ECal; in both cases for the sample of events that passed $\nu_\mu CC$ cuts.

4.4.2.1 $e^\pm$ candidates in the TPC

To select e^+ or e^- ($e^\pm$) tracks in the TPC the following steps were applied:

1. All TPC tracks, except the muon candidate track, were considered.
2. Tracks with more than 18 nodes in the TPC segment closest to the track start position were accepted in order to choose good quality tracks.
3. The track start position had to be located in the FGD extended volume. Replacing the FGD1 FV with the FGD extended volume was justified by

the fact that the electrons and positrons from the π^0 decay are the secondary particles usually produced at a certain distance from the neutrino vertex.

This cut is intended to reject particles entering the TPC from the ECal, P0D and inactive, adjacent material. Figure 4.16 shows that, as expected, most of the particles passing this cut truly start in the FGD volume and in the inactive (dead) material between FGD and TPC.

4. $Pull_e \in (-2, 2.5)$ was required to choose electron-like tracks.

   Figure 4.17 depicts the $Pull_e$ distribution for the TPC tracks reconstructed as (a) negative – electron candidates, and (b) positive – positron candidates. This is a very efficient cut, which rejects most of the charged pions and part of the protons. In the distribution a significant real data excess is visible, which contributes to the surplus of $e^{\pm}$ candidates further discussed in Sec. 4.5.

5. For positron candidates (TPC tracks with a positive reconstructed charge) the momentum smaller than 800 MeV was required. This cut is intended to reject protons.

6. The track momentum larger than 50 MeV was required to reject δ rays and track curving back, which are often incorrectly reconstructed, e.g. as two separate tracks.

   Figure 4.18 depicts the momentum distribution of the $e^{\pm}$ candidates before the last two, 5 and 6 momentum cuts. Most of the tracks below 50 MeV are electrons and positrons, but they are rejected for the above reasons. Figure 4.18(b) shows that, in fact, the positive particles above 800 MeV are mainly protons.

The efficiency, purity and reduction of the number of $e^{\pm}$ candidates after each cut are given in Table 4.5. It is assumed that after the first cut, i.e. the selection of all tracks with the segment in TPC (except the muon candidate), the efficiency equals 100%. The reaction and particle composition of the selected sample chosen after all cuts is presented in Table 4.6. Category "coincidental particle" denotes particles of any type originating from a different neutrino reaction than the muon candidate. The sample contains 84.2% of $e^{\pm}$; among them 44.6% are decay products of the primary π^0 produced in

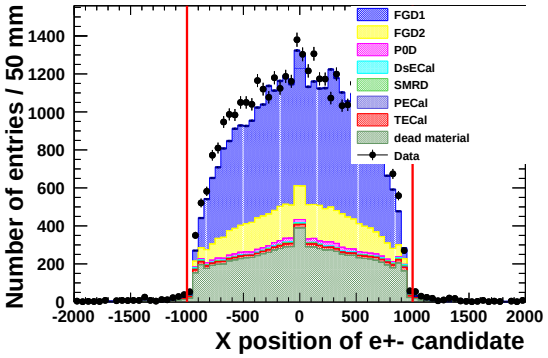

(a)

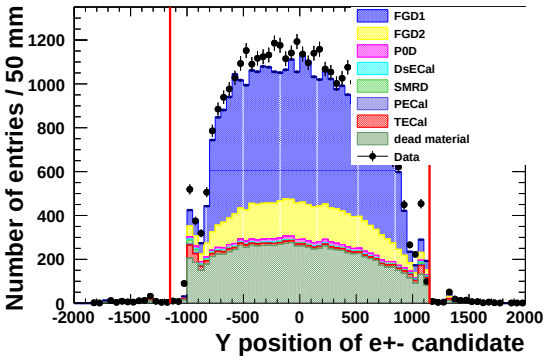

(b)

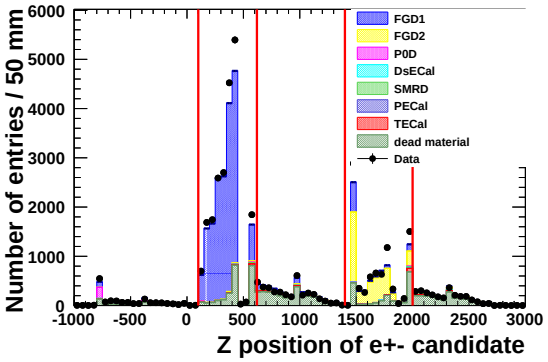

(c)

Figure 4.16: Reconstructed start position of the selected $e^{\pm}$ candidates in the TPC after the $\nu_{\mu}CC$ cuts described in Sec. 4.3 and after 1-2 $e^{\pm}$ cuts. Plot (a) shows X coordinate, plot (b) – Y coordinate, and plot (c) – Z coordinate. The Monte Carlo distributions are split according to a subdetector containing the true beginning of the track and scaled to real data POT given in Table 3.1. The red lines on the plots show the values of cut 3.

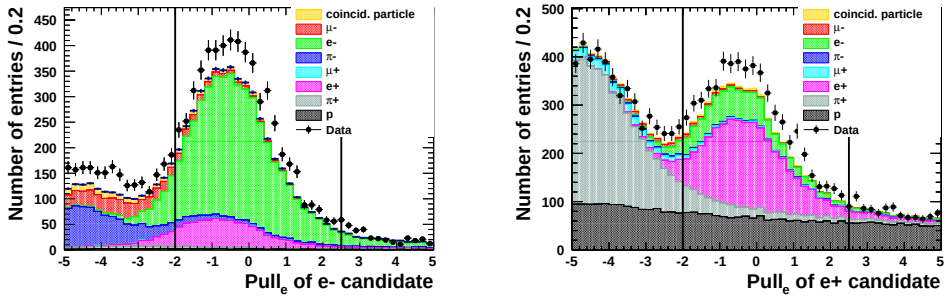

(a) (b)

Figure 4.17: Reconstructed $Pull_e$ distributions of the selected $e^{\pm}$ candidates in the TPC after $\nu_\mu CC$ cuts (Sec. 4.3) and after 1-3 $e^{\pm}$ cuts. Plot (a) corresponds to the negative TPC tracks and plot (b) – to the positive TPC tracks. The Monte Carlo distributions are split according to the true particle type of the selected $e^{\pm}$ candidate and scaled to real data POT given in Table 3.1. The black lines on the plots show the values of cut 4.

the $(\nu_\mu CC\pi^0)_{incl.}$ reaction and another 7.9% originate from the signal reaction, but not from the primary π^0 decays. The remaining 31.7% true $e^{\pm}$'s come from the photon conversion or scattering not originating from the signal reaction (25.4%), and from muon decays (4.2%) and other sources (2.1%) like scattering and decays of other particles and ν_e interactions. The efficiency of the selection of true $e^{\pm}$ from the primary π^0 decay from the $(\nu_\mu CC\pi^0)_{incl.}$ reaction inside FGD1 FV that produced a track containing the TPC segment is 41%. Particles other than $e^{\pm}$ (15.8%) are mainly charged pions (9.8%), μ^- (2.6%) and protons (2.3%), and among them 4.5% originate from the signal reaction. So, the overall purity of selecting particles from the $(\nu_\mu CC\pi^0)_{incl.}$ reaction inside FGD1 FV is 57.0%.

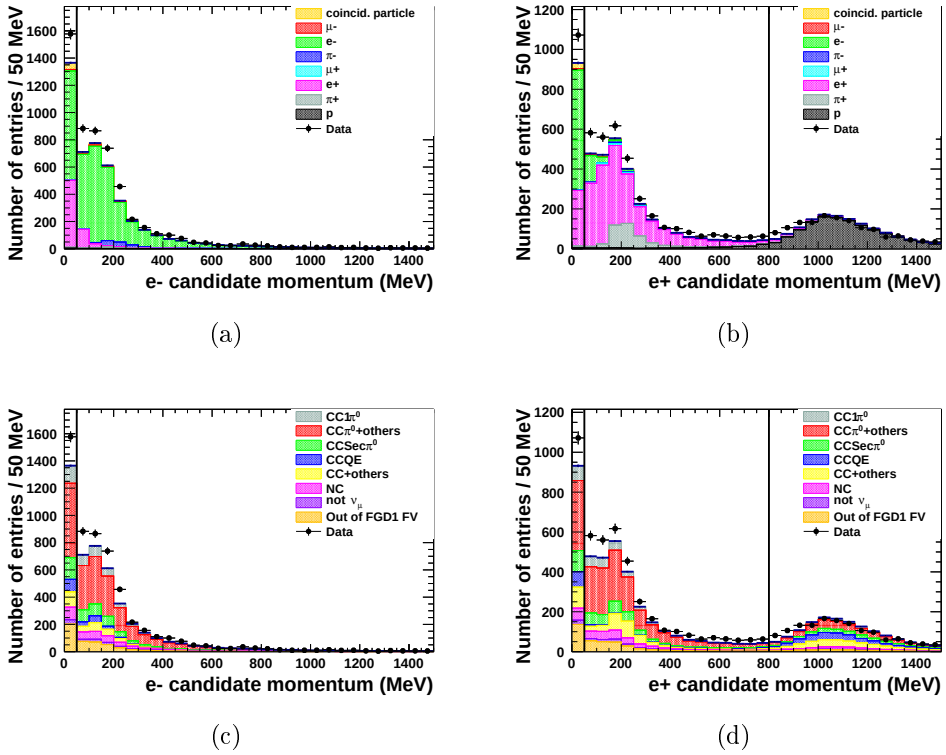

Figure 4.18: Reconstructed momentum of the selected $e^{\pm}$ candidates in the TPC after $\nu_\mu CC$ cuts (Sec. 4.3) and after 1-4 $e^{\pm}$ cuts. The distributions are scaled to real data POT given in Table 3.1. The left column corresponds to the negative TPC tracks and the right column – to the positive TPC tracks. The upper row distributions are split according to the true particle type of the selected $e^{\pm}$ candidates. The bottom row contains plots with Monte Carlo split according to the neutrino reaction type (defined in Table 1.1). The black lines on the plots show the values of cuts 5 and 6.

No.	TPC tracks after cut:	real data	MC	data/MC ratio	signal reaction purity	true $e\pm$ pur.	true $e\pm$ eff.
1.	all TPC tracks	45820	42198	1.086	36.3%	46.5%	100%
2.	nodes > 18	38007	35528	1.070	36.9%	42.8%	77.6%
3.	start in FGD extended volume	29892	27112	1.103	39.1%	33.4%	46.2%
4.	$Pull_e \in (-2, 2.5)$	11761	10148	1.159	51.2%	75.0%	38.8%
5.	momentum < 800 MeV, for positive tracks	10036	8500	1.181	54.5%	87.8%	38.1%
6.	momentum > 50 MeV	7387	6187	1.194	57.1%	84.2%	26.6%

Table 4.5: Characteristics of the TPC tracks after each $e^{\pm}$ cut: reduction of the track number in the real data and MC scaled to the real data POT, real data/MC POT scaled ratio, purity of the selection of particles produced in $(\nu_\mu CC\pi^0)_{incl.}$ reaction, purity and efficiency of the selection of true $e^{\pm}$ tracks from produced in any type of interaction.

True particle	
"Signal" particles	
e^-	48.9
e^+	34.7
"Background" particles	
π^+	7.2
π^-	2.5
p	2.3
μ^-	2.1
coincidental particle	1.3
μ^+	0.7

True topology	
Signal reactions	
$\nu_\mu CC1\pi^0$	9.3
$\nu_\mu CC\pi^0 + others$	47.6
Background reactions	
$\nu_\mu CCsec\pi^0$	11.2
$\nu_\mu CC + others$	9.4
Out of FGD1 FV	8.8
$\nu_\mu NC$	8.0
$\nu_\mu CCQE$	2.9
not ν_μ	2.6

Table 4.6: Percentages of the type of true particle and true reaction for the selected sample of $e^{\pm}$ candidates. True electrons and positrons from the same neutrino reaction as the muon candidate are denotes as the "signal" particles. They do not have to come from the $(\nu_\mu CC\pi^0)_{incl.}$ reaction, as the selection is oriented towards $e^{\pm}$ tracks, not the $(\nu_\mu CC\pi^0)_{incl.}$ reaction itself. The "background" particles are all other types of the particles.

4.4.2.2 Photon candidates in the ECal

To select the photons converting in the ECal, three basic steps were done:

1. All isolated ECal objects were considered, i.e. objects inside the ECal without any part in other subdetectors.

   Among such objects 14% come from a different reaction than the muon candidate (coincidental particles); in 99% these are neutrino interactions outside the FGD1 volume. The particles produced in those coincidental reactions are mainly muons (55%), protons (17%), $e^{\pm}/\gamma$ (15%) and charged pions (8%).

   For particles produced in the same neutrino reaction as the muon candidate, the neutrino interaction vertex is located in FGD1 in 91%, but only 21% of the particles truly start in FGD1, usually on its borders (Fig. 4.19), making their reconstruction difficult. The isolated ECal objects from those reactions are produced in 36% by the products of the primary π^0 decay, and in 26% by $e^{\pm}$ and γ from other sources. The contributions from protons, $\pi^{\pm}$ and muons are 15%, 13% and 7%, respectively. Only 26% of protons start in FGD1, while 76% are produced through rescattering of primary hadrons. For charged pions, 48% start in FGD1 and 58% are produced in secondary interactions. The muons start in the FGD1 (78%), usually close to its upper edge, TECal (9%), dead material (9%) and other subdetectors.

2. Track-like objects were rejected. This cut allows us to significantly reduce the muon contribution and, to a lesser extent, the proton and charged pion contributions. Figure 4.20 shows the contributions of true particles for track-like and shower-like isolated ECal objects for the whole sample of events, as well as for the signal and background reactions separately.

3. The electromagnetic energy of the shower had to be larger than 50 MeV. This cut rejects low-energy cascades, which are difficult to identify. The electromagnetic energy of the photon candidates before this cut is shown in Figure 4.21.

The efficiency, purity and reduction of the number of the photon candidates after each cut is given in Table 4.7. It is assumed that after the first cut, i.e. the selection of all isolated ECal objects, the efficiency equals 100%.

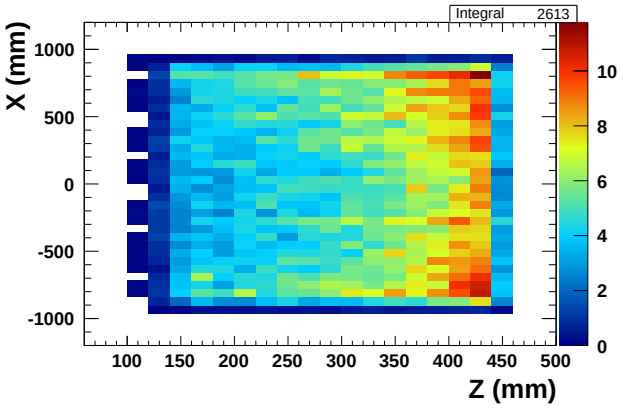

(a)

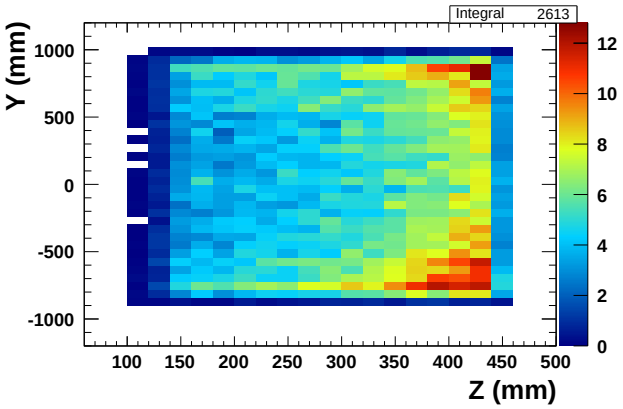

(b)

Figure 4.19: True start position of the charged particles truly starting in the FGD1 volume, but reconstructed as isolated objects in the ECal from the events selected after the $\nu_\mu CC$ cuts described in Sec. 4.3 and after the first ECal photon cut. The distributions are scaled to real data POT given in Table 3.1. Plot (a) shows Z-X coordinates and plot (b) – Z-Y coordinates.

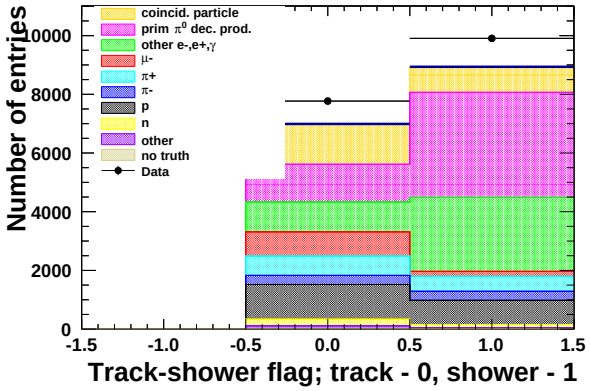

(a)

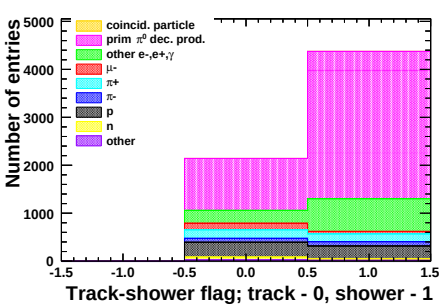

(b)

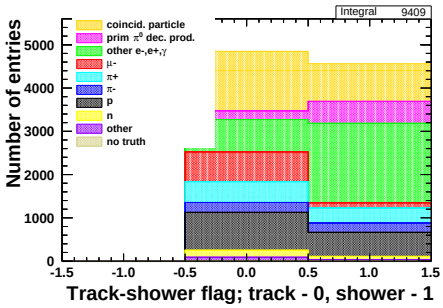

(c)

Figure 4.20: Track-shower flag (0 – track, 1 – shower) of the selected isolated ECal objects after the $\nu_\mu CC$ cuts and after the first ECal photon cut. The Monte Carlo distributions are split according to the true particle type of the selected photon candidates in the ECal and scaled to real data POT given in Table 3.1. Plot (a) corresponds to all isolated ECal objects. Plot (b) contains objects associated with the signal reaction only, and plot (c) – with the background reactions. The distributions (b) and (c) contain only MC data.

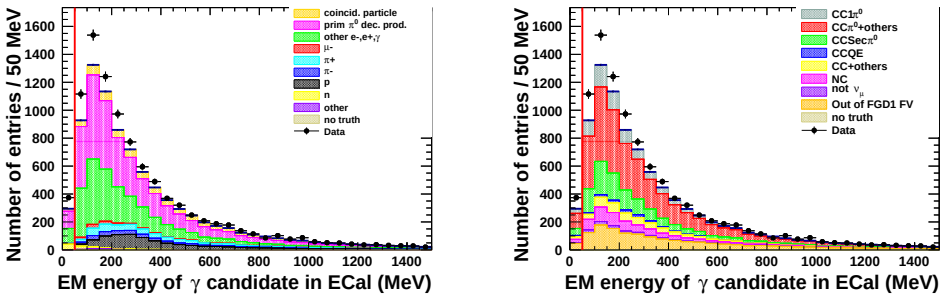

(a) (b)

Figure 4.21: Electromagnetic energy of the selected photon candidates in the ECal after the $\nu_\mu CC$ cuts and after 1-2 ECal photon cuts. The distributions are scaled to real data POT given in Table 3.1. The plots correspond to the whole sample of the selected ECal showers before the last cut, showed by the red line. Plot (a) presents the distributions with Monte Carlo split according to the true particle type of the selected photon candidates in the ECal. In plot (b) Monte Carlo is split according to the neutrino reaction type (defined in Table 1.1).

The reaction and particle composition of the selected shower sample after all cuts is presented in Table 4.8. The final purity and efficiency of the primary π^0 decay products selection equal to 41.6% and 71.2% respectively. 49% of the selected showers come from particles produced in the $(\nu_\mu CC\pi^0)_{incl.}$ reaction; 86% of them are $e^\pm, \gamma$ from the decays of the primary π^0's or from different sources. The largest contribution to the background (28.0%) comes from $e^\pm, \gamma$ not produced by the primary π^0's, but originating mainly from the reinteractions of other particles inside the detector. At the present stage of the software development it is very hard to distinguish this background from the products of the primary π^0 decays, which is due to a poor quality of the shower direction reconstruction. The second important background are coincidental particles from different neutrino vertex than the muon candidate (9.9%); around half of them are true muons and protons from reactions inside the ECal and SMRD. Other main contributions are following particles from the same neutrino reaction as the muon candidate: protons (9.5%), charged pions (9.4%) and muons (1.9%).

No.	ECal objects after cut:	real data	MC	data/MC ratio	signal reaction purity	prim. π^0 pur.	prim. π^0 eff.
1.	all isolated ECal objects	17625	15895	1.109	40.9%	31.7%	100%
2.	shower-like objects	9906	8936	1.108	49.0%	41.6%	73.7%
3.	electromagnetic energy $>$ 50 MeV	9532	8642	1.103	49.0%	41.5%	71.2%

Table 4.7: Characteristics of the ECal objects after each photon cut: reduction of the reconstructed object number in the real data and MC scaled to the real data POT, real data/MC POT scaled ratio, purity of the selection of particles produced in $(\nu_\mu CC\pi^0)_{incl.}$ reaction, purity and efficiency of the selection of true primary π^0 decay products produced in any type of interaction.

True particle	
"Signal" particles	
primary π^0	
decay products	40.0
"Background" particles	
other $e^\pm$ or γ	28.0
coincidental particles	9.9
p	9.5
π^+	5.9
μ^-	1.9
π^-	3.5
n	0.7
other	0.6

True topology	
Signal reactions	
$\nu_\mu CC1\pi^0$	10.1
$\nu_\mu CC\pi^0 + others$	38.9
Background reactions	
Out of FGD1 FV	18.4
$\nu_\mu CCsec\pi^0$	15.2
$\nu_\mu NC$	7.8
$\nu_\mu CC + others$	6.1
not ν_μ	1.8
$\nu_\mu CCQE$	1.6

Table 4.8: Percentages of the type of true particle and true reaction for the selected shower sample. True primary π^0 decay products from the same neutrino reaction as the muon candidate are denotes as the "signal" particles. They do not have to come from the $(\nu_\mu CC\pi^0)_{incl.}$ reaction, as the selection is oriented towards electromagnetic cascades, not the $(\nu_\mu CC\pi^0)_{incl.}$ reaction itself. The "background" particles are all other types of the particles.

4.5 $(\nu_\mu CC\pi^0)_{incl.}$ selection – comparison between the real data and MC

After all $(\nu_\mu CC\pi^0)_{incl.}$ cuts, the number of the selected events in the real data sample is 3738, while the number expected from the MC simulations is 3387. The excess of the real data over the MC expectation is around 10%, while after the $\nu_\mu CC$ cuts a 2.4% deficit of the real data was observed (24242 of the real data events, 24847 of the expected MC events, for details see Table 4.3). As this is a significant difference, which appeared after π^0 cuts, the investigation of possible sources of this discrepancy will be presented in this section.

As described earlier, a neutral pion is assumed to be found if at least two π^0 decay products are found. Let us remind that the possible π^0 decay product combinations, described in Table 4.1, are: two showers in the ECal, two $e^\pm$ tracks in the TPC, one shower and one $e^\pm$ track, or more than two π^0 decay product candidates.

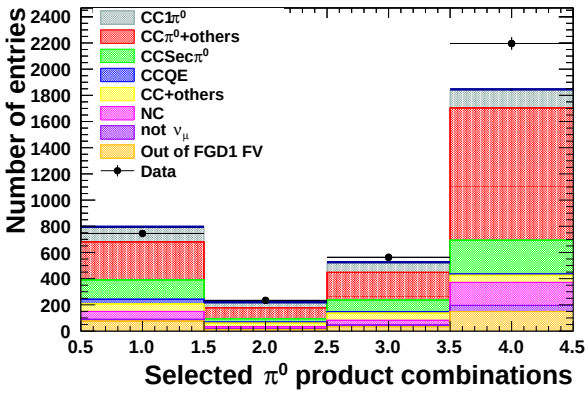

Bin labels:
1 – 2 showers
2 – 2 $e^\pm$ in TPC
3 – 1 shower and 1 $e^\pm$
4 – more than 2 π^0 decay products

Figure 4.22: Combinations of the selected π^0 decay product candidates after all cuts. The considered combinations are enumerated in the list on the right side and described in Table 4.1. The Monte Carlo distribution is split according to the neutrino reaction type (Table 1.1) and scaled to real data POT given in Table 3.1.

Figure 4.22 shows that the number of the selected MC events agrees with the real data for events with exactly 2 π^0 decay products, while MC is significantly less populated than the real data for events with more than 2 selected π^0 decay products. The following hypothetical defects of the MC simulations were considered as possible reasons for this disagreement: underestimation of the high energy tail of the neutrino beam; incorrect treatment of overlapping

events, e.g. some of the selected showers can be in fact short range muons from neutrino interactions in the ECal[2]; wrong modelling of the cross-section for neutrino interactions with multiple particles in the final state; a larger number of neutral pions produced in the secondary interactions. In the following the results of checking all these hypotheses are presented.

4.5.1 High energy neutrino beam tail

Underestimation of the high energy tail of the neutrino beam is the first possible reason of the observed disagreement, because high energy neutrinos are likelier to produce an event with more particles in the final state and the flux systematic error is higher there.

However, the distribution of the reconstructed momentum of the muon candidate in Fig. 4.23 contradicts this assumption, as the real data and MC predictions are in fairly good agreement for events with muon momenta above 3 GeV, produced by high energy neutrinos. The plot in Figure 4.24 shows that for these events an overall normalization agrees. The discrepancies between the real data and MC are at the order of one standard deviation with a small real data deficit for the events with 2 showers and a small real data overpopulation for the events with more than 2 π^0 decay products.

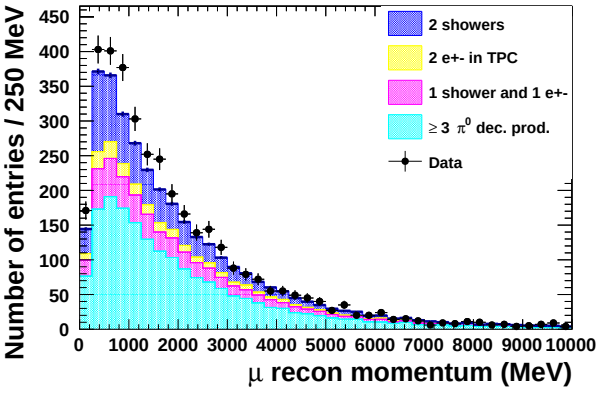

Figure 4.23: Reconstructed momentum of the selected muon candidates after all cuts. The Monte Carlo distribution is split according to the combinations of the selected π^0 decay product candidates (see legend) and scaled to real data POT given in Table 3.1.

[2]Described in section 6.3.3.5

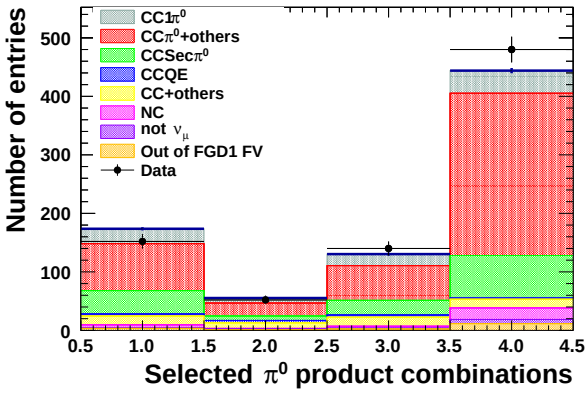

Bin labels:
1 – 2 showers
2 – 2 $e^{\pm}$ in TPC
3 – 1 shower and 1 $e^{\pm}$
4 – more than 2 π^0 decay products

Figure 4.24: Combinations of the selected π^0 decay product candidates after all cuts for the events with the muon candidate reconstructed momentum above 3 GeV. The considered combinations are enumerated in the list on the right side and described in Table 4.1. The Monte Carlo distribution is split according to the neutrino reaction type (Table 1.1) and scaled to real data POT given in Table 3.1.

Figure 4.25 depicts the relationship between the neutrino true energy and the combinations of the selected π^0 decay product candidates and the reconstructed momentum of the muon candidate after all cuts. There is no strong dependence between the number of π^0 decay product candidates and neutrino energy. Events with small reconstructed muon momenta can be produced by neutrinos with much higher momenta. Thus, it is not possible to determine the neutrino energies producing the data excess. It should be noticed that the neutrino energy distribution shown in Fig. 4.25(a) is shifted to much higher energies with respect to the average T2K neutrino beam energy, because the selection efficiency for the reaction $(\nu_\mu CC\pi^0)_{incl.}$ is very low for low neutrino energies.

To conclude, it seems that the discrepancy in Figure 4.22 does not result from the underestimation of the high energy tail of the incoming neutrinos.

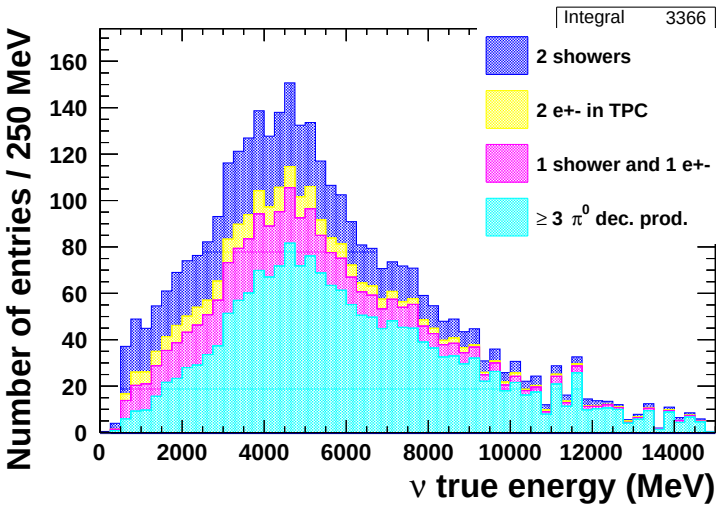

(a)

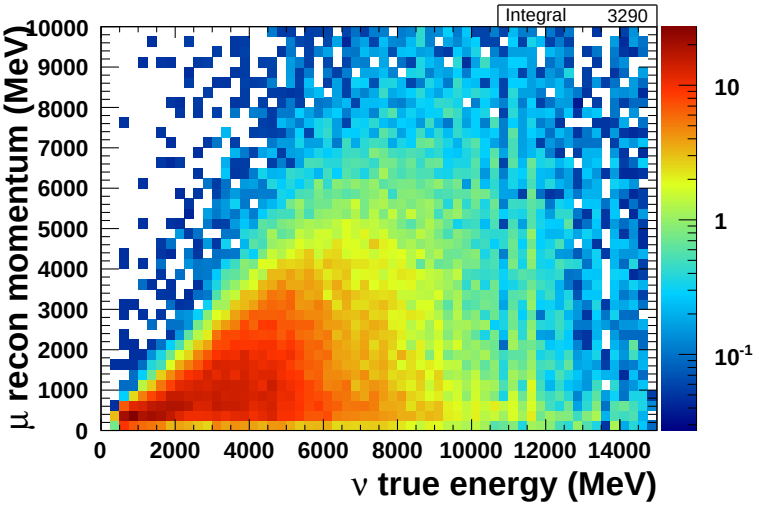

(b)

Figure 4.25: True energy of incoming neutrinos for events selected after all cuts. The distributions are scaled to real data POT given in Table 3.1. In plot (a) the Monte Carlo distribution is split according to the combinations of the selected π^0 decay product candidates (see legend). Plot (b) shows the relationship between the neutrino true energy and muon candidate reconstructed momentum.

4.5.2 Pile-up with other neutrino interactions

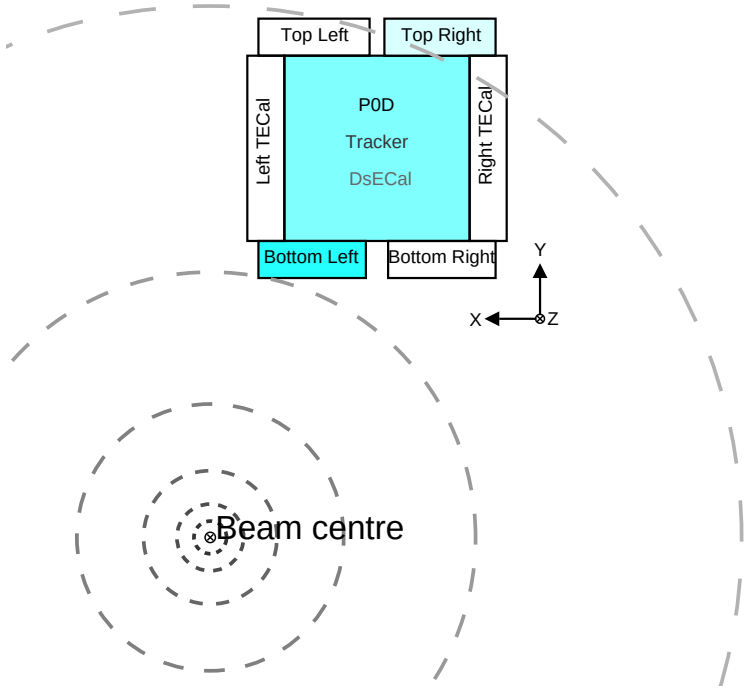

Figure 4.26: Scheme of the neutrino beam position with respect to the ND280 detector.

An overlap with particles produced in other neutrino interactions can also increase the track and shower multiplicity. To test this assumption, the real data excess in the number of showers in different parts of the ECal was compared. Photons from decays of neutral pions produced in FGD1 FV should head on each part (top, bottom, right and left) of the TECal with approximately the same probability. As it is shown in Figure 4.26, the left part of the bottom TECal is placed closest to the neutrino beam centre. Therefore, the neutrino flux is higher there, so the coincidental neutrino interactions are more likely to happen. The opposite situation is in the right part of the top TECal placed at the farthest distance from the beam centre. If the number of overlapping interactions is underestimated in the simulations, the real data excess should be higher in the left-bottom part of the TECal than in the right-top part. Plots (Fig. 4.27(a)) and (Fig. 4.27(b)) indicate that the real data excess is only slightly bigger for the ECal part placed closest to the beam centre. The most significant data-MC difference is visible in DsECal (Fig. 4.27(c)). Most particles are produced at small angles, therefore the showers in DsECal

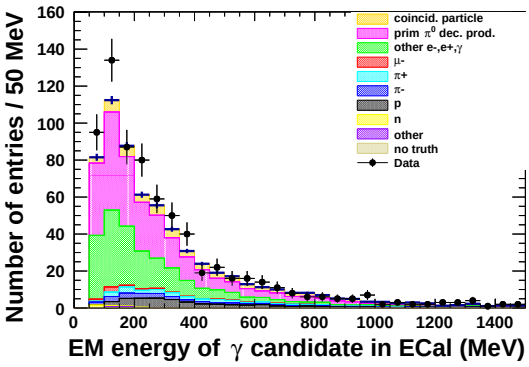

(a)

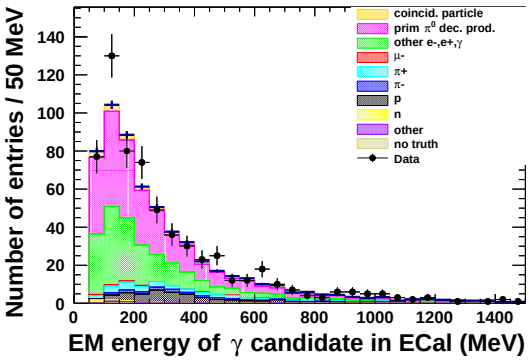

(b)

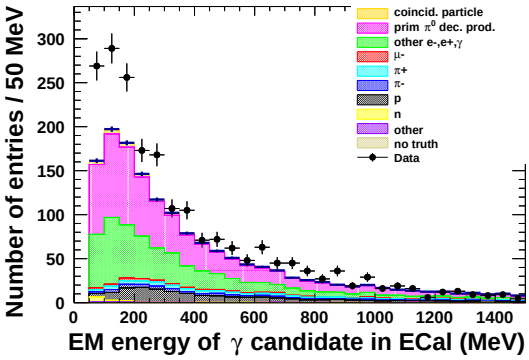

(c)

Figure 4.27: Electromagnetic energy of the selected photon candidates in the ECal after all cuts. The Monte Carlo distributions are split according to the true particle type of the selected photon candidates and scaled to real data POT given in Table 3.1. The figure presents the distributions: (a) for the left part of bottom TECal, (b) for the right part of top TECal and (c) for DsECal.

are more often produced in the same reaction as the muon candidate than the BrECal showers. The fractions of the simulated coincidental particles in the MC data shown in the plots (yellow category at the top of the distributions) are consistent with the above reasoning.

Another check performed to assess a pile-up with coincidental showers coming from a different interaction than the muon candidate is described in more detail in Subsection 6.3.3.5. The control sample of showers coming mainly from the neutrino interactions in the outer heavy part of the ND280 detector was chosen using the same cuts for the photon candidates in the ECal as in the analysis sample, but the selected events did not contain the reconstructed objects inside the tracker. The data-MC difference in the number of such showers in the control sample turned out to be at the level of 9%. This should increase the number of selected events by less than 1%, so it cannot explain the entire discrepancy observed in the selected analysis sample.

To sum up, the overlapping events are responsible for the surplus of the showers in the real data only in a small part. Most showers causing it truly come from the same interaction as the muon candidate.

4.5.3 Particle multiplicity

Higher particle multiplicity in the selected events is the reason suggested by the discrepancy in DsECal (Fig. 4.27(c)). The distributions in Figure 4.28 depict the multiplicity of the objects reconstructed in the tracker, TECal and DsECal after $\nu_\mu CC$ cuts (plot (a)) and after all $(\nu_\mu CC\pi^0)_{incl.}$ cuts (plot (b)). In the inclusive $\nu_\mu CC$ sample a deficit of the events with a low reconstructed object multiplicity can be observed in the real data. In the final $(\nu_\mu CC\pi^0)_{incl.}$ sample, the real data events are shifted towards higher multiplicities. For the selected events within the category with more than 2 π^0 decay product candidates, there is a shift to higher multiplicities in the number of showers in ECal (Fig. 4.29(a)). The shape of the multiplicity distribution for the $e^\pm$ candidates in TPC (Fig. 4.29(b)) in the real data is in agreement with MC. An increase in the number of neutral pions should cause an increase in all types of π^0 decay products, so both showers and $e^\pm$ tracks should be affected. Such behaviour is not observed here.

All that suggests that the true multiplicity of particles in the selected neutrino interactions is higher than expected from MC simulations and that it partly causes disagreements in the number of selected events and an overabun-

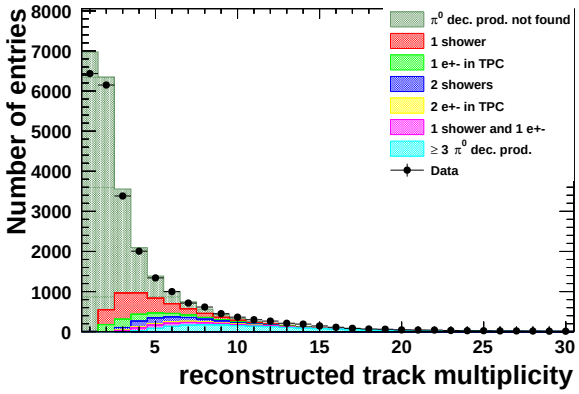

(a)

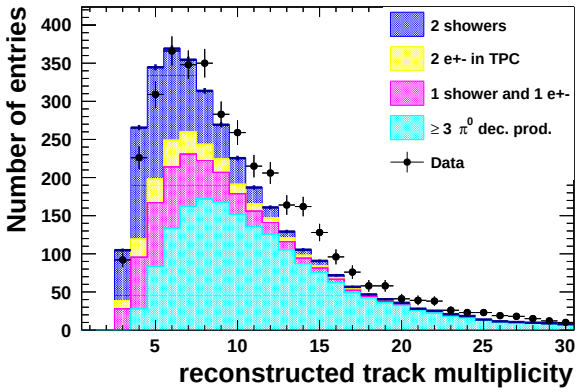

(b)

Figure 4.28: Reconstructed object multiplicity in the tracker and surrounding calorimeter (TECal and DsECal) after the $\nu_\mu CC$ cuts on top (a) and after all $(\nu_\mu CC\pi^0)_{incl.}$ cuts on bottom (b). The Monte Carlo distribution is split according to the combinations of the selected π^0 decay product candidates (Table 4.1) and scaled to real data POT given in Table 3.1.

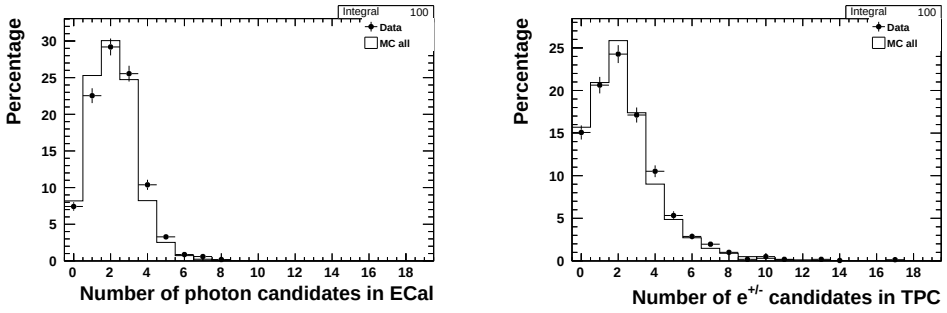

(a) (b)

Figure 4.29: Number of (a) photon candidates in ECal and (b) $e^{\pm}$ candidates in TPC after all cuts for the events with more than two π^0 decay product candidates. The plots are normalized to 100 to show better shape differences between real data and MC.

dance of events with more than 2 π^0 decay product candidates. Nevertheless, the types of additional particles are not clear.

4.5.4 Secondary π^0s

Neutral pions produced in the secondary interactions in the detector are hard to distinguish from the primary π^0s with the available quality of the reconstruction in the ND280 detector and the ND280 detector limitations, as it requires a very good direction reconstruction in order to decide if the reconstructed photons or pairs point to neutrino interaction vertex. Control plots for photon candidates in the ECal (Figures 4.30 and 4.31) also do not give a clear indication if the observed surplus of showers comes from the primary or secondary π^0s, or from other particles.

In the distributions with the reconstructed invariant mass of the two most energetic showers and their opening angle (Fig. 4.30) the excess of the real data seems to agree with the showers category denoted as "other e^-, e^+, γ", which mainly contains the products of the secondary π^0 decays. Figure 4.31 presents the angle between the shower reconstructed direction and the direction determined from the muon candidate start position and shower start position. The real data excess in this distribution can be partly explained by the underestimation of the "other e^-, e^+, γ" category in the MC simulations. However, additional effects may be required to explain the real data excess between 1 and 1.5 radian.

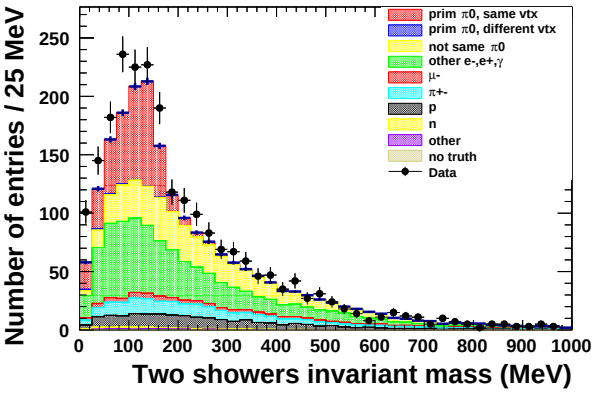

(a)

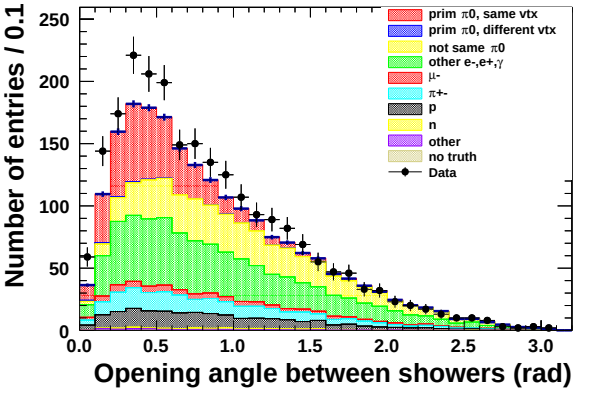

(b)

Figure 4.30: Reconstructed (a) invariant mass and (b) opening angle of the two most energetic showers selected in the ECal after all cuts. The Monte Carlo distributions are split according to the true particle type of the selected photon candidates in the ECal and scaled to real data POT given in Table 3.1.

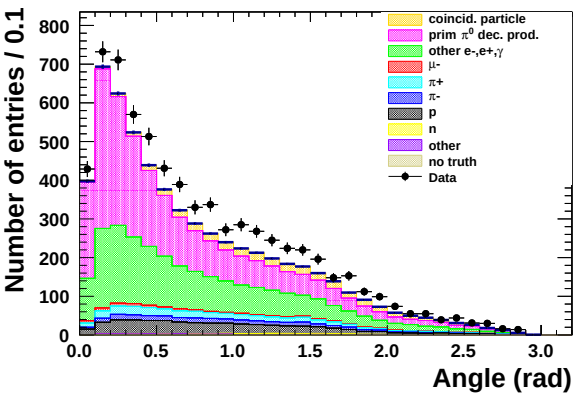

Figure 4.31: Angle between the reconstructed shower direction and vector leading from the muon candidate reconstructed start position to shower reconstructed start position of the selected photon candidates in the ECal after all cuts. The Monte Carlo distributions are split according to the true particle type of the selected photon candidates in the ECal and scaled to real data POT given in Table 3.1.

The above information suggests that the real data excess may originate from the underestimation of the number of the secondary π^0s. However, the difference between the control distributions for different types of particles is too small to draw firm conclusions.

4.5.5 Summary of the real data-MC comparison

The largest discrepancy between the measured and simulated events appears in the topology with more than 2 π^0 decay product candidates. The analysis of such events is complicated because of a high number of the reconstructed objects that need to be considered. Additionally, each of these objects can be located in different subdetectors, so they can be affected by a different set of systematic effects.

The control plots presented in this section do not indicate one clear source of the discussed discrepancy. The conducted analysis suggests that the real data excess originates mainly from the particles produced in the same neutrino reaction as the muon candidate. The true multiplicity of the particles in the selected events seems to be higher than expected from the MC simulations. However, it is possible that the additional particles are produced in the secondary interactions and not directly in the neutrino primary interaction. Another issue that can contribute to a higher number of the observed reconstructed objects in the real data, which was not discussed in this section, is the inefficiency of matching the reconstructed objects from different subdetectors. Section 6.3.3.3 presents a procedure of determining the difference between the real data and MC for TPC-ECal matching efficiency. It was assessed that it could change the number of selected events by less than 0.1%, but further studies for other subdetectors are needed.

The origin of the surplus of the selected real data events should be investigated in the future by taking advantage of larger data statistics and an improved reconstruction software that will be used in the upcoming production 7.

4.6 Selection summary

The $(\nu_\mu CC\pi^0)_{incl.}$ selection is performed in two main stages:

1. First the $\nu_\mu CC$ inclusive sample is chosen using the official cuts listed in Section 4.3.

2. Then events with π^0s are selected according to the cuts described in Section 4.4.

The number of true signal events before cuts, as well as the number of the selected events after both stages, is shown in Table 4.9.

	True events before cuts
$\nu_\mu CC1\pi^0$ events	2393
$\nu_\mu CC\pi^0 + others$ events	3759
Total $(\nu_\mu CC\pi^0)_{incl.}$ events	6152

	Selected events					
	after $\nu_\mu CC$ cuts			after all cuts		
Number of real data events	24242			3738		
Number of MC events	24847			3387		
data/MC ratio	0.976			1.104		
	events	eff.	pur.	events	eff.	pur.
$\nu_\mu CC$	22350	90%	53%	2752	81%	7%
$\nu_\mu CC1\pi^0$	1243	5%	52%	376	11%	16%
$\nu_\mu CC\pi^0 + others$	2564	10%	68%	1595	47%	42%
Total $(\nu_\mu CC\pi^0)_{incl.}$	3807	15%	62%	1971	58%	32%

Table 4.9: Number of true signal events before cuts, as well as the number of selected events, purity and efficiency after the $\nu_\mu CC$ cuts and all cuts. $\nu_\mu CC1\pi^0$ and $\nu_\mu CC\pi^0 + others$ add up to $(\nu_\mu CC\pi^0)_{incl.}$. The number of true signal events is a denominator in the signal selection efficiency calculations.

The reconstructed momentum and $\cos\theta$ distributions of the muon candidates after all cuts for the $(\nu_\mu CC\pi^0)_{incl.}$ selection are shown in Figure 4.32 and can be compared with analogical distributions after $\nu_\mu CC$ cuts in Fig. 4.4. The

momentum distribution after all cuts is flatter and extends to higher momenta. The sample contains a larger contribution of negative pions misidentified as muons, which leads to a larger contribution of NC interactions.

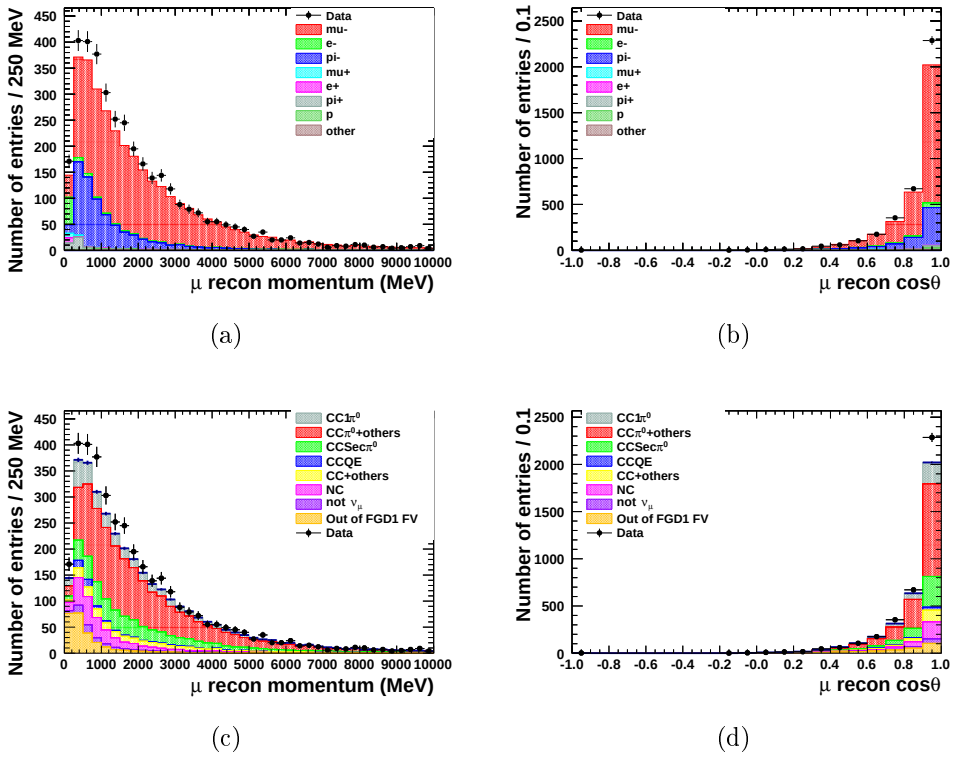

Figure 4.32: Characteristics of the selected muon candidates after all cuts. MC distributions are scaled to real data POT given in Table 3.1. The left column plots show the reconstructed momentum and the right column ones – the reconstructed $\cos\theta$. In the upper row one can find the distributions with Monte Carlo split according to the true particle type of the selected muon candidate. The bottom row contains the plots with Monte Carlo split according to the neutrino reaction type (see Table 1.1).

The number of the selected events and purities for different π^0 decay product combinations were shown in Figure 4.22 and are summarised in Table 4.10. The overall purity of all π^0 decay product combinations is 58%. The subsample with exactly 2 showers and no $e^{\pm}$ track in TPC has the lowest purity (51%). The purity of "two $e^{\pm}$" and "one $e^{\pm}$ and 1 shower" sample equals 58% and 55% respectively. The subsample with more than two π^0 decay products has the highest purity (62%), which is understandable because for the events with many particles in the final state there is a higher probability that at least one

of them will be π^0. We can see that the purity of the "two $e^{\pm}$" subsample does not differ significantly from others, despite the fact that two $e^{\pm}$ can be produced by only one photon (Table 4.1).

Distributions in Fig. 4.33 depict the true neutrino energy distribution of the true signal events before cuts (a) and of the selected events after all cuts (b). Most of the events below 2 GeV, especially the peak from $\nu_\mu CC1\pi^0$, are lost during the selection, in which at least two π^0 decay products are required. This fact can be also observed in the efficiency distribution in Figure 4.34, which shows that the efficiency is low below 2 GeV and it increases steadily with the neutrino energy, while the purity is roughly flat, except for the first bin.

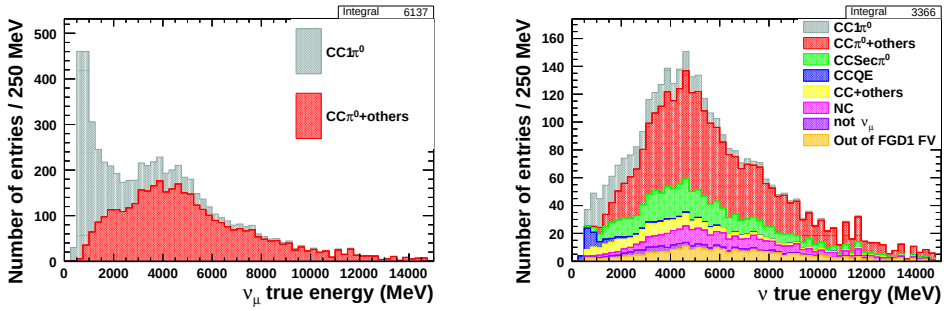

(a) (b)

Figure 4.33: True energy of the incoming neutrinos for all $(\nu_\mu CC\pi^0)_{incl.}$ events before cuts (plot (a)) and for the events selected after all cuts (plot (b)). The Monte Carlo distributions are split according to the neutrino reaction type (see Table 1.1) and scaled to real data POT given in Table 3.1.

Figure 4.35 depicts the selection efficiency dependence on the true muon momentum and $\cos\theta$, as well as the true π^0 multiplicity. For the true muon momentum, the efficiency for the events below 1 GeV is about 20%, and for the rest of events it remains at the same level of about 45%. The applied muon selection cuts are not oriented towards the backward going particles and muons at high angles. Therefore, the efficiency for them is below 10%. For the forward going particles the efficiency grows with the value of $\cos\theta$. The plot with the primary π^0 multiplicity shows that a lot of events with one neutral pion in the final state are lost at the second stage of the selection. The π^0 selection requires two π^0 decay products and in Sec. 4.4.1 it was checked that the lower energy photon from π^0 decay is very often lost. It should be pointed

	Combinations of selected π^0 decay products				
	2 shower	2 $e^{\pm}$	1 sh. & 1 $e^{\pm}$	> 2 π^0 decay products	whole selected sample (≥ 2 π^0 decay products)
Number of real data events	745	234	563	2196	3738
Number of expected events	796	220	526	1846	3387
data/MC ratio	0.936	1.064	1.070	1.190	1.104
signal reaction	Signal selection purities (%)				
$\nu_\mu CC1\pi^0$	14.4	19.1	14.7	7.7	11.1
$\nu_\mu CC\pi^0 + others$	36.5	38.1	40.2	54.7	47.1
signal total	50.9	58.2	54.9	62.4	58.2
background reaction	Background contributions (%)				
$\nu_\mu CCsec\pi^0$	18.6	11.5	17.0	14.0	15.4
$\nu_\mu CCQE$	4.5	4.0	2.1	0.5	1.9
$\nu_\mu CC + others$	7.2	12.4	10.4	3.0	5.7
$\nu_\mu NC1\pi^0$	0.1	0.3	0.2	0.1	0.1
$\nu_\mu NC\pi^0 + others$	4.2	4.8	4.1	7.5	6.0
$\nu_\mu NCsec\pi^0$	2.8	1.1	1.9	1.8	2.0
$\nu_\mu NCE$	0.0	0.0	0.0	0.0	0.0
$\nu_\mu NC + others$	0.5	0.3	0.6	0.1	0.3
not ν_μ	1.7	2.8	2.4	2.5	2.3
out of FGD1 FV	9.6	5.7	6.4	8.1	8.0
background total	49.1	41.8	45.1	37.6	41.8

Table 4.10: Number of events in the real data and in Monte Carlo, and data/MC ratio for different combinations of selected π^0 decay products (upper part of the table). Percentage purity values and background contributions of the selected events for different combinations of selected π^0 decay products (lower part of the table).

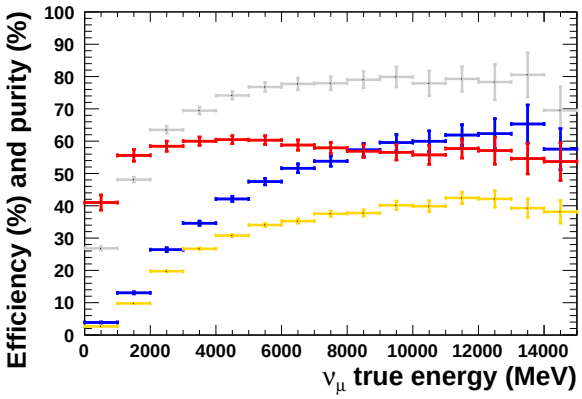

Figure 4.34: Final $(\nu_\mu CC\pi^0)_{incl.}$ selection efficiency after the $\nu_\mu CC$ cuts (gray) and after all cuts (blue) and purity after the $\nu_\mu CC$ cuts (yellow) and after all cuts (red) with respect to the true neutrino energy.

out that events in the first bin, i.e. with one π^0 , are not only $\nu_\mu CC1\pi^0$, but also $\nu_\mu CC\pi^0 + X$ with exactly one π^0 and at least one other meson in the final state. For the events with two primary π^0s a drop in the efficiency at the second stage of the selection with respect to the first stage is visible, but it is not so dramatic. For the events with more than two π^0s the inefficiency is at the same level as after the $\nu_\mu CC$ selection. The statistical error for the events with 5 and 6 primary π^0s is too large to draw any conclusions for them.

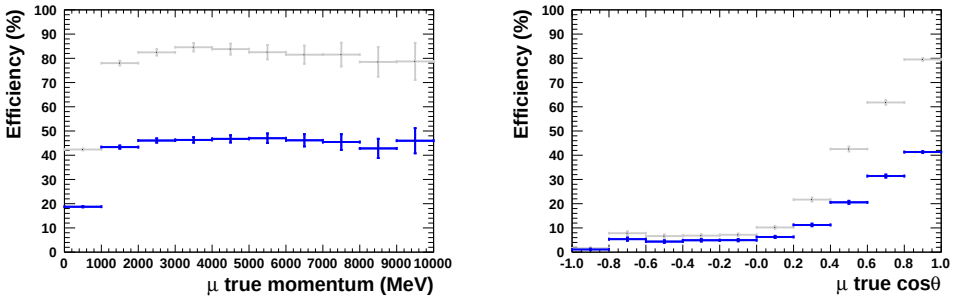

(a) (b)

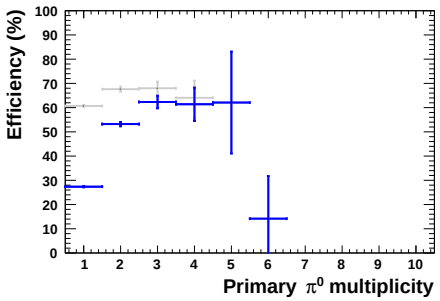

(c)

Figure 4.35: Final $(\nu_\mu CC\pi^0)_{incl.}$ selection efficiency after the $\nu_\mu CC$ cuts (gray) and after all cuts (blue) with respect to (a) the true muon momentum, (b) true muon $\cos\theta$ and (c) true neutral pion multiplicity.

Chapter 5

Total flux-averaged cross-section

The number of events n corresponding to the signal reaction depends on the number of target nucleons T, the incident neutrino flux per unit area $\Phi(E_\nu)$ and the signal cross-section $\sigma(E_\nu)$ as a function of neutrino energy E_ν, and is described by:

$$n = T \int \sigma(E_\nu) \frac{\partial \Phi(E_\nu)}{\partial E_\nu} dE_\nu. \tag{5.1}$$

In this analysis the energies of interacting individual neutrinos are not known. Therefore, a simplified formula with the flux-averaged cross-section $\langle\sigma\rangle$ and the total integrated neutrino flux per unit area Φ is used:

$$n = T \cdot \langle\sigma\rangle \cdot \Phi. \tag{5.2}$$

Thus, the total flux-averaged cross-section of the $(\nu_\mu CC\pi^0)_{incl.}$ interaction with the vertex in FGD1 FV is given by:

$$\langle\sigma\rangle = \frac{n}{T \cdot \Phi_{\nu_\mu}}, \tag{5.3}$$

where

- n is the number of the $(\nu_\mu CC\pi^0)_{incl.}$ events with the vertex inside FGD1 FV,
- T is the number of nucleons inside FGD1 FV, as the $(\nu_\mu CC\pi^0)_{incl.}$ reaction can originate from a neutrino interaction on both proton and neutron,
- Φ_{ν_μ} is the total integrated flux per cm^2 of the muon neutrinos crossing FGD1 FV; in the interactions of other neutrino flavours in the T2K

neutrino beam ($\overline{\nu}_\mu, \nu_e, \overline{\nu}_e$) a negative muon, required by the signal definition, cannot be produced, so such neutrinos contribute only to the background.

The number of the target nucleons T is the number of nucleons comprising the FGD1 FV (defined in Table 4.2), regardless of a type of nuclei they belong to. According to [34]:

$$T = 5.50 \times 10^{29} \text{ nucleons.} \tag{5.4}$$

The contribution of protons and neutrons is 53.6% and 46.4%, respectively.

The value of the total integrated muon neutrino flux per cm^2 Φ_{ν_μ} for each run is calculated from the flux files (version tuned13av1.1), provided by the beam group, multiplied by the number of collected POT.

$$\Phi_{\nu_\mu} = POT^{data(MC)} \cdot \phi_{\nu_\mu}, \tag{5.5}$$

where

- $POT^{data(MC)}$ is the number of POT in the real (simulated) data,
- ϕ_{ν_μ} is the muon neutrino flux per cm^2 per number of collected POT.

The actual neutrino flux changes across the ND280 detector volume, in particular across the FGD1 fiducial volume. However, in the above calculation the neutrino flux averaged over a 150×150 cm^2 X-Y plane, located at the centre of the ND280 detector [23], was used. The plane overlaps largely with the FGD1 FV X-Y projection, therefore this is a sufficient approximation.

In the MC sample the number of the signal events before cuts n^{MC} is known. The number of the signal events in the real data n^{data} sample is evaluated from the number of the real data events selected by applying all $(\nu_\mu CC\pi^0)_{incl.}$ cuts N^{data}, as well as the simulated efficiency ϵ and background contamination of this selection:

$$n^{data} = \frac{N^{data} - B^{MC} \cdot norm}{\epsilon}, \tag{5.6}$$

where

- N^{data} is the number of all selected events in the real data sample,
- B^{MC} is the number of the selected background events in the MC sample,

- $norm = POT^{data}/POT^{MC}$ is the ratio between the number of POT in the real data (POT^{data}) and in the MC sample (POT^{MC}),
- ϵ is the selection efficiency predicted by MC.

Efficiency ϵ is defined as:

$$\epsilon = \frac{S^{MC}}{n^{MC}}, \tag{5.7}$$

where

- S^{MC} is the number of the selected signal events in FGD1 FV in the MC sample,
- n^{MC} is the number of the signal events before cuts in FGD1 FV simulated in the MC sample.

The neutrino flux, selection efficiency and purity can differ between runs of data taking. Therefore, cross-section has to be calculated for each run separately using formula (5.3). Then, the POT-weighted average is calculated:

$$\begin{aligned} \langle\sigma\rangle^{data(MC)} &= \sum_{r=2,3c,4} \frac{POT_r^{data(MC)}}{POT_{tot}^{data(MC)}} \cdot \langle\sigma\rangle_r = \frac{1}{POT_{tot}^{data(MC)} \cdot T} \sum_{r=2,3c,4} \frac{n_r^{data(MC)}}{\phi_{\nu_\mu,r}}, \\ n_r^{data} &= \frac{N_r^{data} - B_r^{MC} \cdot norm_r}{S_r^{MC}/n_r^{MC}}, \end{aligned} \tag{5.8}$$

where

- r subscript denotes the value for the data taking period: run 2, run 3c or run 4,
- $POT_{tot}^{data(MC)}$ denotes the collected number of POT in the real data (MC) sample of all runs:

$$\begin{aligned} POT_{tot}^{data} &= 0.549 \times 10^{21}, \\ POT_{tot}^{MC} &= 12.21 \times 10^{21}. \end{aligned} \tag{5.9}$$

The statistical error (denoted as δ) of the cross-section is calculated as the sum of contributions from individual variables added in quadrature. The contribution from the particular variable is calculated as partial derivative of the cross-section times statistical error of this variable, which is its square root.

The variables, whose contribution to the statistical error is taken into account, are n_r^{MC} for the MC prediction and $N_r^{data}, B_r^{MC}, S_r^{MC}$ and n_r^{MC} for the real data. The formula of the statistical error for the MC prediction is:

$$\begin{aligned}\delta\langle\sigma\rangle^{MC} &= \sqrt{\sum_{r=2,3c,4}\left(\frac{\partial\langle\sigma\rangle_r^{MC}}{\partial n_r^{MC}}\cdot\delta n_r^{MC}\right)^2} \\ &= \frac{1}{POT_{tot}^{MC}\cdot T}\sqrt{\sum_{r=2,3c,4}\left(\frac{1}{\phi_{\nu_\mu,r}}\cdot\sqrt{n_r^{MC}}\right)^2}.\end{aligned} \tag{5.10}$$

The statistical error for the real data measurement can be expressed as a function of the n_r^{data} statistical error:

$$\delta\langle\sigma\rangle^{data} = \frac{1}{POT_{tot}^{data}\cdot T}\sqrt{\sum_{r=2,3c,4}\left(\frac{1}{\phi_{\nu_\mu,r}}\right)^2\cdot(\delta n_r^{data})^2}. \tag{5.11}$$

The n_r^{data} statistical error equals:

$$\begin{aligned}\left(\delta n_r^{data}\right)^2 = &\left(\frac{\partial n_r^{data}}{\partial N_r^{data}}\cdot\delta N_r^{data}\right)^2 + \left(\frac{\partial n_r^{data}}{\partial B_r^{MC}}\cdot\delta B_r^{MC}\right)^2 \\ &+ \left(\frac{\partial n_r^{data}}{\partial S_r^{MC}}\cdot\delta S_r^{MC}\right)^2 + \left(\frac{\partial n_r^{data}}{\partial n_r^{MC}}\cdot\delta n_r^{MC}\right)^2\end{aligned} \tag{5.12}$$

where

$$\frac{\partial n_r^{data}}{\partial N_r^{data}}\cdot\delta N_r^{data} = \frac{1}{S_r^{MC}/n_r^{MC}}\cdot\sqrt{N_r^{data}}, \tag{5.13}$$

$$\frac{\partial n_r^{data}}{\partial B_r^{MC}}\cdot\delta B_r^{MC} = -\frac{norm_r}{S_r^{MC}/n_r^{MC}}\cdot\sqrt{B_r^{MC}}, \tag{5.14}$$

$$\frac{\partial n_r^{data}}{\partial S_r^{MC}}\cdot\delta S_r^{MC} = -\frac{N_r^{data}-B_r^{MC}\cdot norm_r}{(S_r^{MC})^2/n_r^{MC}}\cdot\sqrt{S_r^{MC}}, \tag{5.15}$$

$$\frac{\partial n_r^{data}}{\partial n_r^{MC}}\cdot\delta n_r^{MC} = \frac{N_r^{data}-B_r^{MC}\cdot norm_r}{S_r^{MC}}\cdot\sqrt{n_r^{MC}}. \tag{5.16}$$

The input values needed for the $(\nu_\mu CC\pi^0)_{incl.}$ cross-section calculations are listed in Table 5.1. The total flux averaged cross-section values of the $(\nu_\mu CC\pi^0)_{incl.}$ reaction, predicted by NEUT generator and measured in the real data, are as follows:

$$\langle\sigma\rangle^{MC} = (1.0522\pm0.0028(stat))\times10^{-39}\ \mathrm{cm}^2/\mathrm{nucleon}, \tag{5.17}$$

$$\langle\sigma\rangle^{data} = (1.239\pm0.034(stat))\times10^{-39}\ \mathrm{cm}^2/\mathrm{nucleon}. \tag{5.18}$$

The difference between the measurement and the predictions is a result of the real data excess described in Section 4.5.

Run		Run 2	Run 3c	Run 4
POT_r^{data}	($\times 10^{21}$ POT)	0.078	0.134	0.336
POT_r^{MC}	($\times 10^{21}$ POT)	2.13	3.08	7.00
$norm_r$		0.0368	0.0435	0.0481
$\phi_{\nu_\mu,r}$	(10^{13}/cm^2/10^{21} POT)	1.928	1.937	1.942
N_r^{data}		528	922	2288
N_r^{MC}		12952	19142	43260
$N_r^{MC} \times norm_r$		477	833	2079
B_r^{MC}		5451	8029	18011
S_r^{MC}		7502	11113	25249
n_r^{MC}		23516	34618	78746
ϵ_r		0.319	0.321	0.321
n_r^{data}		1026	1784	4437
$\langle\sigma\rangle_r^{MC}$	($\times 10^{-39}$ cm^2/nucleon)	1.0422	1.0553	1.0538
$\langle\sigma\rangle_r^{data}$	($\times 10^{-39}$ cm^2/nucleon)	1.236	1.249	1.236

Table 5.1: Input values used in the $(\nu_\mu CC\pi^0)_{incl.}$ cross-section calculations.

Chapter 6

Systematics

Both the reconstruction efficiency and selection purity are never 100%. These limitations are not critical, if they are not too big and are correctly reproduced in simulations. If physics processes and the behaviour of the detector are not accurately simulated, the discrepancies have to be estimated and taken into account as systematic errors. For example, the particle charge misidentification itself is not a systematic effect, but a difference between the probability of the charge misidentification in the real and simulated data is. Similarly, an incorrect evaluation of the amount of the selected background increases the systematic uncertainties, but not the background contamination itself.

Systematic errors concern modelling of: the neutrino flux, the neutrino primary interactions and FSI, the passage through matter of particles produced in neutrino interactions and the detector response. The following sections describe an influence of each category of systematics on the calculated cross-section.

6.1 Flux uncertainty

The neutrino flux systematic uncertainty results mainly from a limited knowledge of the primary proton beam parameters, hadronic interaction model, horn current, magnetic field and neutrino beam off-axis angle [23]. The overall uncertainty of the neutrino flux in the ND280 detector is provided by the beam group in the form of a covariance matrix[1]. This covariance matrix, shown in

[1] `www.t2k.org/beam/NuFlux/FluxRelease/13arelease/13av1-1-flux-uncertainty/flux-covariance-matrix-with-fine-binning` – T2K Intranet.

Fig. 6.1, contains 80×80 elements defined with respect to the neutrino type and neutrino true energy. For each neutrino type: $\nu_\mu, \overline{\nu}_\mu, \nu_e$ and $\overline{\nu}_e$, there are 20 energy bins with edges: 0.0, 0.1, 0.2, 0.3, 0.4, 0.5, 0.6, 0.7, 0.8, 1.0, 1.2, 1.5, 2.0, 2., 3.0, 3.5, 4.0, 5.0, 7.0, 10.0 and 30.0 GeV.

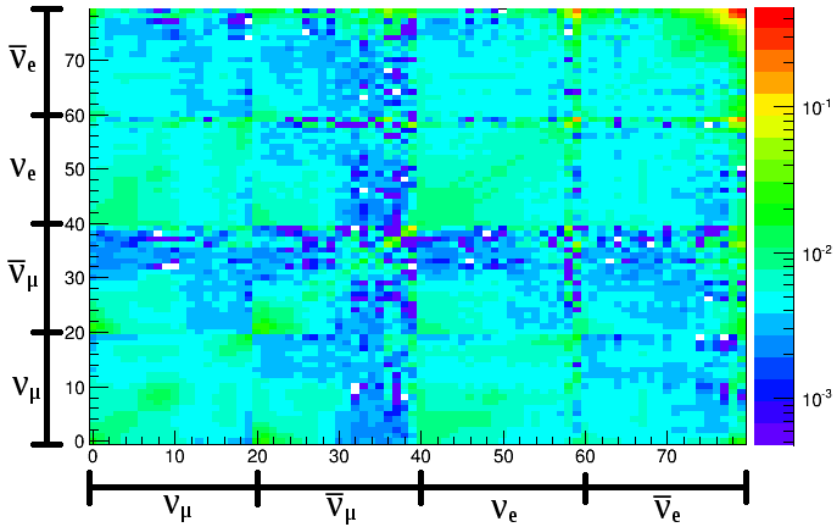

Figure 6.1: The covariance matrix of the neutrino flux systematic uncertainty in the ND280 detector.

In order to calculate the influence of the flux systematic uncertainty on the cross-section measurement, the following procedure was applied:

1. The Cholesky decomposition [98] of the neutrino flux systematics covariance matrix C was done:

$$C = L \cdot L^T \tag{6.1}$$

   where L is a lower triangular matrix and L^T is its transposition.

2. A statistically large number (100 k in this analysis) of 80 element random vectors $\vec{v}^i, i = 1, \ldots 100k$ were generated according to the standard Gaussian distribution.

3. A set of 80 element weight vectors $\vec{w}^i$ was calculated using the formula:

$$w^i_j = 1 + \sum_{k=1}^{80} L_{jk} v^i_k, \quad j = 1, \ldots, 80, \quad i = 1, \ldots, 100k. \tag{6.2}$$

The vectors $\vec{w}\,i$ were used to randomly change the selected sample within the uncertainties described in the flux covariance matrix. This procedure is called reweighting and a single change is called a random throw.

4. In the MC sample, the nominal values of the flux, the number of selected signal, background and generated signal events ($\phi_{\nu_\mu,r}, S_r^{MC}, B_r^{MC}$ and n_r^{MC} in Eq. (5.8) with r denoting run number) were divided into the same neutrino type and true energy bins as in the covariance matrix (Fig. 6.2). The nominal values are denoted with the word *nominal* in the superscript.

5. $\phi_{\nu_\mu,r}, S_r^{MC}, B_r^{MC}$ and n_r^{MC} were reweighted bin-by-bin using the formula:

$$x^i = \sum_j x_j^{nominal} \cdot w_j^i, \quad i = 1, \ldots, 100k, \tag{6.3}$$

where x^i is a reweighted value and i denotes each of 100 k random throws. Index j denotes the neutrino type and neutrino true energy bin. For B_r^{MC} – the number of selected background events $j = 1, \ldots, 80$ because they can be produced by any type of neutrino. The other three characteristics are related only to the muon neutrinos, therefore the bins related only to ν_μ were used: $j = 1, \ldots, 20$.

6. The flux-averaged $(\nu_\mu CC\pi^0)_{incl.}$ cross-section for each throw $\langle\sigma\rangle^{data,i}$ was calculated using reweighted values (bold symbols in the formula below), applied to the Equation (5.8):

$$\langle\boldsymbol{\sigma}\rangle^{\boldsymbol{data,i}} = \frac{1}{POT_{tot}^{data} \cdot T} \sum_{r=2,3c,4} \frac{N_r^{data} - \boldsymbol{B_r^{MC,i}} \cdot norm_r}{\boldsymbol{\phi_{\nu_\mu,r}^i} \cdot \boldsymbol{S_r^{MC,i}} / \boldsymbol{n_r^{MC,i}}}. \tag{6.4}$$

$\langle\sigma\rangle^{data,i}$ distribution is shown in Figure 6.3(a). Distribution in Figure 6.3(b) shows the relative difference between the cross-section nominal value $\langle\sigma\rangle^{data}$ and cross-section for each reweighting throw $\langle\sigma\rangle^{data,i}$ defined as:

$$\frac{\langle\sigma\rangle^{data,i} - \langle\sigma\rangle^{data}}{\langle\sigma\rangle^{data}}. \tag{6.5}$$

7. The flux systematic error was calculated as the difference between nominal value $\langle\sigma\rangle^{data}$ and 68% confidence level values of the $\langle\sigma\rangle^{data,i}$ distribution presented as the green lines in Figure 6.3(a). The area under the

distribution between green lines constitutes 68% of the whole area. The areas below the left green line and above the right green line are the same.

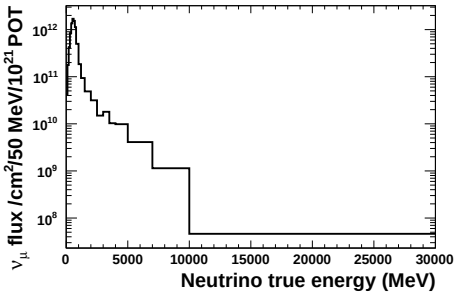

(a)

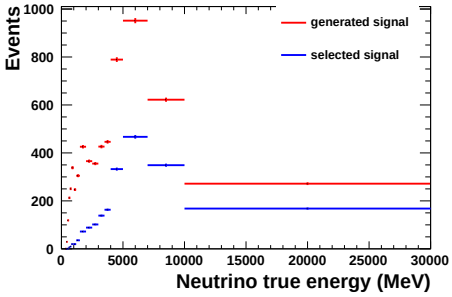

(b)

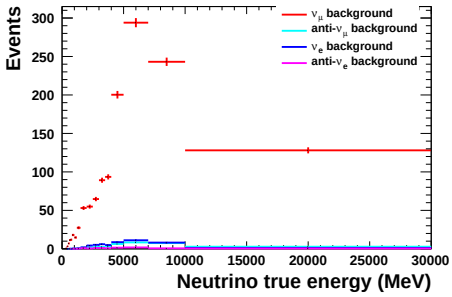

(c)

Figure 6.2: The neutrino flux (a), selected and generated signal (b) and selected background events (c) in the MC sample in the neutrino energy bins, which are the same as the energy bins in the flux systematics covariance matrix. The distributions are scaled to real data POT given in Table 3.1.

The calculated flux systematic error is asymmetric and equals:

$$\langle\sigma\rangle^{data} = (1.239^{+0.175}_{-0.149}(flux)) \times 10^{-39} \text{ cm}^2/\text{nucleon}, \tag{6.6}$$

$$\frac{\delta^{+}_{flux}\langle\sigma\rangle^{data}}{\langle\sigma\rangle^{data}} = 14.1\%, \qquad \frac{\delta^{-}_{flux}\langle\sigma\rangle^{data}}{\langle\sigma\rangle^{data}} = 12.0\%. \tag{6.7}$$

The relative flux uncertainties are bigger for neutrinos with higher energies. Thus, the flux systematic error is higher than in the $\nu_\mu CC$ inclusive analysis, because in the $(\nu_\mu CC\pi^0)_{incl.}$ analysis the average neutrino energies are higher and equal: around 4 GeV for the generated signal events and 5.5 GeV for the selected events (see Fig. 4.33).

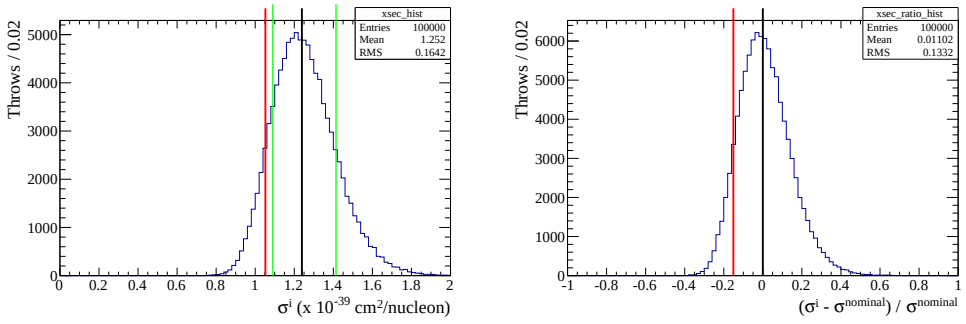

(a) (b)

Figure 6.3: The total flux-averaged $(\nu_\mu CC\pi^0)_{incl.}$ cross-section (a) and its relative error with respect to the real data cross-section nominal value (b) for each reweighting throw measured for the real data sample. The red line shows the nominal cross-section value calculated for the real data $\langle\sigma\rangle^{data}$, the black line shows the predicted value from the NEUT MC generator $\langle\sigma\rangle^{MC}$, and the green lines show the 68% confidence level.

6.2 MC model uncertainty

The MC systematic uncertainty results from uncertainties related to the model of:

- The cross-section of the neutrino primary interaction on a nucleon parton or entire nucleon bound in a nucleus and/or the neutrino coherent interaction on a whole nucleus,
- The interactions of the neutrino primary interaction products with other nucleons in a target nucleus, called Final State Interactions (FSI).

The systematic errors for these two sources are calculated separately. Both of them can influence the number of selected signal, selected background and generated signal events (S_r^{MC}, B_r^{MC} and n_r^{MC} in Equation (5.8) with r denoting the run number). The reweighting procedure is similar for both types of the systematic errors:

1. There is a set of throws for which the model parameters are varied in a way elaborated by the T2K Neutrino Interaction Working Group (NIWG).
2. For each throw weights were calculated for each relevant event, which can be selected signal, selected background and generated signal event.

3. The nominal values S_r^{MC}, B_r^{MC} and n_r^{MC} were reweighted using the formula:

$$x^i = \sum_{j=1}^{x^{nominal}} w_{x,j}^i, \quad x^{nominal} = S_r^{MC}, B_r^{MC}, n_r^{MC}, \tag{6.8}$$

where $w_{x,j}^i$ is a weight for j event from the x sample (x = selected signal, selected background, generated signal), $x^i = S_r^{MC,i}, B_r^{MC,i}, n_r^{MC,i}$ is a reweighted value and i denotes each of the throws.

4. The flux-averaged $(\nu_\mu CC\pi^0)_{incl.}$ cross-section for each throw $\langle\sigma\rangle^{data,i}$ was calculated using reweighted values (bold symbols in the formula below), applied to the Equation (5.8):

$$\langle\boldsymbol{\sigma}\rangle^{\boldsymbol{data,i}} = \frac{1}{POT_{tot}^{data} \cdot T} \sum_{r=2,3c,4} \frac{N_r^{data} - \boldsymbol{B_r^{MC,i}} \cdot norm_r}{\phi_{\nu_\mu,r}^i \cdot \boldsymbol{S_r^{MC,i}/n_r^{MC,i}}}. \tag{6.9}$$

5. At last the cross-section systematic errors were calculated in the way which is described in the following subsections, specific to the error type.

6.2.1 Neutrino primary interaction cross-section modelling

The neutrino primary interactions are described in Section 1.3.2. The neutrino primary interaction cross-section systematic error (in brief, cross-section systematic error) arises from the uncertainty of the following parameters described in detail in [99–102]:

- Parameters related to the Relativistic Fermi Gas (RFG) model:
  - The Fermi momentum in carbon (kNIWG2014a_pF_C12) and oxygen (kNIWG2014a_pF_O16).
  - The nucleon binding energy in carbon (kNIWG2014a_Eb_C12) and oxygen (kNIWG2014a_Eb_016).
- The CCQE axial mass (kNXSec_MaCCQE).
- Normalization, i.e. the overall number of events, of Meson Exchange Current (MEC) interactions on carbon (kNIWGMEC_Norm_C12) and oxygen (kNIWGMEC_Norm_O16).
- Parameters related to the CC and NC single pion resonant interactions:

  - The resonant axial mass(kNXsec_MaNFFRES).
  - The isospin $I = 1/2$ continuum background (KNXsec_BgSclRES).
  - The scaling factor for the axial form factor $C_5^A(0)$ (kNXsec_CA5RES).

- Other parameters:
  - The CC ν_e interaction normalization (kNIWG2012a_ccnueE0).
  - "CC other shape" – the parameter related to the number of CC other events as a function of the neutrino energy (kNIWG2012a_dismpishp). The CC other interactions are the CC multi-π production, CC DIS interactions and CC resonant $\eta/K/\gamma$ production.
  - The CC coherent interaction normalization (kNIWG2012a_cccohE0).
  - The NC coherent interaction normalization (kNIWG2012a_nccohE0).
  - The NC other interaction normalization (kNIWG2012a_ncotherE0).

As discussed in [100], except for the normalisation of the MEC interactions, which contribution to the error for the $(\nu_\mu CC\pi^0)_{incl.}$ interaction is negligible (see Table 6.2), most of the parameters are not correlated, so the correlations are not taken into account during reweighting. This will be improved in the future improvement of this analysis.

The values and errors of the cross-section parameters used during the reweighting procedure are listed in Table 6.1. Each of 15 parameters was varied separately by two values, which gives 30 throws. Table 6.2 presents the POT-weighted averages of relative error of the number of selected background, selected signal and generated signal events, as well as the cross-section $\langle\sigma\rangle^{data,i}$ induced by these variations. The relative errors are calculated as $(x^i - x^{nominal})/x^{nominal}$. The biggest contributions to the systematic error come from parameters describing the NC and CC other interactions, and to a lesser extent, the single pion resonant interactions.

The cross-section systematic error consists of individual contributions added in quadrature, separately for throws with the cross-section lower and higher than the nominal value $\langle\sigma\rangle^{data}$:

$$\begin{matrix}\delta^+_{xsec}\langle\sigma\rangle^{data} \\ \delta^-_{xsec}\langle\sigma\rangle^{data}\end{matrix} = \begin{cases} \sqrt{(\langle\sigma\rangle^{data,i} - \langle\sigma\rangle^{data})^2}, & \text{if} \quad \langle\sigma\rangle^{data,i} > \langle\sigma\rangle^{data} \\ & \text{if} \quad \langle\sigma\rangle^{data,i} < \langle\sigma\rangle^{data} \end{cases} \tag{6.10}$$

Parameter	T2KReWeight mean	NIWG mean	NIWG error
kNXSec_MaCCQE (GeV)	1.21	1.15	0.07
kNIWG2014a_pF_C12 (MeV/c)	217	223	12.3
kNIWG2014a_pF_O16 (MeV/c)	225	225	12.3
kNIWGMEC_Norm_C12	1	0.27	0.29
kNIWGMEC_Norm_O16	1	0.27	1.04
kNIWG2014a_Eb_C12 (MeV)	25	25	9
kNIWG2014a_Eb_016 (MeV)	27	27	9
kNXsec_CA5RES (GeV)	1.01	1.01	0.12
kNXsec_MaNFFRES	0.95	0.95	0.15
KNXsec_BgSclRES	1.30	1.30	0.20
kNIWG2012a_ccnueE0	1	1	0.02
kNIWG2012a_dismpishp	0	0	0.40
kNIWG2012a_cccohE0	1	1	1
kNIWG2012a_nccohE0	1	1	0.3
kNIWG2012a_ncotherE0	1	1	0.3

Table 6.1: Summary of the NIWG cross-section parameters. The second column (T2KReWeight mean) contains default parameter values, and the third column (NIWG mean) contains the mean values recommended by the NIWG group [102].

Thus, the calculated systematic error is asymmetric and equals:

$$\langle\sigma\rangle^{data} = (1.239^{+0.070}_{-0.072}(xsec)) \times 10^{-39} \text{ cm}^2/\text{nucleon}, \tag{6.11}$$

$$\frac{\delta^{+}_{xsec}\langle\sigma\rangle^{data}}{\langle\sigma\rangle^{data}} = 5.7\%, \qquad \frac{\delta^{-}_{xsec}\langle\sigma\rangle^{data}}{\langle\sigma\rangle^{data}} = 5.8\%. \tag{6.12}$$

Parameter	"mean diff - error" variation Relative error (%)				"mean diff + error" variation Relative error (%)			
	$\langle B_r^{MC} \rangle$	$\langle S_r^{MC} \rangle$	$\langle n_r^{MC} \rangle$	$\langle \sigma \rangle^{data,i}$	$\langle B_r^{MC} \rangle$	$\langle S_r^{MC} \rangle$	$\langle n_r^{MC} \rangle$	$\langle \sigma \rangle^{data,i}$
kNXSec_MaCCQE	-0.0051	-0.0005	-0.0024	0.12	0.0004	0.0000	0.0002	-0.01
kNIWG2014a_pF_C12	0.0003	0.0000	0.0000	-0.01	-0.0008	0.0000	-0.0001	0.05
kNIWG2014a_pF_O16	0.0000	0.0000	0.0000	0.00	0.0000	0.0000	0.0000	0.00
kNIWGMEC_Norm_C12	0.0000	0.0000	0.0000	0.00	-0.0033	-0.0001	-0.0007	0.15
kNIWGMEC_Norm_O16	0.0000	0.0000	0.0000	0.00	0.0001	0.0000	0.0000	0.00
kNIWG2014a_Eb_C12	-0.0003	0.0000	0.0002	0.04	0.0003	0.0000	-0.0002	-0.04
kNIWG2014a_Eb_016	0.0000	0.0000	0.0000	0.00	0.0000	0.0000	0.0000	0.00
kNXsec_CA5RES	-0.0130	-0.0157	-0.0361	-1.30	0.0144	0.0172	0.0394	1.29
kNXsec_MaNFFRES	-0.0220	-0.0244	-0.0481	-1.12	0.0281	0.0283	0.0498	0.34
KNXsec_BgSclRES	-0.0075	-0.0137	-0.0224	-0.43	0.0088	0.0159	0.0261	0.47
kNIWG2012a_ccnueE0	-0.0008	0.0000	0.0000	0.05	0.0008	0.0000	0.0000	-0.05
kNIWG2012a_dismpishp	-0.0503	-0.0715	-0.0702	3.20	0.0503	0.0715	0.0702	-3.18
kNIWG2012a_cccohE0	0.0000	0.0000	0.0000	0.00	0.0151	0.0000	0.0000	-0.92
kNIWG2012a_nccohE0	-0.0005	0.0000	0.0000	0.03	0.0005	0.0000	0.0000	-0.03
kNIWG2012a_ncotherE0	-0.0729	0.0000	0.0000	4.44	0.0729	0.0000	0.0000	-4.44

Table 6.2: POT-weighted averages of relative error of the number of selected background $\langle B_r^{MC} \rangle$, selected signal $\langle S_r^{MC} \rangle$, generated signal events $\langle n_r^{MC} \rangle$ and the calculated cross-section $\langle \sigma \rangle^{data,i}$ for each cross-section reweighting throw, where "mean diff" = "NIWG mean - T2KReWeight mean" and "error" = "NIWG error". The relative errors of $\langle B_r^{MC} \rangle, \langle S_r^{MC} \rangle$ and $\langle n_r^{MC} \rangle$ shown in this table are averages of the POT-weight values for all runs. However, to calculate $\langle \sigma \rangle^{data,i}$ values the $\langle B_r^{MC} \rangle, \langle S_r^{MC} \rangle$ and $\langle n_r^{MC} \rangle$ individual errors for each run were used.

6.2.2 FSI modelling

The FSI interactions are described in Section 1.3.3. FSI influence the multiplicity, types and momenta of hadrons produced in the neutrino primary interactions. The FSI systematic errors [99, 100, 103] arise from the uncertainty of the following parameters related to the pion scattering:

- Elastic scattering at low (FSIQE) and high energies (FSIQEH),
- Pion production (FSIINEL),
- Pion absorption (FSIABS),
- Charge exchange at low (FSICX) and high energies (FSICXH).

Values of these parameters for each of 16 reweighting throws are listed in Table 6.3. The throws take into account the biggest correlations between the parameters, e.g. the fact that the elastic scattering (FSIQEH) is strongly anticorrelated to the pion production (FSIINEL) and the charge exchange (FSICXH) at high energies. The correlations are discussed in [100, 103]. Table 6.4 presents the POT-weighted averages of relative error of the number of selected background, selected signal and generated signal events, as well as the cross-section $\langle\sigma\rangle^{data,i}$ induced by each reweighting throw. The relative errors are calculated as $(x^i - x^{nominal})/x^{nominal}$.

The FSI systematic error was calculated as RMS of the distribution $\langle\sigma\rangle^{data,i}$ with respect to the nominal value $\langle\sigma\rangle^{data}$:

$$\delta_{fsi}\langle\sigma\rangle^{data} = \sqrt{\frac{(\langle\sigma\rangle^{data,i} - \langle\sigma\rangle^{data})^2}{n\_throws}}, \tag{6.13}$$

where $n\_throws = 16$ is the number of the FSI reweighting throw. The calculated FSI systematic error equals:

$$\langle\sigma\rangle^{data} = (1.239 \pm 0.045(fsi)) \times 10^{-39}\ \mathrm{cm}^2/\mathrm{nucleon}, \tag{6.14}$$

$$\frac{\delta_{fsi}\langle\sigma\rangle^{data}}{\langle\sigma\rangle^{data}} = 3.6\%. \tag{6.15}$$

Throw	FSIQE	FSIQEH	FSIINEL	FSIABS	FSICX	FSICXH
Nominal	1.0	1.8	1.0	1.1	1.0	1.8
1	0.6	1.1	1.5	0.7	0.5	2.3
2	0.6	1.1	1.5	0.7	1.6	2.3
3	0.7	1.1	1.5	1.6	0.4	2.3
4	0.7	1.1	1.5	1.6	1.6	2.3
5	1.4	1.1	1.5	0.6	0.6	2.3
6	1.3	1.1	1.5	0.7	1.6	2.3
7	1.5	1.1	1.5	1.5	0.4	2.3
8	1.6	1.1	1.5	1.6	1.6	2.3
9	0.6	2.3	0.5	0.7	0.5	1.3
10	0.6	2.3	0.5	0.7	1.6	1.3
11	0.7	2.3	0.5	1.6	0.4	1.3
12	0.7	2.3	0.5	1.6	1.6	1.3
13	1.4	2.3	0.5	0.6	0.6	1.3
14	1.3	2.3	0.5	0.7	1.6	1.3
15	1.5	2.3	0.5	1.5	0.4	1.3
16	1.6	2.3	0.5	1.6	1.6	1.3

Table 6.3: FSI parameter sets – from Table 1 in [99].

Throw	Relative error (%)			
	$\langle B_r^{MC} \rangle$	$\langle S_r^{MC} \rangle$	$\langle n_r^{MC} \rangle$	$\langle \sigma \rangle^{data,i}$
1	1.04	4.13	2.06	-2.61
2	1.09	4.95	5.09	-0.53
3	0.40	0.45	-4.57	-5.23
4	0.31	0.99	-1.82	-2.97
5	-1.62	1.59	4.02	3.41
6	-1.28	1.99	7.52	6.24
7	-1.52	-1.88	-4.21	-1.47
8	-1.80	-1.89	0.15	3.21
9	1.82	1.87	0.20	-2.73
10	1.82	2.75	3.32	-0.56
11	1.24	-1.74	-6.36	-5.42
12	1.26	-1.23	-3.58	-3.14
13	-0.30	-0.66	2.23	3.10
14	-0.25	0.02	5.91	6.05
15	-0.52	-3.92	-5.95	-1.81
16	-0.54	-3.73	-1.40	2.75

Table 6.4: POT-weighted averages of relative error of the number of selected background $\langle B_r^{MC} \rangle$, selected signal $\langle S_r^{MC} \rangle$, generated signal events $\langle n_r^{MC} \rangle$ and the calculated cross-section $\langle \sigma \rangle^{data,i}$ for each FSI reweighting throw. The relative errors of $\langle B_r^{MC} \rangle, \langle S_r^{MC} \rangle$ and $\langle n_r^{MC} \rangle$ shown in this table are averages of the POT-weight values for all runs. However, to calculate $\langle \sigma \rangle^{data,i}$ values the $\langle B_r^{MC} \rangle, \langle S_r^{MC} \rangle$ and $\langle n_r^{MC} \rangle$ individual errors for each run were used.

6.3 Detector systematics

The detector systematics[2] is related to the simulation of the particle passage through matter and the detector response. This systematics affects the selection, so it can change the number of the selected signal and background events only (S_r^{MC} and B_r^{MC} in Equation (5.8) with r denoting the run number).

To evaluate a particular detector systematic error, it is needed to know the real distribution of a studied variable without relying on simulations. Therefore, an event sample of the known behaviour, which is called the control sample, is chosen. For example, the control sample used to evaluate the systematic error of charge misidentification is a pure sample of protons, chosen through a cut on $Pull_p$ (dE/dx). The energy of the neutrino beam is too low to produce antiprotons, therefore the control sample consists in the vast majority of positive particles. The real data-MC difference in the fraction of particles being misidentified as negative is a measure of this systematic error.

The value of the systematic uncertainty of a physical parameter (such as charge misidentification), evaluated based on the control sample, must be propagated to the change in the number of selected signal and background events. It can be done in the following three ways described in detail in Section 9 of [94]:

- Observable-variation systematics. The physics parameter is randomly altered (many times) within its systematic error. For each value of the parameter, the selection is repeated to get the number of selected events. This type of propagation is applied to the parameters that can take continuous values, such as momentum or $Pull$.

- Efficiency-like systematics. The selection is done once. After the selection, for each event the set of random weights within the parameter systematic error is calculated. This type of propagation is applied to the reconstructed object or particle parameters that can take two discrete values, such as charge or the fact that the object is reconstructed or not. If the event contains more than one object that needs to be taken into account, the individual weights must be combined together.

[2] `http://www.t2k.org/nd280/physics/systMasterTablePage` – list of the detector systematic errors – T2K Intranet.

- Normalization systematics. After the selection, the weight is assigned to the whole event. This type of propagation is applied to the parameters related to the whole event, such as FGD mass uncertainty or event pile-up, and not to an individual particle or reconstructed object.

Table 6.5 comprises the list of all detector systematic errors considered in this analysis and relative errors of the number of the selected signal $\langle \delta S_r^{MC}/S_r^{MC} \rangle$ and background $\langle \delta B_r^{MC}/B_r^{MC} \rangle$ events induced by them. The systematic errors related to the cuts used to select $\nu_\mu CC$ events are listed in the first part of this Table at positions 1-13 and are outlined in Section 6.3.1. The selection of $e^\pm$ inside the tracker uses the same variables as the μ^- selection: number of nodes, momentum, dE/dx, etc. The main difference in detector systematics calculations is that the muon candidates have to start in the FGD1 FV, while $e^\pm$ candidates start in FGD extended volume, i.e. inside whole FGD1 and FGD2 and TPC outer envelop (see Table 4.2 and Fig. 4.3). Therefore, after extending the group of reweighted TPC tracks from the tracks starting in FGD1 FV to the tracks starting in FGD extended volume, the $\nu_\mu CC$ systematics can be used to assess the large part of the systematics related to the $e^\pm$ selection.

The second part of Table 6.5 contains the systematic errors related to the selection cuts of the π^0 decay products not handled by the $\nu_\mu CC$ systematics. Two types of π^0 decay products are selected: $e^\pm$ tracks in the TPC from photons from π^0 decays (described in Sec. 4.4.2.1) and showers in the ECal produced by photons from π^0 decay (described in Sec. 4.4.2.2). Selection cuts of these two types of objects are independent. Thus, systematics related to them also does not depend on each other. The only $e^\pm$ systematic error not handled by the $\nu_\mu CC$ systematics is related to the FGD extended volume cut which is described in Section 6.3.2 (position 14 in Table 6.5). Section 6.3.3 characterises errors related the shower selection in the ECal, which are listed in Table 6.5 at positions 15-19. The errors related to the π^0 selection are described in more detail, as they have been mostly developed by the author of this thesis.

The influence of the detector systematics on the flux-averaged $(\nu_\mu CC\pi^0)_{incl.}$

No.	Systematic uncertainty	Relative error (%) $\langle B_r^{MC} \rangle$	Relative error (%) $\langle S_r^{MC} \rangle$	Detailed description
Errors related to the muon selection cuts				
1.	TPC field distortion	1.5473	1.4380	[94, 104]
2.	TPC cluster efficiency*	0.0048	0.0052	[94]
3.	TPC single and double track Reconstruction efficiency*	0.0613	0.0406	[94, 105]
4.	TPC momentum resolution*	0.0613	0.0405	[94, 106]
5.	TPC momentum scale*	0.0613	0.0405	[94, 97, 107, 108]
6.	TPC charge confusion	0.0784	0.0241	[94, 109]
7.	TPC PID*	0.0613	0.0406	[94, 110]
8.	FGD-TPC matching efficiency	0.0542	0.0559	[94, 111]
9.	FGD mass	0.5056	0.6075	[94, 112]
10.	OOFV events	4.3213	0.0010	[94, 113]
11.	Sand muon background	0.0466	0.0010	[94]
12.	Event pile-up	0.2811	0.2830	[94, 97]
13.	Pion secondary interactions	5.4695	4.6380	[94, 97, 114]
Errors related to the π^0 product selection				
$e^{\pm}$ TPC track selection				
14.	FGD extended volume cut	0.0797	0.0724	Sec. 6.3.2
γ ECal shower track selection				
15.	ECal reconstruction efficiency	2.4563	2.6748	[93, 115], Sec. 6.3.3.1
16.	ECal energy reconstruction	0.3131	0.2222	Sec. 6.3.3.2
17.	Tracker-ECal matching	0.0792	0.0605	[93, 95, 115], Sec. 6.3.3.3
18.	ECal PID	1.5453	1.4416	[93, 95, 96], Sec. 6.3.3.4
19.	Shower pile-up	0.5658	0.1047	Sec. 6.3.3.5
	Total error added in quadrature	7.7586	5.7741	

Table 6.5: Detector systematics uncertainties related to the $\nu_\mu CC$ selection cuts (upper part of the table) and to the π^0 selection (lower part of the table), which consists of $e^{\pm}$ track selection in the TPC and photon shower selection in the ECal. The selection of $e^{\pm}$ track in the TPC uses the same reconstructed variables as the muon (or $\nu_\mu CC$) selection. Thus, after small modifications of the uncertainties denoted with a star the $\nu_\mu CC$ systematics can be used to assess the large part of the $e^{\pm}$ related systematics. The systematic errors denoted with a star were originally applied only to the tracks starting in FGD1 FV. In the $(\nu_\mu CC\pi^0)_{incl.}$ analysis for the $e^{\pm}$ selection the tracks starting in the FGD extended volume are considered and this denotes the modification. The relative errors of $\langle B_r^{MC} \rangle$ and $\langle S_r^{MC} \rangle$ shown in this table are averages of the POT-weight values for all runs considered in this analysis. However, to calculate the detector systematic error for the $(\nu_\mu CC\pi^0)_{incl.}$ cross-section $\delta_{det}\langle\sigma\rangle^{data}$ the $\langle B_r^{MC} \rangle$ and $\langle S_r^{MC} \rangle$ individual errors for each run were used.

cross-section is calculated using the formula:

$$\delta\langle\sigma\rangle^{data} = \frac{1}{POT_{tot}^{data}\cdot T}\sqrt{\sum_{r=2,3c,4}\left(\frac{1}{\phi_{\nu_\mu,r}}\right)^2\cdot(\delta n_r^{data})^2},$$
$$\left(\delta n_r^{data}\right)^2 = \left(\frac{\partial n_r^{data}}{\partial B_r^{MC}}\cdot\delta B_r^{MC}\right)^2 + \left(\frac{\partial n_r^{data}}{\partial S_r^{MC}}\cdot\delta S_r^{MC}\right)^2. \quad (6.16)$$

where

$$\frac{\partial n_r^{data}}{\partial B_r^{MC}} = -\frac{norm_r}{S_r^{MC}/n_r^{MC}}, \quad (6.17)$$
$$\frac{\partial n_r^{data}}{\partial S_r^{MC}} = -\frac{N_r^{data} - B_r^{MC}\cdot norm_r}{(S_r^{MC})^2/n_r^{MC}}, \quad (6.18)$$

and δB_r^{MC} and δS_r^{MC} are the total background and signal detector systematic errors for run r. At this stage of the $(\nu_\mu CC\pi^0)_{incl.}$ analysis, individual systematic error contributions listed in Table 6.5 are added in quadrature without taking into account possible correlations. This should be improved in the future.

The resulting overall detector systematic error for the total flux-averaged $(\nu_\mu CC\pi^0)_{incl.}$ cross-section equals:

$$\langle\sigma\rangle^{data} = (1.239 \pm 0.133(det)) \times 10^{-39}\ \mathrm{cm}^2/\mathrm{nucleon}, \quad (6.19)$$
$$\frac{\delta_{det}\langle\sigma\rangle^{data}}{\langle\sigma\rangle^{data}} = 10.7\%. \quad (6.20)$$

As it can be seen in Table 6.5 the largest contributions come from: pion secondary interactions, ECal reconstruction efficiency, Out Of Fiducial Volume (OOFV) events, ECal PID and TPC field distortion. All the individual detector systematic errors are described more in detail in the following three subsections.

6.3.1 Systematics related to $\nu_\mu CC$ inclusive selection

In the $\nu_\mu CC$ selection, official cuts from the *numuCCAnalysis* package were applied. The *highland* package includes also the calculation of the systematic errors related to this selection. Their influence on the number of the selected signal and background events is presented in Table 6.5 as percentages of these two populations. The individual systematic errors (positions 1-13 in Table 6.5) are as follows:

1. TPC field distortion [94, 104]. This systematic uncertainty is related to the distortions of magnetic and electric fields in TPCs. The value and source of those distortions are not fully understood. Therefore, it is assumed that the systematic error equals to the difference in MC between the reconstruction for the perfect field and the field with empirical correction.

2. TPC cluster efficiency [22, 94]. The TPC cluster (also called node) is a collection of contiguous hits in the same column or row for horizontal and vertical tracks, respectively. The cluster efficiency systematics has an impact mainly on the TPC quality cut, which requires more than 18 clusters in the TPC segment closest to the track start position. The fraction of tracks not passing this cut is small, thus the associated systematic error is also small.

3. TPC single and double track reconstruction efficiency [22, 94, 105]. The control samples used to evaluate this efficiency were: single tracks of straight through-going muons, cosmic muons, single short tracks and two close tracks sample. The later required the use of the TPC pattern recognition algorithm, whose efficiency was estimated based only on MC truth information. For all control samples the efficiency in the real data and MC data sets is very high and is independent from the track momentum, angle or length. The conservative estimate of the systematic uncertainty is below 1.0% in each TPC.

4. TPC momentum resolution [22, 94, 106]. The momentum resolution systematic uncertainty is calculated from the difference between the measurements in TPC1 and TPC2, corrected by the energy loss in the intermediate FGD1. For global tracks the results of Kalman filter fit with different sets of subdetectors are compared.

5. TPC momentum scale [22, 94, 97, 107, 108]. The momentum scale uncertainty is related to a systematic shift of the reconstructed momentum distribution with respect to the true momentum distribution. The value of this shift was determined through comparison with the momentum measured from the range in FGD1 for a stopping cosmic muons sample [97] and through the calculation of the Δ^{++} reconstructed invariant mass distribution with different values of the shift [108].

6. TPC charge confusion [22, 94, 109]. This systematic uncertainty is evaluated from data-MC differences in the sample of tracks crossing more than one TPC, for whose the charge assigned by local reconstruction in each TPC and charge from global reconstruction is compared.

   The only π^0 cut that depends on the reconstructed charge is the requirement that positron candidates in TPC should have momentum below 800 MeV. As the charge reconstruction quality should have only a small influence on π^0 selection and because of problems with implementation of this systematic error in the $(\nu_\mu CC\pi^0)_{incl.}$ analysis, it is assumed that a percentage change in the number of events is the same as in the inclusive $\nu_\mu CC$ selection.

7. TPC PID systematic error [22, 94, 110] (*Pull* systematics, Eq. 4.1). The systematic error on $Pull_\mu$, $Pull_e$ and $Pull_p$ was evaluated through shifting and smearing those distributions in MC by the values determined from the three control samples: through-going muons, e^+e^- pairs from photon conversions and high energy positive particles dominated by protons.

8. FGD-TPC matching efficiency [94, 111]. There are two types of FGD-TPC matching efficiencies:

   - Basic FGD-TPC matching efficiency – probability that the TPC track is matched to any hit in FGD; if track is not matched, the events occurring inside FGD1 FV are reconstructed as located outside this volume,
   - Good FGD-TPC matching efficiency – probability that the TPC track is matched to all or almost all hits in FGD; in this case, the efficiency affects the Out-Of-Fiducial-Volume (OOFV) background contamination and is handled by OOFV systematics.

   If any hit in FGD exists, the basic TPC-FGD matching efficiency is found to be 100% both in the real data and MC. The only possibility that the matching is not working is when all hits in FGD are lost. This can happen only for very short segments in FGD. The systematic error is a consequence of a real data-MC difference in the efficiency of FGD hits reconstruction. It was decided by group analysing $\nu_\mu CC$ events to apply this systematics for tracks with less than 3 hits in FGD.

In the $(\nu_\mu CC\pi^0)_{incl.}$ analysis only the muon candidate, which has to be the Highest Momentum Negative track with part in the TPC (HMN track), is required to start inside FGD. The $e^{\pm}$ candidates are allowed to start in the TPC layers adhering to the FGD detectors, inside FGD extended volume defined in Table 4.2. Therefore, this sytematics is applied to the first three highest momentum negative tracks whose true starting position is located inside FGD1 FV.

9. FGD mass uncertainty. According to [22, 94, 112], an areal density of the FGD XY modules is overestimated by 0.41% in MC simulations. Additionally, the results of direct measurements of these modules can differ up to 0.38%. These two contributions added in quadrature give the systematic error of FGD1 FV mass equal to 0.6%.

10. Out Of Fiducial Volume (OOFV) Events [22, 94, 113]. The Out-Of-Fiducial-Volume background events are split into 9 categories, depending on the reason why the event was not rejected by the selection cuts. Next, cross-section rate uncertainty and the systematics related to the reconstruction are assigned to each category.

11. Sand muon background [22, 94]. This is the background from particles produced outside the ND280 detector and passing the FGD1 FV $\nu_\mu CC$ selection cuts. The systematic uncertainty on the amount of this background is calculated from the data-MC difference in the sand muons enriched control sample: sample of tracks entering through the upstream wall of the P0D detector. The difference was found to be approximately 10%.

12. Event pile-up [22, 94, 97]. Particles produced outside of the ND280 detector (sand muons, cosmics), as well as interactions inside the detector, especially in ECal and SMRD (the heaviest subdetectors), can overlap with reactions inside FGD1 FV. If they activate the TPC1 veto, the whole event is rejected, which decreases the efficiency. If such a track is assigned to the reaction in the FGD1 FV, it can be misclassified, e.g. as $\nu_\mu CC1\pi$ instead of $\nu_\mu CC0\pi$. The shower pile-up systematics is described in detail in Section 6.3.3.5.

13. Pion secondary interactions [94,97,114]. Geant4 [35,36] model of charged pion secondary interactions significantly differs from the external data.

Therefore, Geant4 cross-sections of such interactions were weighted to fit this data, and the uncertainty on the cross-sections measurement in these external data was used to calculate this detector systematic error, the largest one in this analysis.

6.3.2 π^0 related systematics – $e^{\pm}$ tracks in the TPC

This section describes the only systematic error related to the selection of $e^{\pm}$ from π^0 decays tracks in the TPC which is not handled by the $\nu_\mu CC$ systematics. It concerns the cut requiring the electron and positron track to start in the FGD extended volume. Its influence on the number of selected signal and background events is shown in Table 6.5 at position 14.

The FGD extended volume cut is not affected by the FGD-TPC matching efficiency systematics because the FGD extended volume definition allows the tracks to start in the TPCs near the edge of FGD, so even if the matching is not working correctly, the track will be accepted.

Expected number of selected signal events			
Cut	looser cut (increased allowed volume)	standard cut (standard volume)	tighter cut (decreased allowed volume)
Run 2	276	276	276
Run 3c	484	484	483
Run 4	1214	1213	1212

Expected number of selected background events			
Cut	looser cut (increased allowed volume)	standard cut (standard volume)	tighter cut (decreased allowed volume)
Run 2	201	201	201
Run 3c	350	350	350
Run 4	867	867	866

Table 6.6: Change in the number of the selected signal and background events after all $(\nu_\mu CC\pi^0)_{incl.}$ cuts in the MC sample normalized to the real data POT after increasing allowed volume (looser cut) and decreasing allowed volume (tighter cut) in the FGD extended volume cut by the X,Y and Z resolution with respect to the standard size of the allowed volume (standard cut).

The systematic error related to this cut was evaluated by shifting the size

of the allowed volume in the MC sample by the resolution in X, Y and Z coordinates, i.e. ± 15 mm, ± 15 mm and ± 10 mm, respectively. When the allowed volume was increased in each direction by the resolution value the cut became looser, and for the case with the allowed volume decreased in each direction the cut became tighter. Changes in the number of the selected signal and background events, caused by both shifts, are presented in Table 6.6. To evaluate the systematic error the values of bigger change in number of selected signal and background events were taken into account.

6.3.3 π^0 related systematics – photon showers in the ECal

This section describes the systematics related to the selection of photons from π^0 decays, showering in the ECal. Its influence on the number of selected signal and background events is shown in Table 6.5 at positions 15-19.

The systematics related to the ECal reconstruction was partly developed for the $\nu_e CC$ analysis [93,95] and further adjusted by the author of this thesis to the $(\nu_\mu CC\pi^0)_{incl.}$ analysis.

To avoid double counting it is important to use the control samples which do not overlap with the analysis sample. A standard control sample to investigate the shower reconstruction quality, used by the ECal group, is the sample of e^+e^- pairs from photon conversion or single electron-like tracks. Electrons (and positrons) are identified using dE/dx and have their momenta measured in the TPC. Two $e^\pm$ tracks constitute one of possible signatures of the neutral pion used in the presented analysis. Therefore, to avoid an overlap with the analysis sample, the control sample does not contain events with an identified muon-like track.

The systematic errors related to the ECal reconstruction are not taken into account for the events with at least two $e^\pm$ candidates in the TPC, because such events would be selected anyhow, as in this analysis two $e^\pm$'s are already the signature of π^0 . The events with at least 5 π^0 decay products candidates are also not reweighted, as the probability of losing at least 4 showers is negligible. For the efficiency-like systematics, the weight is calculated for each relevant true or reconstructed object and the event weight is the multiplication of these "object" weights. For the $(\nu_\mu CC\pi^0)_{incl.}$ selection it is not important if all such objects are correctly reconstructed, but only if at least two of them would pass cuts for π^0 decay product candidates. Therefore, artificially high value of a systematic error can be assigned to events with high multiplicity of objects

relevant for the reweighting. To avoid such situation, in the reweighted events, e.g. events with less than two $e^{\pm}$'s and less than 5 π^0 decay product candidates, the weight is assigned to not more than three objects relevant for particular systematic error. This procedure of selecting events and objects in these events for reweighting was applied to the systematic error related to the ECal shower reconstruction efficiency, track-shower discrimination (ECal PID) and Tracker-ECal matching efficiency systematics.

6.3.3.1 ECal reconstruction efficiency

Track pointing to	TECal	DsECal
Real data events	4306	4886
Expected events	4277	5250
Particle	Contribution (%)	
e^-	24.3	41.9
e^+	28.8	34.3
μ^-	25.5	12.8
π^+	12.8	6.1
π^-	5.0	2.8
p	2.0	0.9
μ^+	1.5	0.9
other	0.2	0.3

Table 6.7: Percentages of the true particle types for the control sample used to assess the ECal reconstruction efficiency systematic error of the showering particles.

The ECal reconstruction efficiency systematics [115] for this analysis is evaluated using the sample of electron-like tracks with the momentum between 100 MeV and 800 MeV pointing into TECal or DsECal. This is the control sample described in [93, 95] and used for the ECal reconstruction efficiency systematics, but for this analysis modified by rejecting events with muon-like track and restraining momenta of $e^{\pm}$-like tracks to $[100 - 800]$ MeV region. The contributions from different true particles in the control sample are listed in Table 6.7. The efficiency is calculated as the ratio of the events where the object in the ECal was reconstructed not farther than 70 cm from the point where the $e^{\pm}$ track leaves the TPC and enters ECal. The calculated

efficiency systematics is presented in Table 6.8. This error was propagated as efficiency-like systematics. The objects relevant for this systematic error were true electrons, positrons or photons, for which an isolated shower in the ECal with the electromagnetic energy larger than 50 MeV was reconstructed. The weight was assigned to at most three such objects, as it was described at the beginning of Section 6.3.3.

	MC eff. (%)	real data eff. (%)
TECal	43.27 ± 0.16	40.36 ± 0.75
DsECal	94.48 ± 0.07	94.94 ± 0.31

Table 6.8: ECal reconstruction efficiency of the showering particles.

6.3.3.2 ECal energy reconstruction

Expected number of selected signal events			
Cut	looser cut (energy $>$ 47.5 MeV)	standard cut (energy $>$ 50 MeV)	tighter cut (energy $>$ 52.5 MeV)
Run 2	277	276	275
Run 3c	485	484	483
Run 4	1215	1213	1210

Expected number of selected background events			
Cut	looser cut (energy $>$ 47.5 MeV)	standard cut (energy $>$ 50 MeV)	tighter cut (energy $>$ 52.5 MeV)
Run 2	201	201	200
Run 3c	351	350	349
Run 4	869	867	864

Table 6.9: Influence of shifting the shower electromagnetic energy cut on the number of the selected signal and background events after all $(\nu_\mu CC\pi^0)_{incl.}$ cuts in the MC sample normalized to the real data POT. The looser cut means standard cut -2.5 MeV while the tighter cut equals to standard cut +2.5MeV.

The electromagnetic energy reconstructed in the ECal for photon candidates is required to be larger than 50 MeV. To check the influence of the

energy measurement systematic error on the final sample, it was decided to vary the shower minimal energy cut by the resolution of the electromagnetic energy reconstruction equal to 2.5 MeV. The change in the number of the selected signal and background events is presented in Table 6.9.

6.3.3.3 Tracker-ECal matching

The tracker-ECal matching systematics [115] has two contribution:s TPC-ECal and FGD-ECal matching systematics.

The TPC-ECal matching efficiency systematic error [93, 95] is needed to assess the probability that the photon candidate in the ECal can result from a part of the broken track entering the calorimeter from the TPC. The control sample for this systematic error is a subset of the sample used for the ECal reconstruction efficiency systematics. It consists of the events with the electron-like track in TPC pointing to TECal or DsECal and with the shower in the ECal closer than 70 cm from the point where the electron-like track leaves TPC. The fraction of events where these two objects are matched together equals to the TPC-ECal matching efficiency in the real and simulated data. The measured efficiency uncertainty is presented in Table 6.10.

	EM energy	MC eff. (%)	real data eff. (%)
TECal	50-400.	72.92 ± 0.35	75.7 ± 1.6
	400-800.	72.33 ± 0.79	65.0 ± 4.7
	800-5000.	58.8 ± 1.2	58.2 ± 5.5
DsECal	50-400.	78.05 ± 0.20	76.40 ± 0.97
	400-800.	65.93 ± 0.35	64.0 ± 1.7
	800-5000.	43.12 ± 0.37	39.5 ± 1.8

Table 6.10: TPC track-ECal shower matching efficiency.

FGDs consist of a dense material in which electrons quickly lose energy and are likely to stop before reaching the calorimeter. Those subdetectors also have a poor particle identification ability. Therefore, it is hard to select the control sample of electrons passing through FGD and heading for the calorimeter, to estimate the FGD-ECal matching efficiency for showering particles. For that reason, the FGD-ECal matching efficiency systematic uncertainty is assumed to be equal to the TPC-ECal matching efficiency systematic uncertainty. It is

also propagated together with the TPC-ECal matching systematics under the analogical conditions.

This error was propagated as the efficiency-like systematics. The objects relevant for this systematic error were true charged particles crossing the tracker (TPC or FGD) and ECal, for which the track in the tracker and the shower in the ECal with the electromagnetic energy larger than 50 MeV were reconstructed. The weight was assigned to at most three such objects, as it was described at the beginning of Section 6.3.3. First, TPC-ECal tracks are taken into account. If there was less than three relevant TPC-ECal tracks, FGD-ECal tracks are reweighted.

6.3.3.4 ECal PID

Particle identification in the ECal relies on the Minimum Ionising Particle Electro-Magnetic shower (MIP EM) discriminator [93, 95, 96] and allows to discriminate shower-like objects from track-like objects, and thus $e^{\pm}/\gamma$ from μ. The systematic error of this variable was studied using a sample of cosmic muons in TECal, through-going muons in DsECal and a pure sample of electrons produced in γ conversions for TECal and DsECal separately. All these uncertainties appeared to be below 3.0%. This error was propagated as the efficiency-like systematics. The objects relevant for this systematic error were showers in TECal and DsECal. The weight was assigned to at most three such objects, as it was described at the beginning of Section 6.3.3.

6.3.3.5 Shower pile-up

The last cut of the $(\nu_\mu CC\pi^0)_{incl.}$ selection requires the existence of at least two π^0 decay products, i.e. $e^{\pm}$ tracks in the TPC and/or γ showers in the ECal. The showers, being photon candidates in the ECal, are reconstructed far from the neutrino vertex, in the outer heavy part of the ND280 detector where more neutrino interactions happen than in the tracker. Additionally, this selection does not take into account either the poorly known shower direction or the invariant mass of π^0 decay products. Therefore, γ candidates in the ECal are exposed to a pile-up with the products of other neutrino interactions, which in consequence can increase the number of events passing the selection cuts.

According to the simulations, after all cuts about 6%[3] of the selected show-

[3]In Table 4.8 the number of coincidental particles is higher, because these are showers

ers come from a different neutrino interaction than a muon candidate and 98.7% of these objects come from reactions outside FGD1 FV. To check if the expected number of such showers agrees with the real data, a control sample based on the following cuts was selected:

1. good beam and good ND280 data quality flags,
2. at least one shower in the ECal passing exactly the same requirements as the showers in the $(\nu_\mu CC\pi^0)_{incl.}$ sample,
3. no tracks either in TPC or in FGD.

Thanks to the selection of events with no object in the tracker, 99.8% of the showers come from reactions outside FGD1 FV and the control sample does not overlap with the selected analysis sample. For this control sample, 81.2% of showers come from the reactions in the outer detectors (70.6% – ECal, 10.6% – SMRD). Most of them are produced by muons incorrectly categorized as showers (40.5%) and protons (22.2%). Electrons, positrons and photons from the primary π^0 decay and from other sources constitute 22.5% in total. The detailed composition of the showers from a different neutrino vertex than the muon candidate in the analysis sample and showers from the control sample is presented in Table 6.11. The table contains information about the type of a particle producing the shower, the type of a reaction in which the particle was produced and the detector in which the neutrino reaction occurred. In other distributions and tables shown in this thesis all reactions with the vertex outside FGD1 FV are denoted as "Out of FGD1 FV". However, over 98% of the showers studied here come from the reaction with the vertex outside FGD1 FV. Therefore, in this subsection, while categorising with respect to the reaction type, it is not taken into account if the neutrino vertex was inside FGD1 FV or not. As it can be seen from the percentage contributions in Table 6.11, both samples are similar, which allows us to expect that the chosen control sample reflects also the real data-MC difference in the amount of the coincidental showers in the analysis sample.

In the control sample, the real data sample contains around 9% more events than predicted (Table 6.12). The excess in the real data is visible for showers with a low electromagnetic energy and a small number of hits (Fig. 6.4).

before the last cut on the minimum number of π^0 decay product candidates. In particular, this sample contains events with a muon candidate and exactly one π^0 decay product candidate in the ECal, which will not pass the last cut.

Particle	Analysis sample	Control sample
primary π^0	17.2%	13.2%
decay products		
other $e^{\pm}$ or γ	14.4%	9.3%
μ^-	30.5%	40.5%
$\pi^{\pm}$	13.6%	11.5%
p	21.6%	22.2%
other	2.7%	2.7%

Reaction	Analysis sample	Control sample
$(\nu_\mu CC\pi^0)_{incl.}$	25.3%	16.5%
$\nu_\mu NC$	25.3%	22.9%
$\nu_\mu CCQE$	22.6%	34.2%
$\nu_\mu CC$+others	12.4%	13.9%
$\nu_\mu CCsec\pi^0$	9.0%	5.3%
not ν_μ	7.3%	6.5%

Detector	Analysis sample	Control sample
BrECAL	61.8%	60.3%
dead material	9.3%	15.6%
SMRD	8.7%	10.6%
Tracker	8.0%	1.6%
DsECAL	5.4%	8.0%
P0D	3.5%	1.4%
P0DECAL	3.3%	2.3%

Table 6.11: Characteristics of the showers from a different neutrino vertex than the muon candidate in the analysis sample (second column) and showers from the control sample (third column): the type of a particle producing the shower (upper part), the type of a reaction in which the particle was produced (middle part) and the detector in which the neutrino reaction occurred (bottom part).

The excess in the number of coincidental showers passing the photon cuts in the ECal can increase the amount of selected background and signal events, if such showers overlap with the event after $\nu_\mu CC$ cuts with less than two π^0 decay product candidates. Events chosen because of the overlap with coincidental showers most likely will fall into the category with exactly two showers

Number of selected events					
Run	data	MC magnet	MC sand	total MC	data/MC
Run 2	219162	186221	13473	199695	1.09748
Run 3c	376429	316611	23234	339845	1.10765
Run 4	921558	796753	58098	854851	1.07803

Number of selected showers					
Run	data	MC magnet	MC sand	total MC	data/MC
Run 2	239243	203058	13770	216828	1.10338
Run 3c	412299	345952	23737	369689	1.11526
Run 4	1012190	870507	59372	929879	1.08852

Table 6.12: Number of selected events and selected showers in the shower pile-up control sample in the real data and MC magnet, MC sand and total minimum bias MC (magnet+sand) scaled to the real data POT, as well as the real data/total MC POT scaled ratio.

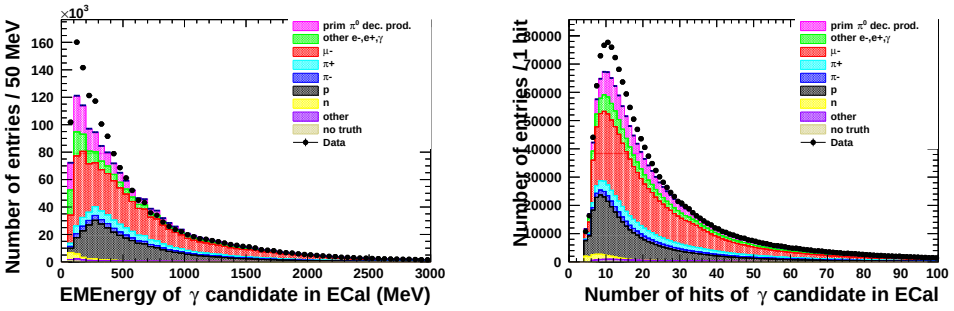

(a) (b)

Figure 6.4: Properties of the showers from the (pile-up) control sample. The plot (a) shows the reconstructed electromagnetic energy and the plot (b) – the number of hits. The Monte Carlo distributions are split according to the true particle type of the selected showers and scaled to the real data POT given in Table 3.1.

or the category with one shower and one $e^{\pm}$ candidate in the TPC. Events with more than two π^0 decay product candidates are less affected, because having at least two coincidental showers in one event is very unlikely. The expected relative systematic error in the number of selected background and

signal events in the analysis sample is calculated as:

$$\frac{\delta X_r^{MC}}{X_r^{MC}} = \delta N_{pile-up\ CS,r} \times \frac{X^{MC}_{pile-up\ shower,2sh,1sh+1e^{\pm},r}}{X^{MC}_{shower,2sh,1sh+1e^{\pm},r}} \times \frac{X^{MC}_{2sh,1sh+1e^{\pm},r}}{X_r^{MC}},$$
$$X = B, S, \tag{6.21}$$
$$\delta N_{pile-up\ CS,r} = \frac{N^{data}_{pile-up\ CS,r} - N^{MC}_{pile-up\ CS,r}}{N^{MC}_{pile-up\ CS,r}},$$

where

- X denotes selected background B or selected signal S events,
- $\delta X_r^{MC}/X_r^{MC}$ is the expected relative error in the simulated MC analysis sample (MC) in the number of selected background ($X = B$) or signal ($X = S$) events in run r,
- $N^{data/MC}_{pile-up\ CS,r}$ is the number of selected events in the pile-up control sample in the real data or in the MC sample scaled to the real data POT,
- $X^{MC}_{pile-up\ shower,2sh,1sh+1e^{\pm},r}$ is the number of coincidental showers in the selected X sample with exactly two showers in the ECal or one shower and one $e^{\pm}$ candidate in the TPC,
- $X^{MC}_{shower,2sh,1sh+1e^{\pm},r}$ is the number of all showers in the selected X sample with exactly two showers in the ECal or one shower and one $e^{\pm}$ candidate in the TPC,
- $X^{MC}_{2sh,1sh+1e^{\pm},r}$ is the number of X events in the selected sample with exactly two showers in the ECal or one shower and one $e^{\pm}$ candidate in the TPC,
- X_r^{MC} is the total number of X events in the sample after all $(\nu_\mu CC\pi^0)_{incl.}$ cuts.

The input values and the calculated error in the number of selected background and signal events are shown in Tables 6.12 and 6.13. The procedure described above is used to evaluate an increase in the number of selected background and signal events caused by additional coincidental showers. It must be noted that the excess of coincidental showers can also increase the average number of showers in the selected event sample and therefore it can rise the amount of events with more than two π^0 decay product candidates in the selected sample.

Run	Run 2	Run 3c	Run 4
$\delta N_{pile-up\ CS,r}$	9.75%	10.77%	7.80%
$\frac{B^{MC}_{pile-up\ shower,2sh,1sh+1e^{\pm},r}}{B^{MC}_{shower,2sh,1sh+1e^{\pm},r}}$	13.04%	14.84%	14.75%
$\frac{B^{MC}_{2sh,1sh+1e^{\pm},r}}{B^{MC}_{r}}$	44.50%	43.83%	44.51%
$\frac{\delta B^{MC}_{r}}{B^{MC}_{r}}$	0.5656%	0.7001%	0.5124%
$\frac{S^{MC}_{pile-up\ shower,2sh,1sh+1e^{\pm},r}}{S^{MC}_{shower,2sh,1sh+1e^{\pm},r}}$	3.04%	3.11%	3.63%
$\frac{s^{MC}_{2sh,1sh+1e^{\pm},r}}{S^{MC}_{r}}$	35.91%	34.89%	35.11%
$\frac{\delta S^{MC}_{r}}{S^{MC}_{r}}$	0.1063%	0.1168%	0.0995%

Table 6.13: Input values used in the calculations of the relative errors in the number of selected background and signal events resulting from the pile-up with coincidental showers produced in a different neutrino reaction than the muon candidate.

6.4 Systematics summary

The calculated cross-section systematic errors related to the neutrino flux uncertainty (flux), the modelling neutrino primary interactions (xsec) and FSI (fsi), as well as the detector response (det) equal:

$$\begin{aligned}\langle\sigma\rangle^{data} =&(1.239 \pm 0.034(stat)^{+0.175}_{-0.149}(flux) \pm^{+0.070}_{-0.072}(xsec) \\ &\pm 0.045(fsi) \pm 0.133(det)) \times 10^{-39}\ \text{cm}^2/\text{nucleon} \\ =&(1.239 \pm 0.034(stat)^{+0.235}_{-0.217}(syst)) \times 10^{-39}\ \text{cm}^2/\text{nucleon}.\end{aligned} \tag{6.22}$$

The biggest contributions come from the flux uncertainty and detector systematics. The other errors are significantly lower. The percentage error contributions with respect to $\langle\sigma\rangle^{data}$ are listed in Table 6.14.

Systematics source	Relative error
flux	$^{+14.1\%}_{-12.0\%}$
xsec	$^{+5.7\%}_{-5.8\%}$
fsi	$\pm 3.6\%$
det	$\pm 10.7\%$
Total	$^{+19.0\%}_{-17.5\%}$

Table 6.14: Summary of the total flux-averaged $(\nu_\mu CC\pi^0)_{incl.}$ cross-section systematic errors.

Summary

The analysis presented in this thesis was done on the 0.549×10^{21} POT set of the real data collected from November 2010 to May 2013 and divided into runs 2, 3c and 4. The results were compared with the predictions from the corresponding 12.21×10^{21} POT set of NEUT MC events. The sample of FGD1 FV $(\nu_\mu CC\pi^0)_{incl.}$ events was selected using the ND280 tracker and ECal with 58% purity and 32% efficiency. Based on this sample, the total flux-averaged cross-section was measured:

$$\begin{aligned}\langle\sigma\rangle^{data} =&(1.239 \pm 0.034(stat)^{+0.175}_{-0.149}(flux) \pm^{+0.070}_{-0.072}(xsec) \\ &\pm 0.045(fsi) \pm 0.133(det)) \times 10^{-39} \text{ cm}^2/\text{nucleon} \\ =&(1.239 \pm 0.034(stat)^{+0.235}_{-0.217}(syst)) \times 10^{-39} \text{ cm}^2/\text{nucleon},\end{aligned} \tag{6.23}$$

while the NEUT generator prediction is

$$\langle\sigma\rangle^{MC} = (1.0522 \pm 0.0028(stat)) \times 10^{-39} \text{ cm}^2/\text{nucleon}. \tag{6.24}$$

The statistical ($stat$) and systematic ($syst$) errors were assessed using the procedures approved by the T2K physics analyses groups. The measured cross-section is consistent within the errors with the expectations. The observed excess of the number of selected real data events is at the level of 10%, which results in the 18% excess in the measured cross-section.

The improvement of the ND280 software including better ECal reconstruction and systematic error treatment, will make it possible to further develop important parts of the $(\nu_\mu CC\pi^0)_{incl.}$ analysis, such as: selection of low energy photons in the ECal and $e^\pm$ tracks contained inside the FGD subdetectors to increase π^0 selection efficiency, taking into account correlations between systematic errors, more detailed studies of secondary π^0s and finally reconstruction of neutral pions momenta, directions and multiplicity. All these improvements should eventually lead to the calculation of the flux-averaged differential cross-section as a function of muon momentum and $\cos\theta$ and π^0 momentum, $\cos\theta$ and multiplicity.

Acknowledgements

This work was partially supported by the Polish National Science Centre, project number: UMO-2014/14/M/ST2/00850 and 2015/17/D/ST2/03533, as well as by the Marian Smoluchowski Krakow Consortium "Materia-Energia-Przyszłość" ("Matter-Energy-Future") from KNOW funds in the form of a PhD scholarship. This research was also supported by the PL-Grid Infrastructure.

First of all, I would like to express my sincere thanks to my supervisor prof. Agnieszka Zalewska for her expertise, valuable guidance and a great help with writing this thesis, as well as continuous support and patience.

My special thanks go to dr Tomasz Wąchała for valuable discussions and a great help with technical issues, especially systematic error calculations.

I would like to thank the T2K π^0 analysis group and its conveners, Helen O'Keeffe and Clark McGrew, for advice and support. I also thank Iain Lamont for his help with detector systematic errors.

I would like to express my gratitude to Beata Murzyn for linguistic correction.

My appreciation also goes to my colleagues from the Department of Neutrinos and Dark Matter Studies of the Institute of Nuclear Physics for their help and friendly atmosphere.

I thank my friends, especially Michał Kwaśniak and Magdalena Skurzok, who were always close to me, understanding and encouraging me all the time.

Last but not least, I would like to thank my family for supporting me throughout writing this thesis and my life in general.

Acronyms

BrECal Barrel Electromagnetic Calorimeter.

CC Charged Current.

CCQE Charged Current Quasi-Elastic.

COH Coherent pion production.

DIS Deep Inelastic Scattering.

DsECal Downstream Electromagnetic Calorimeter.

ECal Electromagnetic Calorimeter.

FG Fermi Gas.

FGD Fine Grained Detector.

FSI Final State Interactions.

FV Fiducial Volume.

GENIE Generates Events for Neutrino Interaction Experiments – the neutrino event generator.

GRV98 M. Glueck, E. Reya, A. Vogt package ; 1998 update – the parton distribution function.

HE photon Higher-Energy photon, i.e. photon from π^0 decay with a higher energy.

highland HIGH-Level Analysis in the ND280 detector.

HMN track Highest Momentum Negative track with part in the TPC.

IH Inverted Hierarchy.

INGRID Interactive Neutrino GRID.

J-PARC Japan Proton Accelerator Research Complex.

LE photon Lower-Energy photon, i.e. photon from π^0 decay with a lower energy.

MC Monte Carlo.

MEC Meson Exchange Current.

MIP EM Minimum Ionising Particle Electro-Magnetic shower.

NC Neutral Current.

NCE Neutral Current Elastic.

ND280 Near Detector at 280 m.

NEUT NEUT – the neutrino event generator.

NH Normal Hierarchy.

NIWG Neutrino Interaction Working Group.

NuWro Wrocław Neutrino Event Generator.

OOFV Out Of Fiducial Volume.

P0D Pi-Zero Detector.

PECal P0D ECal, part of BrECal around P0D.

PID Particle Identification.

POT Protons On Target.

RES Resonance production.

RFG Relativistic Fermi Gas.

RMS Root Mean Square.

SF Spectral Function.

SK Super-Kamiokande.

SM Standard Model.

SMRD Side Muon Range Detector.

T2K Tokai to Kamioka.

TECal Tracker ECal, part of BrECal around the tracker.

TPC Time Projection Chamber.

Bibliography

[1] J. A. Formaggio and G. P. Zeller. From eV to EeV: Neutrino Cross Sections Across Energy Scales. *Rev. Mod. Phys.*, 84:1307, 2012. http://arxiv.org/abs/1305.7513.

[2] K. A. Olive et al. Review of Particle Physics. *Chin. Phys.*, C38:090001, 2014. http://stacks.iop.org/1674-1137/38/i=9/a=090001.

[3] Wikimedia Commons. Standard model of elementary particles. https://commons.wikimedia.org/wiki/File:Standard_Model_of_Elementary_Particles.svg, 2014.

[4] C. L. Cowan, F. Reines, F. B. Harrison, H. W. Kruse, and A. D. McGuire. Detection of the free neutrino: A Confirmation. *Science*, 124:103–104, 1956. http://science.sciencemag.org/content/124/3212/103.

[5] B. Povh et al. *Particles and Nuclei.* Springer, 3 edition, 2002. http://link.springer.com/book/10.1007%2F978-3-662-05023-1.

[6] Artur M. Ankowski and Jan T. Sobczyk. Construction of spectral functions for medium-mass nuclei. *Phys. Rev.*, C77:044311, 2008. http://arxiv.org/abs/0711.2031.

[7] C. M. Jen, A. Ankowski, O. Benhar, A. P. Furmanski, L. N. Kalousis, and C. Mariani. Numerical Implementation of lepton-nucleus interactions and its effect on neutrino oscillation analysis. *Phys. Rev.*, D90(9):093004, 2014. http://arxiv.org/abs/1402.6651.

[8] Daniel Ivan Scully. *Neutrino Induced Coherent Pion Production.* PhD thesis, University of Warwick, Department of Physics, September 2013. http://www.t2k.org/docs/thesis/038.

[9] C. H. Llewellyn Smith. Neutrino Reactions at Accelerator Energies. *Phys. Rept.*, 3:261–379, 1972. https://inspirehep.net/record/67183.

[10] Carl H. Albright, C. Quigg, R. E. Shrock, and J. Smith. Neutrino - Proton Elastic Scattering: Implications for Weak Interaction Models. *Phys. Rev.*, D14:1780, 1976. http://dx.doi.org/10.1103/PhysRevD.14.1780.

[11] Dieter Rein and Lalit M. Sehgal. Neutrino Excitation of Baryon Resonances and Single Pion Production. *Annals Phys.*, 133:79–153, 1981. http://www.pas.rochester.edu/~ksmcf/rein-sehgal/rein-sehgal.pdf.

[12] A. A. Aguilar-Arevalo et al. First Measurement of the Muon Neutrino Charged Current Quasielastic Double Differential Cross Section. *Phys. Rev.*, D81:092005, 2010. http://arxiv.org/abs/1002.2680.

[13] V Lyubushkin et al. A Study of quasi-elastic muon neutrino and antineutrino scattering in the NOMAD experiment. *Eur. Phys. J.*, C63:355–381, 2009. http://arxiv.org/abs/0812.4543.

[14] A. Liesenfeld et al. A Measurement of the axial form-factor of the nucleon by the p(e, e' pi+)n reaction at W = 1125-MeV. *Phys. Lett.*, B468:20, 1999. http://arxiv.org/abs/nucl-ex/9911003.

[15] M. B. Barbaro, J. E. Amaro, J. A. Caballero, T. W. Donnelly, J. M. Udias, and C. F. Williamson. Meson-exchange Currents and Quasielastic Neutrino Cross Sections. 2011. http://arxiv.org/abs/1110.4739.

[16] The T2K experiment. http://t2k-experiment.org.

[17] K. Abe et al. The T2K Experiment. *Nucl. Instrum. Meth.*, A659:106–135, 2011. http://arxiv.org/abs/1106.1238.

[18] Yury Kudenko. The Near neutrino detector for the T2K experiment. *Nucl.Instrum.Meth.*, A598:289–295, 2009. http://arxiv.org/abs/0805.0411.

[19] D. Karlen. Near detectors for the T2K experiment. *Nucl. Phys. Proc. Suppl.*, 159:91–96, 2006. http://dx.doi.org/10.1016/j.nuclphysbps.2006.08.062.

[20] T2K ND280 Conceptual Design Report. http://www.nd280.org/documents/cdr.pdf.

[21] Y. Fukuda et al. The Super-Kamiokande detector. *Nucl. Instrum. Meth.*, A501:418–462, 2003. http://dx.doi.org/10.1016/S0168-9002(03)00425-X.

[22] Melody Ravonel Salzgeber. *Measurement of the Inclusive ν_μ Charged Current Cross Section in the Near Detector of the T2K Experiment.* PhD thesis, University of Geneva, 2012. http://www.t2k.org/docs/thesis/024.

[23] K. Abe et al. T2K neutrino flux prediction. *Phys.Rev.*, D87(1):012001, 2013. http://arxiv.org/abs/1211.0469.

[24] M.Fried et al. T2K-TN-217. Version 3. Flux Prediction and Uncertainty Updates with NA61 2009 Thin Target Data and Negative Focussing Mode Predictions. April 2015. http://www.t2k.org/docs/technotes/217/statistical-update-for-the-run-6-flux-tuning-version-3 – T2K Intranet.

[25] S. Assylbekov et al. The T2K ND280 Off-Axis Pi-Zero Detector. *Nucl. Instrum. Meth.*, A686:48–63, 2012. http://dx.doi.org/10.1016/j.nima.2012.05.028.

[26] N. Abgrall et al. Time Projection Chambers for the T2K Near Detectors. *Nucl. Instrum. Meth.*, A637:25–46, 2011. http://arxiv.org/abs/1012.0865.

[27] P. A. Amaudruz et al. The T2K Fine-Grained Detectors. *Nucl. Instrum. Meth.*, A696:1–31, 2012. http://arxiv.org/abs/1204.3666.

[28] D. Allan et al. The Electromagnetic Calorimeter for the T2K Near Detector ND280. *JINST*, 8:P10019, 2013. http://dx.doi.org/10.1088/1748-0221/8/10/P10019.

[29] S. Aoki et al. The T2K Side Muon Range Detector (SMRD). *Nucl. Instrum. Meth.*, A698:135–146, 2013. http://arxiv.org/pdf/1206.3553.pdf.

[30] K. Abe et al. Measurements of neutrino oscillation in appearance and disappearance channels by the T2K experiment with 6.6×10^{20} protons on target. *Phys. Rev.*, D91(7):072010, 2015. http://arxiv.org/abs/1502.01550.

[31] A.Hillairet, A.Izmaylov, et al. T2K-TN-072-v1.0. ND280 Reconstruction. November 2011. http://www.t2k.org/docs/technotes/072/tn72_reconstruction_technote_v1.0 – T2K Intranet.

[32] Super-Kamiokand Official Homepage. http://www-sk.icrr.u-tokyo.ac.jp/sk/index-e.html.

[33] K. Abe et al. Precise Measurement of the Neutrino Mixing Parameter θ_{23} from Muon Neutrino Disappearance in an Off-Axis Beam. *Phys. Rev. Lett.*, 112(18):181801, 2014. http://arxiv.org/abs/1403.1532.

[34] K. Abe et al. Measurement of the inclusive ν_μ charged current cross section on carbon in the near detector of the T2K experiment. *Phys.Rev.*, D87(9):092003, 2013. http://arxiv.org/abs/1302.4908.

[35] S. Agostinelli et al. GEANT4: A Simulation toolkit. *Nucl. Instrum. Meth.*, A506:250–303, 2003. http://dx.doi.org/10.1016/S0168-9002(03)01368-8.

[36] John Allison et al. Geant4 developments and applications. *IEEE Trans. Nucl. Sci.*, 53:270, 2006. http://dx.doi.org/10.1109/TNS.2006.869826.

[37] Y. Hayato. A neutrino interaction simulation program library NEUT. *Acta Physica Polonica B*, 40:2477–2489, 2009. www.actaphys.uj.edu.pl/fulltext?series=Reg&vol=40&page=2477.

[38] Y. Hayato. NEUT. *Nucl.Phys.Proc.Suppl.*, 112:171–176, 2002. http://dx.doi.org/10.1016/S0920-5632(02)01759-0.

[39] S. H. Ahn et al. Detection of accelerator produced neutrinos at a distance of 250-km. *Phys. Lett.*, B511:178–184, 2001. http://arxiv.org/abs/hep-ex/0103001.

[40] R. A. Smith and E. J. Moniz. Neutrino Reactions On Nuclear Targets. *Nucl. Phys.*, B43:605, 1972. http://dx.doi.org/10.1016/0550-3213(72)90040-5,http://dx.doi.org/10.1016/0550-3213(75)90612-4.

[41] Dieter Rein and Lalit M. Sehgal. Coherent pi0 Production in Neutrino Reactions. *Nucl. Phys.*, B223:29–44, 1983. http://dx.doi.org/10.1016/0550-3213(83)90090-1.

[42] P. Marage et al. Coherent Single Pion Production by Anti-neutrino Charged Current Interactions and Test of PCAC. *Z. Phys.*, C31:191–197, 1986. http://dx.doi.org/10.1007/BF01479526.

[43] D. Rein and L. M. Sehgal. PCAC and the Deficit of Forward Muons in pi+ Production by Neutrinos. *Phys. Lett.*, B657:207–209, 2007. http://arxiv.org/abs/hep-ph/0606185.

[44] M. Glück, E. Reya, and A. Vogt. Dynamical parton distributions revisited. *Eur. Phys. J.*, C5:461–470, 1998. http://arxiv.org/abs/hep-ph/9806404.

[45] A. Bodek and U. K. Yang. Modeling neutrino and electron scattering inelastic cross- sections in the few GeV region with effective LO PDFs TV Leading Order. In *2nd International Workshop on Neutrino-Nucleus Interactions in the Few GeV Region (NuInt 02) Irvine, California, December 12-15, 2002*, 2003. http://arxiv.org/abs/hep-ex/0308007.

[46] L. L. Salcedo, E. Oset, M. J. Vicente-Vacas, and C. Garcia-Recio. Computer Simulation of Inclusive Pion Nuclear Reactions. *Nucl. Phys.*, A484:557, 1988. http://dx.doi.org/10.1016/0375-9474(88)90310-7.

[47] Glenn Rowe, Martin Salomon, and Rubin H. Landau. An Energy Dependent Phase Shift Analysis of Pion - Nucleon Scattering Below 400-MeV. *Phys. Rev.*, C18:584–589, 1978. http://link.aps.org/doi/10.1103/PhysRevC.18.584.

[48] R. Seki and K. Masutani. Unified analysis of pionic atoms and low-energy pion-nucleus scattering: Phenomenological analysis. *Phys. Rev.*, C27:2799–2816, 1983. http://link.aps.org/doi/10.1103/PhysRevC.27.2799.

[49] B. R. Martin and M. K. Pidcock. Anti-K n Interactions in the Resonance Region. 1. Analysis of Data. *Nucl. Phys.*, B126:266–284, 1977. http://www.sciencedirect.com/science/article/pii/0550321377903820.

[50] B. R. Martin and M. K. Pidcock. Anti-K n Interactions in the Resonance Region. 2. Amplitudes. *Nucl. Phys.*, B126:285–297, 1977. http://www.sciencedirect.com/science/article/pii/0550321377903832.

[51] J. S. Hyslop, R. A. Arndt, L. D. Roper, and R. L. Workman. Partial wave analysis of K+ nucleon scattering. *Phys. Rev.*, D46:961–969, 1992. http://link.aps.org/doi/10.1103/PhysRevD.46.961.

[52] D.A. Sparrow. Effects of the nuclear medium on the observation of baryon number violation. pages 1019–1025, November 1984. http://dx.doi.org/10.1063/1.34840.

[53] H. W. Bertini. Nonelastic interactions of nucleons and pi mesons with complex nuclei at energies below 3 gev. *Phys. Rev.*, C6:631–659, 1972. http://link.aps.org/doi/10.1103/PhysRevC.6.631.

[54] S. J. Lindenbaum and R. M. Sternheimer. Isobaric nucleon model for pion production in nucleon-nucleon collisions. *Phys. Rev.*, 105:1874–1879, 1957. http://link.aps.org/doi/10.1103/PhysRev.105.1874.

[55] GENIE Neutrino Monte Carlo Generator. http://www.genie-mc.org/.

[56] C. Andreopoulos et al. The GENIE Neutrino Monte Carlo Generator. *Nucl. Instrum. Meth.*, A614:87–104, 2010. http://arxiv.org/abs/0905.2517.

[57] A. Bodek and J. L. Ritchie. Further Studies of Fermi Motion Effects in Lepton Scattering from Nuclear Targets. *Phys. Rev.*, D24:1400, 1981. http://link.aps.org/doi/10.1103/PhysRevD.24.1400.

[58] L. A. Ahrens et al. Measurement of Neutrino - Proton and anti-neutrino - Proton Elastic Scattering. *Phys. Rev.*, D35:785, 1987. http://link.aps.org/doi/10.1103/PhysRevD.35.785.

[59] R. P. Feynman, M. Kislinger, and F. Ravndal. Current matrix elements from a relativistic quark model. *Phys. Rev.*, D3:2706–2732, 1971. http://link.aps.org/doi/10.1103/PhysRevD.3.2706.

[60] A Bodek and U. K. Yang. Higher twist, ξ_ω scaling, and effective LO PDFs for lepton scattering in the few GeV region. *J. Phys.*, G29:1899–1906, 2003. http://arxiv.org/abs/hep-ex/0210024.

[61] T. Yang, C. Andreopoulos, H. Gallagher, and P. Kehayias. A hadronization model for the MINOS experiment. *AIP Conf. Proc.*, 967:269–275, 2007. http://dx.doi.org/10.1063/1.2834490.

[62] S. G. Kovalenko. Quasielastic neutrino production of charmed baryons from the point of view of local duality. *Sov. J. Nucl. Phys.*, 52:934–936, 1990. https://inspirehep.net/record/299416.

[63] Markus Bischofberger. *Quasi elastic charm production in neutrino nucleon scattering.* PhD thesis, Zurich, ETH, 2005. http://e-collection.ethbib.ethz.ch/show?type=diss&nr=16034.

[64] M. A. G. Aivazis, Frederick I. Olness, and Wu-Ki Tung. Leptoproduction of heavy quarks. 1. General formalism and kinematics of charged current and neutral current production processes. *Phys. Rev.*, D50:3085–3101, 1994. http://arxiv.org/abs/hep-ph/9312318.

[65] G. De Lellis, F. Di Capua, and P. Migliozzi. Prediction of charm production fractions in neutrino interactions. *Phys. Lett.*, B550:16–23, 2002. http://arxiv.org/abs/hep-ph/0210383.

[66] C. Peterson, D. Schlatter, I. Schmitt, and Peter M. Zerwas. Scaling Violations in Inclusive e+ e- Annihilation Spectra. *Phys. Rev.*, D27:105, 1983. http://link.aps.org/doi/10.1103/PhysRevD.27.105.

[67] P. D. B. Collins and T. P. Spiller. The Fragmentation of Heavy Quarks. *J. Phys.*, G11:1289, 1985. http://stacks.iop.org/0305-4616/11/i=12/a=006.

[68] D. Yu. Bardin and V. A. Dokuchaeva. Muon Energy Spectrum in Inverse μ Decay. *Nucl. Phys.*, B287:839, 1987. http://dx.doi.org/10.1016/0550-3213(87)90131-3.

[69] William J. Marciano and Zohreh Parsa. Neutrino electron scattering theory. *J. Phys.*, G29:2629–2645, 2003. http://arxiv.org/abs/hep-ph/0403168.

[70] Steven Dytman. Final state interactions in neutrino-nucleus experiments. *Acta Phys. Polon.*, B40:2445–2460, 2009. www.actaphys.uj.edu.pl/fulltext?series=Reg&vol=40&page=2445.

[71] Wrocław Neutrino Group. NuWro – Wrocław Neutrino Events Generator. http://borg.ift.uni.wroc.pl/nuwro/.

[72] Tomasz Golan, Cezary Juszczak, and Jan T. Sobczyk. Final State Interactions Effects in Neutrino-Nucleus Interactions. *Phys. Rev.*, C86:015505, 2012. http://arxiv.org/abs/1202.4197.

[73] Wrocław University – Neutrino Physics Division. http://neutrino.ift.uni.wroc.pl.

[74] O. Benhar, A. Fabrocini, S. Fantoni, and I. Sick. Spectral function of finite nuclei and scattering of GeV electrons. *Nucl. Phys.*, A579:493–517, 1994. http://dx.doi.org/10.1016/0375-9474(94)90920-2.

[75] D. Rohe et al. Correlated strength in nuclear spectral function. *Phys. Rev. Lett.*, 93:182501, 2004. http://arxiv.org/abs/nucl-ex/0405028.

[76] Daniela Rohe. First measurement of the spectral function at high energy and momentum in medium-heavy nuclei. *Nucl. Phys. Proc. Suppl.*, 159:152–157, 2006. [,152(2006)].

[77] C. Juszczak, J. A. Nowak, and J. T. Sobczyk. Spectrum of recoil nucleons in quasi-elastic neutrino nucleus interactions. *Eur. Phys. J.*, C39:195–200, 2005. http://borg.ift.uni.wroc.pl/nuwro/?s=4.

[78] M. Martini, M. Ericson, G. Chanfray, and J. Marteau. A Unified approach for nucleon knock-out, coherent and incoherent pion production in neutrino interactions with nuclei. *Phys. Rev.*, C80:065501, 2009. http://arxiv.org/abs/0910.2622.

[79] A. Bodek, H. S. Budd, and M. E. Christy. Neutrino Quasielastic Scattering on Nuclear Targets: Parametrizing Transverse Enhancement (Meson Exchange Currents). *Eur. Phys. J.*, C71:1726, 2011. http://arxiv.org/abs/1106.0340.

[80] J. Nieves, I. Ruiz Simo, and M. J. Vicente Vacas. Inclusive Charged–Current Neutrino–Nucleus Reactions. *Phys. Rev.*, C83:045501, 2011. http://arxiv.org/abs/1102.2777.

[81] K. M. Graczyk, D. Kielczewska, P. Przewlocki, and J. T. Sobczyk. C_5^A axial form factor from bubble chamber experiments. *Phys. Rev.*, D80:093001, 2009. http://arxiv.org/abs/0908.2175.

[82] G. M. Radecky et al. Study of Single Pion Production by Weak Charged Currents in Low-energy Neutrino d Interactions. *Phys. Rev.*, D25:1161–1173, 1982. http://link.aps.org/doi/10.1103/PhysRevD.25.1161.

[83] T. Kitagaki et al. Charged Current Exclusive Pion Production in Neutrino Deuterium Interactions. *Phys. Rev.*, D34:2554–2565, 1986. http://link.aps.org/doi/10.1103/PhysRevD.34.2554.

[84] E. Oset and L. L. Salcedo. Δ Selfenergy in Nuclear Matter. *Nucl. Phys.*, A468:631–652, 1987. http://dx.doi.org/10.1016/0375-9474(87)90185-0.

[85] Ch. Berger and L. M. Sehgal. PCAC and coherent pion production by low energy neutrinos. *Phys. Rev.*, D79:053003, 2009. http://arxiv.org/abs/0812.2653.

[86] A. Bodek and U. K. Yang. Modeling deep inelastic cross-sections in the few GeV region. *Nucl. Phys. Proc. Suppl.*, 112:70–76, 2002. [,70(2002)].

[87] Jarosław Andrzej Nowak. *Construction of neutrino event generator (in polish)*. PhD thesis, University of Wroclaw, 2006. neutrino.ift.uni.wroc.pl/files/Nowak_PhD.ps.

[88] N. Metropolis, R. Bivins, M. Storm, J. M. Miller, G. Friedlander, and Anthony Turkevich. Monte Carlo Calculations on Intranuclear Cascades. 2. High-Energy Studies and Pion Processes. *Phys. Rev.*, 110:204–219, 1958. http://link.aps.org/doi/10.1103/PhysRev.110.204.

[89] V. R. Pandharipande and Steven C. Pieper. Nuclear transparency to intermediate-energy nucleons from (e, e'p) reactions. *Phys. Rev.*, C45:791–798, 1992. http://link.aps.org/doi/10.1103/PhysRevC.45.791.

[90] Tomasz Golan. *Modeling nuclear effects in NuWro Monte Carlo neutrino event generator*. PhD thesis, University of Wroclaw, 2014. neutrino.ift.uni.wroc.pl/files/phd_tomasz_golan.pdf.

[91] M.Bass et al. T2K-TN-013. Version 1. Quality assessment of the 2010a data set at ND280. December 2010. www.t2k.org/docs/technotes/013/T2K-TN-013_v01 – T2K Intranet.

[92] C. Giganti, M. Zito. T2K-TN-001. Version 2. Particle Identification with the T2K TPC. October 2009. http://www.t2k.org/docs/technotes/001/dEdxnote_v2 – T2K Intranet.

[93] T2K Collaboration. Measurement of the intrinsic electron neutrino component in the t2k neutrino beam with the nd280 detector. *Phys. Rev. D*, 89:092003, May 2014. http://link.aps.org/doi/10.1103/PhysRevD.89.092003.

[94] P.Bartet et al. T2K-TN-212. Version 2.1.1. ν_μ CC event selection in the ND280 tracker using Run 2+3+4 data. October 2015. www.t2k.org/docs/technotes/212/tn-212-v-2-1.1 – T2K Intranet.

[95] J. Caravaca, G. Christodoulou, et al. T2K-TN-149. Version 3.1. Measurement of the electron neutrino beam component in the ND280 Tracker for 2013 analyses. January 2014. http://www.t2k.org/docs/technotes/149/NuETN_v3.1.pdf – T2K Intranet.

[96] G. Barker, S. Boyd, et al. T2K-TN-111. Release 1.0. Implementation of the Second Generation PID for the ND280 Tracker ECals. August 2012. http://www.t2k.org/docs/technotes/111/ecalPidTechNote_v1r0 – T2K Intranet.

[97] C. Bojechko, J. Caravaca, et al. T2K-TN-152-V4.2. CC-multiple-pion ν_μ event selections in the ND280 tracker using Run 1+2+3+4 data. November 2013. http://www.t2k.org/docs/technotes/152/t2ktn152v4.2 – T2K Intranet.

[98] Cholesky factorization. N.J. Higham (originator). Encyclopedia of Mathematics. https://www.encyclopediaofmath.org/index.php/Cholesky_factorization.

[99] P. de Perio et al. T2K-TN-108. Version 1.5. Cross section parameters for the 2012a oscillation analysis. January 2013. www.t2k.org/docs/technotes/108/T2K-TN-108-v1.5_Cross_section_parameters_for_the_2012a_oscillation_analysis.pdf – T2K Intranet.

[100] A.Bercellie et al. T2K-TN-192. Version 2.2. Cross section parameters for 2014 oscillation analysis. June 2015. www.t2k.org/docs/technotes/192/version22 – T2K Intranet.

[101] A.Bercellie et al. T2K-TN-193. Version 1.1. Implementation of additional NIWG cross section parametrizations for 2014 analyses. January 2015. www.t2k.org/docs/technotes/193/v11 – T2K Intranet.

[102] T.Campbell et al. T2K-TN-208. Version 2. The $\bar{\nu}_\mu/\nu_\mu$ Cross Section Ratio with the P0D-TPC1 Samples. October 2015. www.t2k.org/docs/technotes/208/the-n-m-nm-cross-sections-ratio-with-the-pod-tpc1-samples-1 – T2K Intranet.

[103] Patrick de Perio. Status of NEUT FSI π Scattering Fits. www.t2k.org/asg/xsec/meetings/niwgmeetings-2011/niwg20110926/110926-NIWG_FSI_Fits.pdf – T2K Intranet, September 2011.

[104] C. Bojechko, A. Cervera, et al. T2K-TN-061. Measurement and Correction of Magnetic Field Distortions in the Time Projection Chambers. 2013. http://www.t2k.org/docs/technotes/061/v2 – T2K Intranet.

[105] Yevgeniy Petrov, Anthony Hillairet. T2K-TN-163. ND280 TPC Track Reconstruction Efficiency. Version 2.0. January 2015. http://www.t2k.org/docs/technotes/163/TN163_version2rev_for_Prod6B – T2K Intranet.

[106] A.Cervera, L.Escudero. T2K-TN-222. Study of momentum resolution and scale using tracks that cross multiple TPCs. November 2014. www.t2k.org/docs/technotes/222/ – T2K Intranet.

[107] E.Frank et al. T2K-TN-081. B-field calibration and systematic errors. November 2011. www.t2k.org/docs/technotes/081/ – T2K Intranet.

[108] Eike Frank. *Precision Measurement of the ND280 Magnetic Field in the T2K Neutrino Experiment: Confirmation of the Momentum Scale through $\Delta++$ Resonances.* PhD thesis, University of Bern, 2012. http://www.t2k.org/docs/thesis/021.

[109] F.Sanchez, J.Medina. T2K-TN-229. Version 2. ND280 Global Charge Identification Systematic Error. January 2015. http://www.t2k.org/docs/technotes/229/V2 – T2K Intranet.

[110] S.Bordoni et al. T2K-TN-221. The TPC Particle IDentification algorithm with production 6B. April 2015. www.t2k.org/docs/technotes/221/TN221v1 – T2K Intranet.

[111] A. Hillairet, L. Haegel, et al. T2K-TN-75. ND280 tracker tracking efficiency. January 2015. http://www.t2k.org/docs/technotes/075/tm075v1.2 – T2K Intranet.

[112] T. Lindner K. Mahn, S. Oser. T2K-TN-122. Version 4. FGD Mass Checks. May 2012. www.t2k.org/docs/technotes/122 – T2K Intranet.

[113] F.Dufour et al. T2K-TN-098. Version 1.1. Systematics on Out-of-Fiducial-Volume Backgrounds in the ND280 Tracker. June 2015. www.t2k.org/docs/technotes/098/tn98oofvv2 – T2K Intranet.

[114] J. Myslic. T2K-TN-125. Determination of pion secondary interaction systematics for the ND280 tracker ν_μ analysis. October 2013. http://www.t2k.org/docs/technotes/125/tn-125-pionsec-v02.pdf – T2K Intranet.

[115] Iain Lamont – private communication.